The Kinetic Plasma Physics of Solar-Wind Electrons

Seong-Yeop Jeong

A dissertation submitted in partial fulfillment

of the requirements for the degree of

Doctor of Philosophy

of

University College London.

Department of Space & Climate Physics

University College London

April 12, 2022

I, Seong-Yeop Jeong, confirm that the work presented in this thesis is my own. Where information has been derived from other sources, I confirm that this has been indicated in the work.

Abstract

This thesis uses kinetic plasma physics to study the kinetic evolution of the electron velocity distribution function (VDF) in the solar wind. We propose an analytical model for resonant wave–particle instability in homogeneous plasma based on quasi-linear theory. By using this model, we confirm that the oblique fast-magnetosonic/whistler (FM/W) instability can scatter the electron strahl in the electron VDF.

Following the study of the local scattering, we propose a global transport theory for the kinetic expansion of solar-wind electrons. We derive a gyro-averaged kinetic transport equation that accounts for the solar-wind expansion in the geometry of the Parker-spiral magnetic field. Our kinetic transport model shows the development of the core–strahl configuration in the electron VDF near the Sun. Applying fits to our numerical results, we compare our numerical results with data from Parker Solar Probe (PSP), and provide theoretical evidence that the electron strahl is not scattered by the oblique FM/W instability near the Sun.

To confirm our theoretical results for strahl scattering, we analyse data from PSP and Helios. We compare the measured strahl properties with the analytical thresholds for the oblique FM/W instability in the low- and high-$\beta_{\|c}$ regimes, where $\beta_{\|c}$ is the ratio of the parallel core thermal pressure to the magnetic pressure, as functions of heliocentric distance. Our PSP and Helios data show that the electron strahl is stable against the oblique FM/W instability in the inner heliosphere. Our analysis suggests that this instability can only be excited sporadically, on short timescales.

For the numerical evaluation of the kinetic equations in the research chapters,

we develop a mathematical approach based on the Crank–Nicolson scheme. This approach numerically solves any kind of diffusion equations with any dimensions. We note that our mathematical approach is applicable to other complex diffusion equations.

Impact Statement

Most of the visible matter in the universe is in the plasma state. In many space and astrophysical plasmas, such as stellar winds, supernovae, black hole accretion discs, and the interstellar medium, there are many open questions on fundamental plasma physics relating to the transfer of energy. Wave–particle interactions play an important role for the energy exchange between the plasma particles and the electromagnetic fields in plasmas. Likewise, the environment and properties of the plasma, such as the magnetic field and the system boundaries, play important roles for the evolution of plasmas on global scales. Therefore, it is of great importance to study the mechanics of wave–particle resonances, the kinetics of electrons, and the effects of astrophysical environments, in order to advance our understanding of the physics of astrophysical plasmas throughout the universe. This thesis presents a physics-based understanding of the evolution of electrons in the solar wind.

I developed a quasi-linear diffusion model to describe the effects of resonant wave–particle instabilities on the particle velocity distribution. This model enables us to understand how the particles in a non-relativistic plasma, such as the solar wind and the magnetosphere, lose kinetic energy through unstable and resonant waves. This is important because wave–particle interactions are a key energy-transfer mechanism in plasma systems and thus affect and even determine the large-scale evolution of these systems.

I also derived a kinetic transport equation that enables us to model the kinetic expansion of electrons in a steady-state magnetic field resulting from a spherically symmetric plasma outflow. This is important for all astrophysical plasma outflows because they are determined by the same interplay between global gradients and

local kinetic processes.

The third part of my thesis provides a detailed study of the occurrence of a resonant instability in the solar wind. Electrons play a very important role for the heat conduction in all collisionless plasmas. Although instabilities can regulate this heat conduction, it is not known when and how often these instabilities actually work. Therefore, this third part of my thesis is an important contribution to the understanding of the heat conduction in collisionless plasma in general.

Electrons account for over 50% of the charged particles in plasmas and guarantee quasi-neutrality. This makes them a critical component of all plasmas. Therefore, understanding the solar-wind electrons is central to understanding the evolution of the solar wind itself. My research supports the development of successful solar-wind prediction models for space weather. Space weather is a major natural hazard. It can cause problems for satellite communication and air traffic, destroy satellites, and even cause major power outages.

My mathematical approaches are applicable to other physics and mathematical problems. My extended Crank–Nicolson approach can describe general diffusion processes such as random-walk propagation of energetic particles, heat conduction in solid media, or Brownian particle motion. Moreover, it can solve the Black—Scholes equation which is used in the financial industry to determine the fair price or theoretical value for an option.

Acknowledgements

First of all, Dr. Daniel Verscharen has been the primary supervisor since my MSc at UCL. I would like to express my gratitude to him for my thesis work and guidance in all of my scientific questions. He has always made a positive and educative atmosphere. He has guided me to develop the necessary framework for my research while he has always left me with the freedom in deciding the direction and method of research. Thanks to his deep knowledge and wide experience of the field, I could always enjoy discussing the physics and mathematics with him and this thesis could be completed in its present form.

The support by Dr. Robert T. Wicks and Prof. Andrew N. Fazakerley in panel meetings is also enormously appreciated. I would like to express my gratitude to them for their outstanding advice on my PhD work based on different perspectives.

The great knowledge on the heliospheric plasma physics from Dr. Christian Vocks has been very fruitful. I would like to thank him for his valuable advice on my thesis work. Without his advice, this thesis would have taken a longer time.

I appreciate the members of the "Joint Electron Project" at MSSL for the support of the data analysis. I express my gratitude to Joel B. Abraham, Dr. Laura Berčič, Prof. Christopher J. Owen and Dr. David Stansby for their help with PSP, Solar Orbiter and Helios data to consolidate my theoretical work. I also thank Dr. Georgios Nicolaou and Jeffersson A. Agudelo Rueda for the discussions on physics and social topics.

I am grateful for the time that I have spent during my PhD with Dr. Colin Forsyth, Dr. Jonathan Rae, Dr. Jasmine Kaur Sandhu, Dr. Andy Smith, Mayur Bakrania, Caoimhe Doherty, Dr. Frances Staples, Sam Walton and Dr. Michaela

Mooney in the space plasma group. They have always created a pleasant atmosphere for our group. I also enormously thank Diego de Pablos because he has helped with all technical problems with my computer.

Lastly, I would like to appreciate my parents for their great support. Thanks to their full financial support and trust in me, I have been able to focus on my PhD work and complete this thesis. I express my respect to their patience and efforts. I also would like to thank my older sisters for their kind support during all the time. This thesis is dedicated to my family.

Publications

The following peer-reviewed publications resulted from this thesis:

- **Jeong, S. -Y.**, Abraham, J. B., Verscharen, D., Berčič, L., Stansby, D., Nicolaou, G., Owen, C. J., Wicks, R. T., Fazakerley, A. N., Agudelo Rueda, J. A. and Bakrania, M.: *The Stability of the Electron Strahl against the Oblique Fast-magnetosonic/Whistler Instability in the Inner Heliosphere*, Astrophys. J. Lett., 926, 2, L26, 2022

- **Jeong, S. -Y.**, Verscharen, D., Vocks, C., Abraham, J. B., Owen, C. J., Wicks, R. T., Fazakerley, A. N., Stansby, D., Berčič, L., Nicolaou, G., Agudelo Rueda, J. A. and Bakrania, M.: *The Kinetic Expansion of Solar-Wind Electrons: Transport Theory and Predictions for the very Inner Heliosphere*, Astrophys. J., 927, 2, 162, 2022

- Abraham, J. B., Owen, C. J., Verscharen, D., Bakrania, M., Stansby, D., Wicks, R. T., Nicolaou, G., Agudelo Rueda, J. A., **Jeong, S. -Y.**, Whittlesey, P. L. and Berčič, L.: *Radial evolution of thermal and suprathermal electron populations in the slow solar wind from 0.13 to 0.5 au using Machine learning: Parker Solar Probe Observations*, Astrophys. J., submitted, 2021

- **Jeong, S. -Y.**, Verscharen, D., Wicks, R. T. and Fazakerley, A. N.: *A Quasi-linear Diffusion Model for Resonant Wave–Particle Instability in Homogeneous Plasma*, Astrophys. J., 902, 2, 128, 2020

- Verscharen, D., Chandran, B. D. G., **Jeong, S. -Y.**, Salem, C. S., Pulupa, M. P. and Bale, S. D.: *Self-induced Scattering of Strahl Electrons in the Solar Wind*, Astrophys. J., 886, 2, 136, 2019

Contents

List of Figures

Chapter 1

Introduction to Kinetic Plasma Physics

Kinetic plasma physics describes and predicts the conditions of space plasma based on the microscopic motion of the particles. It provides a fundamental insight for space plasma physics and links to the framework of magnetohydrodynamics (MHD). In the heliosphere, the solar-wind plasma experiences a variety of kinetic phenomena. Due to the low collisionality of the solar wind, the particle VDF is typically not in local Maxwellian thermodynamic equilibrium, and separated into different populations of particles in the VDF (Marsch, 2006). Therefore, kinetic plasma physics is of great importance for the theoretical description of many phenomena in the solar-wind plasma that are related to the non-Maxwellian features of electron and ion VDFs.

1.1 Velocity Distribution Function and Boltzmann Equation

To statistically describe the density of charged particles in phase space, kinetic physics treats the particle VDF which is defined as

$$f_j(\mathbf{x},\mathbf{v},t) = \frac{dN}{d^3\mathbf{x}d^3\mathbf{v}}, \tag{1.1}$$

where dN is the number of particles of population j in the six-dimensional phase-space volume element ($d^3\mathbf{x}d^3\mathbf{v}$) at time t, the vectors $\mathbf{v}$ and $\mathbf{x}$ indicate the velocity and configuration coordinates. We assume that the number of particles is large enough to guarantee that f_j is a continuous function of $\mathbf{x}$, $\mathbf{v}$ and t. The particle VDF f_j also describes the bulk properties of each particle population j through its velocity moments. The zeroth velocity moment of f_j corresponds to the particle density

$$n_j = \int f_j d^3\mathbf{v}. \tag{1.2}$$

The first velocity moment of f_j corresponds to the bulk velocity

$$\mathbf{U}_j = \frac{1}{n_j}\int \mathbf{v} f_j d^3\mathbf{v}. \tag{1.3}$$

The second velocity moment of f_j corresponds to the pressure tensor

$$\overleftrightarrow{\mathbf{P}}_j = m_j \int (\mathbf{v}-\mathbf{U}_j)(\mathbf{v}-\mathbf{U}_j) f_j d^3\mathbf{v}, \tag{1.4}$$

where m_j is the mass of a particle of population j, and $(\mathbf{v}-\mathbf{U}_j)(\mathbf{v}-\mathbf{U}_j)$ is the dyadic product. The third velocity moment of f_j corresponds to the heat-flux tensor

$$\overleftrightarrow{\mathbf{Q}}_j = m_j \int (\mathbf{v}-\mathbf{U}_j)(\mathbf{v}-\mathbf{U}_j)(\mathbf{v}-\mathbf{U}_j) f_j d^3\mathbf{v}. \tag{1.5}$$

Lastly, the kinetic energy density is defined as

$$W_j = \frac{1}{2} m_j \int (\mathbf{v}\cdot\mathbf{v}) f_j d^3\mathbf{v}. \tag{1.6}$$

In this way, the particle VDF describes the full state of the plasma particles.

Even though measurements often show irregular distribution functions in the solar wind, analytical distribution functions are widely used to model the solar-wind evolution. Typically, there are four standard and "gyrotropic" distribution functions. A Maxwellian distribution function in the solar-wind frame represents

isotropic plasma in thermodynamic equilibrium:

$$f_j^M = \frac{n_j}{\pi^{3/2} v_{th,j}^3} \exp\left(-\frac{v^2}{v_{th,j}^2}\right), \tag{1.7}$$

where

$$v^2 = v_\perp^2 + v_\parallel^2 \tag{1.8}$$

and

$$v_{th,j} \equiv \sqrt{\frac{2k_B T_j}{m_j}}. \tag{1.9}$$

Note that the cylindrical velocity coordinate is $(v_\perp, \phi_v, v_\parallel)$ where $v_\perp$ and $v_\parallel$ are the components of the velocity $\mathbf{v}$ perpendicular and parallel with respect to the local background magnetic field, ϕ_v is the azimuthal angle of $\mathbf{v}$, T_j is the temperature of population j, and k_B is the Boltzmann constant. To account for temperature anisotropies, a bi-Maxwellian distribution function in the solar-wind frame is often defined as

$$f_j^{bM} = \frac{n_j}{\pi^{3/2} v_{\perp th,j}^2 v_{\parallel th,j}} \exp\left(-\frac{v_\perp^2}{v_{\perp th,j}^2} - \frac{v_\parallel^2}{v_{\parallel th,j}^2}\right), \tag{1.10}$$

where

$$v_{\perp th,j} \equiv \sqrt{\frac{2k_B T_{\perp j}}{m_j}}, \tag{1.11}$$

$$v_{\parallel th,j} \equiv \sqrt{\frac{2k_B T_{\parallel j}}{m_j}}, \tag{1.12}$$

and $T_{\perp j}$ and $T_{\parallel j}$ are the temperatures of population j perpendicular and parallel with respect to the local background magnetic field. As a more generalised distribution function that allows for superthermal tails, non-extensive statistical mechanics leads to the κ-distribution function in the solar-wind frame (Livadiotis and McComas, 2009; Livadiotis and McComas, 2013; Nicolaou and Livadiotis, 2016):

$$f_j^\kappa = \frac{n_j}{v_{th,j}^3} \left[\frac{2}{\pi(2\kappa-3)}\right]^{3/2} \frac{\Gamma(\kappa+1)}{\Gamma(\kappa-0.5)} \left(1 + \frac{2}{2\kappa-3}\frac{v^2}{v_{th,j}^2}\right)^{-\kappa-1}, \tag{1.13}$$

where $\Gamma(x)$ is the Γ-function and $\kappa > 3/2$ is the κ-index. The κ-distribution transitions into the Maxwellian distribution in the limit

$$\lim_{\kappa\to\infty} f_j^{\kappa} = f_j^{M}. \tag{1.14}$$

To account for temperature anisotropies in κ-distribution functions, analogously to the bi-Maxwellian distribution function, a bi-κ-distribution function is described as

$$\begin{aligned} f_j^{b\kappa} = \frac{n_j}{v_{\perp th,j}^2 v_{\parallel th,j}} \left[\frac{2}{\pi(2\kappa-3)}\right]^{3/2} \frac{\Gamma(\kappa+1)}{\Gamma(\kappa-0.5)} \\ \times \left[1+\frac{2}{2\kappa-3}\left(\frac{v_\perp^2}{v_{\perp th,j}^2}+\frac{v_\parallel^2}{v_{\parallel th,j}^2}\right)\right]^{-\kappa-1}. \end{aligned} \tag{1.15}$$

These four standard and gyrotropic distribution functions are often used to describe the particle distribution functions not only in the corona where Coulomb collisions are relatively frequent, but also in the solar wind. Moreover, least-squares fitting of measured distributions by these standard distributions is often used to characterise the plasma and to separate the measured distribution function into different populations of particles.

To compute the evolution of the particle VDF through the electromagnetic force and Coulomb collisions, the Boltzmann equation is most widely used in kinetic plasma physics (Stix, 1992):

$$\frac{\partial f_j}{\partial t} + \mathbf{v}\cdot\nabla_{\mathbf{x}} f_j + \frac{q_j}{m_j}\left[\mathbf{E}+\frac{\mathbf{v}}{c}\times\mathbf{B}\right]\cdot\nabla_{\mathbf{v}} f_j = \left(\frac{\partial f_j}{\partial t}\right)_{\text{col}}, \tag{1.16}$$

where q_j is the charge of a particle of population j, c is the light speed in vacuum, and $\mathbf{E}$ and $\mathbf{B}$ are the electric and magnetic fields. The fields $\mathbf{E}$ and $\mathbf{B}$ obey Maxwell's equations:

$$\nabla_{\mathbf{x}}\cdot\mathbf{E} = 4\pi\rho_q, \tag{1.17}$$

$$\nabla_{\mathbf{x}}\cdot\mathbf{B} = 0, \tag{1.18}$$

$$\nabla_{\mathbf{x}}\times\mathbf{E} = -\frac{1}{c}\frac{\partial\mathbf{B}}{\partial t}, \tag{1.19}$$

and

$$\nabla_{\mathbf{x}} \times \mathbf{B} = \frac{4\pi}{c}\mathbf{J} + \frac{1}{c}\frac{\partial \mathbf{E}}{\partial t}, \tag{1.20}$$

where

$$\rho_q = \sum_j q_j \int f_j d^3\mathbf{v}, \tag{1.21}$$

and

$$\mathbf{J} = \sum_j q_j \int \mathbf{v} f_j d^3\mathbf{v}. \tag{1.22}$$

The term on the right-hand side of Eq. (1.16) corresponds to the Coulomb collision operator. The full Boltzmann equation, Eq. (1.16), combined with the set of Maxwell's equations, describes the self-consistent response of charged particles to the electromagnetic force with Coulomb-collisional effects in a conducting medium. Since our work focuses on non-relativistic space plasma like the solar wind, we neglect relativistic effects throughout our study.

By taking the velocity moments of Eq. (1.16), we evaluate the evolution of the bulk properties of the particle VDF, which is the basis of MHD theory. Moreover, we use Eq. (1.16) to clarify the effects of wave-particle interactions on the particle VDF, which is a local kinetic process in the heliosphere (see sections 1.2, 1.3 and 3). Probability theory for collisions realises the right-hand side of Eq. (1.16), which describes the effect of a large number of random Coulomb collisions on the particle VDF with time (see section 1.4). On the global scale of the heliosphere, Eq. (1.16) describes the full evolution of the solar wind. In that case, it accounts for the gradient of the background electric and magnetic fields and particle temperature. However, global kinetic models of the heliosphere based on the six-dimensional Eq. (1.16) are not feasible with current numerical resources. Therefore, we derive a three-dimensional kinetic transport equation for our global kinetic model (see Chapter 4).

1.2 Linear Theory

The presence of the static background magnetic field leads to many kinetic phenomena in a hot plasma. In this chapter, we discuss linear waves with small amplitudes

in a hot magnetised plasma. Wave-particle interactions are an important effect in linear kinetic theory. In wave-particle interactions, a subset of charged particles with a specific velocity experiences the wave electric field as a static electric field. Under such circumstances, these resonant particles lose or gain energy, depending on the resonant wave characteristics.

To analyse the resonant wave characteristics in a hot magnetised plasma, linear theory derives the kinetic dispersion relation which connects the wave vector and frequency as self-consistent solutions to the linearised Eq. (1.16) and Maxwell's equations, given as Eqs. (1.17) $\sim$ (1.20). The kinetic dispersion relation is a cornerstone for the determination of the wave properties as a fundamental and important plasma process. Thus, by solving the kinetic dispersion relation, the resonant wave characteristics can be analysed. The following derivation of the kinetic dispersion relation is to understand the underlying assumptions of linear theory. The mathematics of the following derivation is explained in great detail by Gurnett and Bhattacharjee (2017).

In linear theory, we assume that the amplitude of the wave is small and that the background plasma is homogeneous. Then, the electric and magnetic fields in Eq. (1.16) are expressed as

$$\mathbf{B} = \mathbf{B}_0 + \mathbf{B}_\mathbf{r}, \tag{1.23}$$

and

$$\mathbf{E} = \mathbf{E}_\mathbf{r}, \tag{1.24}$$

where $\mathbf{B}_0$ is the local background magnetic field, and $\mathbf{B}_\mathbf{r}$ and $\mathbf{E}_\mathbf{r}$ are the magnetic and electric fields of the waves and very small perturbed first-order terms. It is also logical to express the particle VDF by a spatially and temporally uniform zeroth-order VDF plus a small perturbed first-order VDF as

$$f_j(\mathbf{x},\mathbf{v},t) = f_{0j}(\mathbf{v}) + f_{1j}(\mathbf{x},\mathbf{v},t). \tag{1.25}$$

In linear theory, we assume that the plasma is collisionless, which means that $(\partial f_j/\partial t)_{\mathrm{col}} = 0$ in Eq. (1.16). Applying Eqs. (1.23)$\sim$(1.25) to Eq. (1.16), the

zeroth-order terms in Eq. (1.16) provide the gyrotropic condition of f_{0j} (i.e., $\partial f_{0j}/\partial \phi_v = 0$).

For the analysis of the effects of the perturbed electromagnetic fields on the VDF, retaining only the first-order terms in Eq. (1.16) leads to:

$$\frac{\partial f_{1j}}{\partial t} + \mathbf{v}\cdot\nabla_{\mathbf{x}} f_{1j} + \frac{q_j}{m_j}\left(\frac{\mathbf{v}}{c}\times\mathbf{B}_0\right)\cdot\nabla_{\mathbf{v}} f_{1j} + \frac{q_j}{m_j}\left(\mathbf{E_r} + \frac{\mathbf{v}}{c}\times\mathbf{B_r}\right)\cdot\nabla_{\mathbf{v}} f_{0j} = 0. \quad (1.26)$$

The third term in Eq. (1.26) becomes

$$\frac{q_j}{m_j}\left(\frac{\mathbf{v}}{c}\times\mathbf{B}_0\right)\cdot\nabla_{\mathbf{v}} f_{1j} = \Omega_j\left(v_y\frac{\partial f_{1j}}{\partial v_x} - v_x\frac{\partial f_{1j}}{\partial v_y}\right), \quad (1.27)$$

where the cyclotron frequency of population j is defined as $\Omega_j \equiv q_j B_0/m_j c$. Note that $v_x = v_\perp\cos\phi_v$, $v_y = v_\perp\sin\phi_v$ and $v_z = v_\parallel$. Then, Eq. (1.27) becomes

$$\begin{aligned}\frac{q_j}{m_j}\left(\frac{\mathbf{v}}{c}\times\mathbf{B}_0\right)\cdot\nabla_{\mathbf{v}} f_{1j} &= \Omega_j\left(v_\perp\sin\phi_v\frac{\partial f_{1j}}{\partial v_x} - v_\perp\cos\phi_v\frac{\partial f_{1j}}{\partial v_y}\right)\\ &= -\Omega_j\left(\frac{\partial v_x}{\partial\phi_v}\frac{\partial f_{1j}}{\partial v_x} + \frac{\partial v_y}{\partial\phi_v}\frac{\partial f_{1j}}{\partial v_y}\right)\\ &= -\Omega_j\frac{\partial f_{1j}}{\partial\phi_v},\end{aligned} \quad (1.28)$$

which replaces the third term of Eq. (1.26).

When analysing the linearised equation, it is more convenient to work in Fourier space. The formula of the Fourier transform in three-dimensional space and in time for an arbitrary function $F(\mathbf{x},t)$ is

$$\tilde{F}(\mathbf{k},\omega) = \frac{1}{(2\pi)^2}\int F(\mathbf{x},t)\exp\left[-i(\mathbf{k}\cdot\mathbf{x}-\omega t)\right]d^3\mathbf{x}dt, \quad (1.29)$$

where $\mathbf{k}\cdot\mathbf{x} = k_\perp x\cos\phi_k + k_\perp y\sin\phi_k + k_\parallel z$ and ω is the wave frequency which is a complex function of the wavevector $\mathbf{k}$. The cylindrical wavevector coordinates are $(k_\perp,\phi_k,k_\parallel)$ where $k_\perp$ and $k_\parallel$ are the components of the wavevector $\mathbf{k}$ perpendicular and parallel with respect to the local background magnetic field, and ϕ_k is the azimuthal angle of $\mathbf{k}$. After applying Eq. (1.29) to Eq. (1.26), a linear differential

equation for $\tilde{f}_{1j}$, which is the Fourier-transformed f_{1j}, is given as

$$(-i\omega + i\mathbf{k}\cdot\mathbf{v})\tilde{f}_{1j} - \Omega_j \frac{\partial \tilde{f}_{1j}}{\partial \phi_v} = -\frac{q_j}{m_j}\left(\tilde{\mathbf{E}}_\mathbf{r} + \frac{\mathbf{v}}{c}\times\tilde{\mathbf{B}}_\mathbf{r}\right)\cdot\nabla_\mathbf{v} f_{0j} \tag{1.30}$$

where $\tilde{\mathbf{E}}_\mathbf{r}$ and $\tilde{\mathbf{B}}_\mathbf{r}$ are the Fourier-transformed $\mathbf{E}_\mathbf{r}$ and $\mathbf{B}_\mathbf{r}$. By applying Eq. (1.29) to Eqs. (1.19) and (1.20), we express the perturbed first-order Maxwell's equations

$$\mathbf{k}\times\tilde{\mathbf{E}}_\mathbf{r} = \frac{\omega}{c}\tilde{\mathbf{B}}_\mathbf{r} \tag{1.31}$$

and

$$i\mathbf{k}\times\tilde{\mathbf{B}}_\mathbf{r} = \frac{4\pi}{c}\tilde{\mathbf{J}}_1 - \frac{i\omega}{c}\tilde{\mathbf{E}}_\mathbf{r}, \tag{1.32}$$

where $\tilde{\mathbf{J}}_1$ is the perturbed first-order current density. Eq. (1.31) replaces $\tilde{\mathbf{B}}_\mathbf{r}$ with $\tilde{\mathbf{E}}_\mathbf{r}$ in Eqs. (1.30) and (1.32). Because the plasma is gyrotropic on average, we assume that $\mathbf{k}$ is in the xz-plane without loss of generality, leading to $\mathbf{k}\cdot\mathbf{v} = k_\parallel v_\parallel + k_\perp v_\perp \cos\phi_v$. Then, Eq. (1.30) becomes

$$\frac{\partial \tilde{f}_{1j}}{\partial \phi_v} - i(\alpha_j + \beta_j\cos\phi_v)\tilde{f}_{1j} = \frac{q_j}{m_j\Omega_j}\left[\tilde{\mathbf{E}}_\mathbf{r} + \mathbf{v}\times\left(\frac{\mathbf{k}\times\tilde{\mathbf{E}}_\mathbf{r}}{\omega}\right)\right]\cdot\nabla_\mathbf{v} f_{0j}, \tag{1.33}$$

where $\alpha_j = (k_\parallel v_\parallel - \omega)/\Omega_j$ and $\beta_j = k_\perp v_\perp/\Omega_j$. By solving Eq. (1.33), we obtain $\tilde{f}_{1j}$, expressed in terms of $\tilde{\mathbf{E}}_\mathbf{r}$ where $\tilde{\mathbf{E}}_\mathbf{r} = \hat{x}\tilde{E}_r^x + \hat{y}\tilde{E}_r^y + \hat{z}\tilde{E}_r^z$, as follows:

$$\begin{aligned}\tilde{f}_{1j} =& i\frac{q_j}{m_j\Omega_j}\sum_{m,n}\frac{\exp[i(m-n)\phi_v]}{\alpha_j + n}J_m(\beta_j) \\ &\times\left[\left(\frac{n}{\beta_j}J_n(\beta_j)\tilde{E}_r^x + iJ_n'(\beta_j)\tilde{E}_r^y\right)A_j + J_n(\beta_j)B_j\tilde{E}_r^z\right],\end{aligned} \tag{1.34}$$

where

$$A_j = \frac{\partial f_{0j}}{\partial v_\perp} + \frac{k_\parallel}{\omega}\left(v_\perp\frac{\partial f_{0j}}{\partial v_\parallel} - v_\parallel\frac{\partial f_{0j}}{\partial v_\perp}\right) \tag{1.35}$$

and

$$B_j = \frac{\partial f_{0j}}{\partial v_\parallel} - \frac{n\Omega_j}{\omega v_\perp}\left(v_\perp\frac{\partial f_{0j}}{\partial v_\parallel} - v_\parallel\frac{\partial f_{0j}}{\partial v_\perp}\right). \tag{1.36}$$

We denote the n^{th}-order Bessel function as $J_n(\beta_j)$, with the property $J_{n+1}(\beta_j) -$

$J_{n-1}(\beta_j) = -2J'_n(\beta_j)$. Then, Eq. (1.34) is used to express the perturbed first-order current density as

$$\tilde{\mathbf{J}}_1 = \overleftrightarrow{\sigma} \cdot \tilde{\mathbf{E}}_\mathbf{r} = \sum_j q_j \int \mathbf{v} \tilde{f}_{1j} d^3\mathbf{v}, \tag{1.37}$$

where $\overleftrightarrow{\sigma}$ is the 3×3 conductivity tensor, which is found by comparing with the right-hand side of Eq. (1.37). By substituting Eq. (1.37) into Eq. (1.32), the wave equation in a homogeneous plasma is given as

$$\mathbf{k} \times \mathbf{k} \times \tilde{\mathbf{E}}_\mathbf{r} + \frac{\omega^2}{c^2} \overleftrightarrow{\varepsilon} \cdot \tilde{\mathbf{E}}_\mathbf{r} = 0, \tag{1.38}$$

where

$$\overleftrightarrow{\varepsilon} = \overleftrightarrow{\mathbf{I}} - \frac{4\pi \overleftrightarrow{\sigma}}{i\omega} \tag{1.39}$$

is the dielectric tensor, which describes the properties of the electromagnetic waves and charged particles in a conducting medium. $\overleftrightarrow{\mathbf{I}}$ is the 3×3 identity tensor. Eq. (1.39) is a function of ω, $k_\perp$ and $k_\parallel$ and the plasma parameters.

The hot plasma dispersion relation describes all non-trivial solutions of Eq. (1.38), shown in great detail by Gurnett and Bhattacharjee (2017). This dispersion relation provides much information about the resonance properties between waves and particles. We define ω_k and γ_k as the real and imaginary parts of ω, (i.e., $\omega = \omega_k + i\gamma_k$) at wavevector $\mathbf{k}$. The growth/damping rate γ_k is directly retrieved from the dispersion relation. Considering that

$$\mathbf{E}_\mathbf{r} \sim \exp(-i\omega t) = \exp[-i\omega_k t + \gamma_k t], \tag{1.40}$$

if the growth rate is positive, the resonant wave grows exponentially with time. The required energy for this process comes from resonant particles in linear theory. On the other hand, if the growth rate is negative, the resonant wave is damped exponentially with time and the energy transfers to the resonant particles. In order to describe a realistic enhancement or dampening of propagating resonant wave modes, it is reasonable to assume that the growth rate must be much smaller than the real wave frequency at the initial time, which is known as a weak-growth-rate

approximation:

$$|\omega_k| \gg |\gamma_k|. \tag{1.41}$$

The derivation of the growth rate under this assumption is given in the seminal work by Kennel and Wong (1967).

In the case of resonant wave instabilities, the dispersion relation provides resonant wave properties, such as the range of wave vector where the growth rate is positive and the unstable resonant wave is driven. At the same time, the dispersion relation provides the resonant wave frequency, ω_k, of the instability. It is most interesting to study ω_k where the dispersion relation has the largest growth rates because these wave modes will quickly dominate the fluctuation spectrum over time. However, linear theory is fundamentally based on the assumption that the wave amplitude is very small. Therefore, the results from linear theory are only valid initially until the amplitude grows to a significant value. In addition, due to a diffusion process of particles in velocity space through instabilities, the initial VDF is deformed over time (see section 1.3). This means that the dispersion relation must be updated based on such deformed VDF. Quasi-linear theory describes this diffusion process in the VDF under the action of a wave instability. It can thus capture the nonlinear saturation of the instability due to changes in the background distribution f_{0j}.

In general, the non-trivial solutions of Eq. (1.38) for the dispersion relation are analytically intractable because they contain an infinite number of Bessel functions and propagation modes. Therefore, for our applications in Chapter 3, we use the New Hampshire Dispersion relation Solver (NHDS; Verscharen and Chandran, 2018) which numerically solves the dispersion relation.

1.3 Quasi-Linear Theory

Quasi-linear theory is fundamentally different from linear theory due to the different underlying assumptions. In linear theory, the VDF is set to Eq. (1.25). Hence, the spatially and temporally uniform zeroth-order VDF, $f_{0j}(\mathbf{v})$, is always constant in time even if the small perturbed first-order VDF, $f_{1j}(\mathbf{x},\mathbf{v},t)$, grows significantly through, for example, a wave-particle resonance. A significant growth of the per-

turbed VDF would invalidate the small-perturbation assumption. Thus, a permanently constant $f_{0j}(\mathbf{v})$ is not realistically true in the long-term evolution of kinetic instabilities. Quasi-linear theory allows that when $f_{1j}(\mathbf{x},\mathbf{v},t)$ undergoes resonances, $f_{0j}(\mathbf{v})$ slowly changes and, in turn, the changed $f_{0j}(\mathbf{v})$ provides the evolving background for $f_{1j}(\mathbf{x},\mathbf{v},t)$. To mathematically describe this scenario, the spatially and temporally uniform zeroth-order VDF, $f_{0j}(\mathbf{v})$, in Eq. (1.25) is replaced by the spatially averaged VDF:

$$f_j(\mathbf{x},\mathbf{v},t) = \left\langle f_j \right\rangle(\mathbf{v},t) + f_{1j}(\mathbf{x},\mathbf{v},t). \tag{1.42}$$

The angular bracket indicates the spatial average. Eq. (1.42) suggests that the spatial average of $f_{1j}(\mathbf{x},\mathbf{v},t)$ should be always zero while the averaged zeroth-order VDF, $\left\langle f_j \right\rangle(\mathbf{v},t)$, evolves with time. As an important point, quasi-linear theory assumes that the time evolution of $\left\langle f_j \right\rangle(\mathbf{v},t)$ occurs on a timescale that is much slower than the gyroperiod of the particles and the wave period.

To develop an equation for the evolution of $\left\langle f_j \right\rangle(\mathbf{v},t)$ through wave–particle resonance in time, we apply spatial and gyro-phase averages to Eq. (1.16), underlying Eq. (1.42) and without the Coulomb collision operator. In this procedure, three assumptions are made. First, $\nabla_{\mathbf{x}} f_{1j}(\mathbf{x},\mathbf{v},t)$ is perfectly differential in space and vanishes at very large distances, $\mathbf{x}$: $\left\langle \nabla_{\mathbf{x}} f_{1j} \right\rangle = 0$. Second, the spatial average of the first-order electromagnetic fields is zero: $\langle \mathbf{E_r} \rangle = \langle \mathbf{B_r} \rangle = 0$. Lastly, $\left\langle f_j \right\rangle(\mathbf{v},t)$ is always gyrotropic: $\partial \left\langle f_j \right\rangle / \partial \phi_v = 0$. Following this procedure and under these assumptions, Eq. (1.16) becomes

$$\frac{\partial \left\langle f_j \right\rangle(\mathbf{v},t)}{\partial t} = -\frac{q_j}{m_j}\frac{1}{2\pi}\int_0^{2\pi} \left\langle \nabla_{\mathbf{v}} \cdot \left[\left(\mathbf{E_r} + \frac{\mathbf{v}}{c} \times \mathbf{B_r} \right) f_{1j} \right] \right\rangle d\phi_v. \tag{1.43}$$

Applying sophisticated vector analysis, which is explained in great detail by Stix

(1992), Eq. (1.43) yields

$$\left(\frac{\partial f_j}{\partial t}\right)_{\mathrm{QLD}} = \lim_{V\to\infty} \sum_{n=-\infty}^{\infty} \int \frac{\pi q_j^2}{V m_j^2} \times \hat{G}[k_\parallel] \left[\frac{v_\perp^2}{|v_\parallel|} \delta\left(k_\parallel - \frac{\omega_k - n\Omega_j}{v_\parallel} \right) \left|\psi_j^n\right|^2 \hat{G}[k_\parallel] f_j \right] d^3\mathbf{k}, \tag{1.44}$$

where

$$\psi_j^n \equiv \frac{1}{\sqrt{2}} \left[\tilde{E}_r^R e^{i\phi_k} J_{n+1}(\beta_j) + \tilde{E}_r^L e^{-i\phi_k} J_{n-1}(\beta_j) \right] + \frac{v_\parallel}{v_\perp} \tilde{E}_r^z J_n(\beta_j), \tag{1.45}$$

and

$$\hat{G}[k_\parallel] \equiv \left(1 - \frac{k_\parallel v_\parallel}{\omega_k}\right) \frac{1}{v_\perp} \frac{\partial}{\partial v_\perp} + \frac{k_\parallel}{\omega_k} \frac{\partial}{\partial v_\parallel}. \tag{1.46}$$

From this moment on, we simply denote $\left\langle f_j(\mathbf{v},t) \right\rangle$ as $f_j(v_\perp, v_\parallel, t)$ which is spatially averaged and gyrotropic. Eq. (1.44) is the quasi-linear diffusion equation first established by Yakimenko (1963) and Kennel and Engelmann (1966), and describes the diffusion of resonant particles with time in velocity space. The integer n determines the order of the resonance, where $n = 0$ corresponds to the Landau resonance and $n \neq 0$ corresponds to cyclotron resonances. In our equations, we label contributions from a given resonance order with a superscript n. Eq. (1.44) is all valid in any coordinate system, but we will from now on work in a coordinate system in which the protons are at rest. V is the volume in which the wave amplitude is effective so that the wave and particles undergo a significant interaction. We denote Dirac's δ-function as δ. Without loss of generality, we set $\omega_k > 0$. We assume that $\omega_k \gg |\gamma_k|$ as in Eq. (1.41) (i.e. the assumption of slow growth or damping that is central to linear and quasi-linear theory). We take the constant background magnetic field as $\mathbf{B}_0 = \hat{z}B_0$ and define the right- and left-circularly polarized components of the electric field as $\tilde{E}_r^R \equiv (\tilde{E}_r^x - i\tilde{E}_r^y)/\sqrt{2}$ and $\tilde{E}_r^L \equiv (\tilde{E}_r^x + i\tilde{E}_r^y)/\sqrt{2}$. We define the longitudinal component of the electric field as $\tilde{E}_r^z$.

To analyse Eq. (1.44), we require the parameters of the resonant waves which are given by linear theory. Therefore, linear theory explains the nature of the reso-

nant waves while quasi-linear theory explains the long-term evolution of the resonant particles. For a full explanation of wave–particle resonances, these two theories must be linked with each other.

1.4 Probability Theory for Coulomb Collisions

Even though Coulomb collisions are negligible on the timescale of local events such as wave-particle interactions, Coulomb collisions can affect the VDF on the timescale of solar-wind expansion and near the corona. It is well known that many small pitch-angle Coulomb collisions contribute to the deflection of charged particles instead of one large pitch-angle Coulomb collision (Rosenbluth et al., 1957; Gurnett and Bhattacharjee, 2017). The trajectory of a charged particle is complicated in a plasma due to the large number of randomly directed collision impacts on large timescales. Accordingly, a statistical analysis is necessary and the concept of a probability distribution function, $P_j(\mathbf{v},\Delta\mathbf{v})$, is introduced. The mathematics for the following derivation is explained in more detail by Gurnett and Bhattacharjee (2017).

$P_j(\mathbf{v},\Delta\mathbf{v})d^3(\Delta\mathbf{v})$ is the probability that a test particle of species j with velocity $\mathbf{v}$ at time t experiences a change of its velocity by $\Delta\mathbf{v}$ during the time Δt due to small pitch-angle Coulomb collisions. In probability theory, the normalisation of the probability function must be satisfied:

$$\int_{-\infty}^{\infty} P_j(\mathbf{v},\Delta\mathbf{v})d^3(\Delta\mathbf{v}) = 1. \tag{1.47}$$

An equation to describe the diffusion process of $f_j(\mathbf{x},\mathbf{v},t)$ in velocity space due to Coulomb collisions in time is developed by using $P_j(\mathbf{v},\Delta\mathbf{v})$. If $f_j(\mathbf{x},\mathbf{v}-\Delta\mathbf{v},t-\Delta t)$ at time $t-\Delta t$ evolves into $f_j(\mathbf{x},\mathbf{v},t)$ at time t through Coulomb collisions, the present $f_j(\mathbf{x},\mathbf{v},t)$ is expressed by

$$f_j(\mathbf{x},\mathbf{v},t) = \int_{-\infty}^{\infty} f_j(\mathbf{x},\mathbf{v}-\Delta\mathbf{v},t-\Delta t)P_j(\mathbf{v},\Delta\mathbf{v})d^3(\Delta\mathbf{v}). \tag{1.48}$$

By assuming that $t \gg \Delta t$ and $|\mathbf{v}| \gg |\Delta\mathbf{v}|$, and expanding $f_j(\mathbf{x},\mathbf{v}-\Delta\mathbf{v},t-\Delta t)$ in

Eq. (1.48), we obtain

$$f_j(\mathbf{x},\mathbf{v},t) = \int_{-\infty}^{\infty} \Bigg[f_j(\mathbf{x},\mathbf{v},t)P_j(\mathbf{v},\Delta\mathbf{v}) - \Delta t \frac{\partial f_j(\mathbf{x},\mathbf{v},t)}{\partial t} P_j(\mathbf{v},\Delta\mathbf{v}) \\ -\Delta\mathbf{v}\cdot\nabla_{\mathbf{v}} f_j(\mathbf{x},\mathbf{v},t)P_j(\mathbf{v},\Delta\mathbf{v}) + \frac{1}{2}\Delta\mathbf{v}\Delta\mathbf{v} : \nabla_{\mathbf{v}}\nabla_{\mathbf{v}} f_j(\mathbf{x},\mathbf{v},t)P_j(\mathbf{v},\Delta\mathbf{v}) \Bigg] d^3(\Delta\mathbf{v}). \tag{1.49}$$

We neglect higher-order terms in Eq. (1.49). The single dot ($\cdot$) is the scalar product, and double dots (:) represent the two-fold application of the scalar product to a tensor. Considering Eq. (1.47), the first term on the right-hand side cancels with the term on the left-hand side in Eq. (1.49). Then, by rearranging Δt and using Eq. (1.47), we obtain:

$$\left(\frac{\partial f_j}{\partial t}\right)_{\text{col}} = -\nabla_{\mathbf{v}}\cdot\left[\left\langle\frac{\Delta\mathbf{v}}{\Delta t}\right\rangle_j f_j\right] + \frac{1}{2}\nabla_{\mathbf{v}}\nabla_{\mathbf{v}} : \left[\left\langle\frac{\Delta\mathbf{v}\Delta\mathbf{v}}{\Delta t}\right\rangle_j f_j\right], \tag{1.50}$$

where

$$\left\langle\frac{\Delta\mathbf{v}}{\Delta t}\right\rangle_j = \frac{1}{\Delta t}\int_{-\infty}^{\infty}\Delta\mathbf{v}P_j(\mathbf{v},\Delta\mathbf{v})d^3(\Delta\mathbf{v}), \tag{1.51}$$

and

$$\left\langle\frac{\Delta\mathbf{v}\Delta\mathbf{v}}{\Delta t}\right\rangle_j = \frac{1}{\Delta t}\int_{-\infty}^{\infty}\Delta\mathbf{v}\Delta\mathbf{v}P_j(\mathbf{v},\Delta\mathbf{v})d^3(\Delta\mathbf{v}). \tag{1.52}$$

Eq. (1.50) is known as the Fokker–Planck equation, which describes the diffusion process in velocity space due to Coulomb collisions. It provides us with a representation for the right-hand side of Eq. (1.16). However, this expression is not complete yet since Eqs. (1.51) and (1.52) have not been explicitly defined. Typically, for Eqs. (1.51) and (1.52), we use Rosenbluth potentials (Rosenbluth et al., 1957). Using the Rutherford scattering cross section, Rosenbluth potentials are given by

$$\left\langle\frac{\Delta\mathbf{v}}{\Delta t}\right\rangle_j = -4\pi\sum_b \ln\Lambda_{jb}\frac{(Z_jq_j)^2(Z_bq_b)^2}{\mu_{jb}m_j}\nabla_{\mathbf{v}}\int_{-\infty}^{\infty} f_b\left(\mathbf{v}'\right)\frac{\mathbf{v}-\mathbf{v}'}{|\mathbf{v}-\mathbf{v}'|}d^3\mathbf{v}', \tag{1.53}$$

and

$$\left\langle\frac{\Delta\mathbf{v}\Delta\mathbf{v}}{\Delta t}\right\rangle_j = 4\pi\sum_b \ln\Lambda_{jb}\frac{(Z_jq_j)^2(Z_bq_b)^2}{m_j^2}\nabla_{\mathbf{v}}\nabla_{\mathbf{v}}\int_{-\infty}^{\infty} f_b\left(\mathbf{v}'\right)\left|\mathbf{v}-\mathbf{v}'\right|d^3\mathbf{v}', \tag{1.54}$$

where

$$\Lambda_{jb} = \mu_{jb}\left(\frac{3k_{\mathrm{B}}T_j}{m_j} + \frac{3k_{\mathrm{B}}T_b}{m_b}\right)\left(\frac{\lambda_D}{Z_j Z_b q_j q_b}\right) \tag{1.55}$$

and

$$\mu_{jb} = \frac{m_j m_b}{m_j + m_b}. \tag{1.56}$$

The subscript b indicates the species of background particles, which means that particles of population j Coulomb-collide with particles of population b, and λ_D is the Debye length. The parameters Z_j and Z_b are the charge number of a particle of populations j and b. Considering Eqs. (1.53) and (1.54), Eq. (1.50) becomes

$$\left(\frac{\partial f_j}{\partial t}\right)_{\mathrm{col}} = \sum_b \Gamma_{jb}\left\{-\sum_\alpha \frac{\partial}{\partial v^\alpha}\left(f_j \frac{\partial H_b}{\partial v^\alpha}\right) + \frac{1}{2}\sum_{\alpha,\beta}\frac{\partial^2}{\partial v^\alpha \partial v^\beta}\left(f_j \frac{\partial^2 G_b}{\partial v^\alpha \partial v^\beta}\right)\right\}, \tag{1.57}$$

where

$$G_b = \int f_b(\mathbf{v}')|\mathbf{v}-\mathbf{v}'|d^3\mathbf{v}', \tag{1.58}$$

$$H_b = \frac{m_b - m_j}{m_b}\int f_b(\mathbf{v}')|\mathbf{v}-\mathbf{v}'|^{-1}d^3\mathbf{v}', \tag{1.59}$$

and

$$\Gamma_{jb} = 4\pi\left(\frac{Z_j Z_b q_j q_b}{m_j}\right)^2 \ln\Lambda_{jb}. \tag{1.60}$$

The superscripts α and β indicate the component of the velocity in a given coordinate system, and the summation convention holds. Eq. (1.57) contains the derivatives up to second order in the first term and up to fourth order in the second term. For a more explicit form, Ljepojevic et al. (1990) modify Eq. (1.57) to

$$\left(\frac{\partial f_j}{\partial t}\right)_{\mathrm{col}} = \sum_b \Gamma_{jb}\left\{4\pi\frac{m_j}{m_b}f_b f_j + \sum_\alpha \frac{\partial H_b}{\partial v^\alpha}\frac{\partial f_j}{\partial v^\alpha} + \frac{1}{2}\sum_{\alpha,\beta}\frac{\partial^2 G_b}{\partial v^\alpha \partial v^\beta}\frac{\partial^2 f_j}{\partial v^\alpha \partial v^\beta}\right\}. \tag{1.61}$$

Eq. (1.61) contains the derivatives up to first order in the second term and up to second order in the third term.

Eq. (1.61) is the general form of the Fokker–Planck equation. In Appendix A, we calculate Eq. (1.61) based on the cylindrical velocity space and provide the explicit forms of Rosenbluth potentials, Eqs. (1.58) and (1.59), for our applications

in the following chapters.

Chapter 2

Solar-Wind Electrons

The solar-wind electrons are the most abundant particle species and play important roles for the evolution of the solar wind. They guarantee the overall plasma quasi-neutrality and provide significant heat flux through non-thermal properties of the electron VDF (Pagel et al., 2005). In addition, the solar-wind electrons contribute to the creation of a global ambipolar electric field through their thermal pressure gradient (Jockers, 1970; Lemaire and Scherer, 1970, 1971; Pierrard et al., 1999; Scudder, 2019; Berčič et al., 2021). The central open questions of the solar-wind electrons are the heat-flux regulation and a decrease of the electron temperature slower than expected from the adiabatic expansion law.

2.1 Solar Wind

A hydrostatic equilibrium means the state in which a fluid is in force balance between the pressure-gradient force and gravity. Parker (1958) shows that a hot coronal plasma cannot maintain a hydrostatic equilibrium. The pressure-gradient force predominates over gravity and leads to a radial acceleration of the hot coronal plasma to supersonic velocities. This hot expanding coronal plasma is called the "solar wind". The solar wind is a continuous magnetised plasma that spherically emanates from Sun. It propagates through interplanetary space up to a heliocentric distance of about 90 au, where it transitions from a supersonic flow to a subsonic flow by crossing the solar-wind termination shock (Stone et al., 2005).

The solar-wind plasma consists of positively charged ions and negatively

charged electrons. The solar-wind plasma is in the state of quasi-neutrality in which the number of positive and negative charges is, on sufficiently large scales, equal so that the plasma is neutral on those scales. The dimensions of the solar-wind plasma are significantly greater than the Debye length, which describes the scale on which neighbouring charges of particles mutually shield their Coulomb potentials. The density of the solar-wind plasma in a sphere with the radius of the Debye length is large enough to allow us to neglect the effects of neighbouring particles on each other.

Typically, the solar wind is categorised into two states: fast wind and slow wind, based on its outflow bulk velocity in the heliosphere (Bravo and Stewart, 1997; Feldman et al., 2005). The velocity of fast solar wind ranges from 500km/s to 800km/s while the velocity of slow solar wind ranges from 300km/s to 500km/s. It is generally accepted that the fast solar wind originates from coronal hole regions while the slow wind originates from closed magnetic structures in the corona such as the streamer belt at the solar equator (Phillips et al., 1995; McComas et al., 1998; McComas et al., 2000, 2003; Ebert et al., 2009). On average, the fast solar wind has a lower density than the slow solar wind, and the fast solar wind is collisionless while the slow solar wind is weakly collisional (Livi et al., 1986).

The major open science question in the field of solar-wind physics is the solar-wind heating problem in the heliosphere. According to *in-situ* measurements (Hellinger et al., 2013; Štverák et al., 2015), the measured temperatures of electrons and protons decrease with heliocentric distances more slowly than expected from the adiabatic expansion law. The measured temperatures of electrons and protons are the consequence of combined physical mechanisms, such as Coulomb collisions, wave-particle interactions, magnetic mirror forces, turbulent heating, ambipolar electric field, shocks and potentially additional yet unknown processes. The physics-based understanding for the combination of these physical mechanisms is not complete.

2.2 *In-Situ* Measurements of the Electron VDF

In-situ measurements of the electron VDF in the solar wind reveal multiple deviations from a Maxwellian thermodynamic equilibrium (Pilipp et al., 1987a; Štverák et al., 2009). The electron VDF typically consists of three different electron populations: the core, the halo, and the strahl. The electron core, which accounts for most of the electrons in the solar wind, has a relatively low energy ($\lesssim 50\,\mathrm{eV}$) and is nearly isotropic. The electron halo has a higher energy ($\gtrsim 50\,\mathrm{eV}$) than the core and is nearly isotropic as well. Lastly, the electron strahl is an energetic and highly field-aligned electron population.

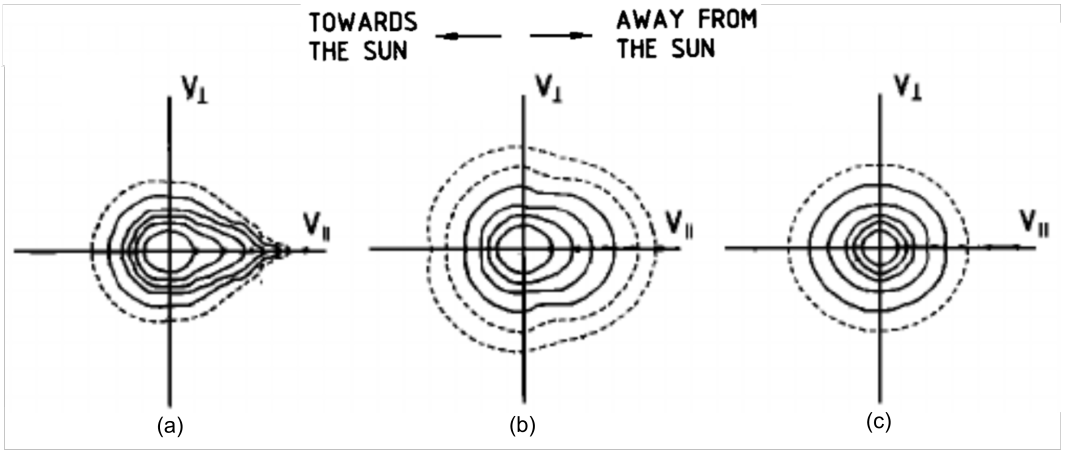

Figure 2.1: Electron VDFs measured by the Helios spacecraft at different distances from the Sun. (a) A highly anisotropic electron VDF measured at a distance of 0.3 au from the Sun shows a prominent electron strahl. (b) A moderately anisotropic electron VDF measured at a distance of 0.7 au from the Sun in the fast solar wind shows the result of electron strahl scattering perpendicular to the background magnetic field. (c) A nearly isotropic electron VDF measured at a distance of 0.7 au from the Sun in the slow solar wind shows no electron strahl (Pilipp et al., 1987a).

Fig. 2.1 visualises the phase-space density contours of the electron VDF in the plane of velocity space measured at different heliocentric distances from the Sun. The horizontal and vertical axes are $v_{\parallel}$ and $v_{\perp}$, respectively. The reference frame in these electron VDFs is the proton rest frame, and the solid and dotted lines are contours of constant phase-space density. The anti-sunward direction in Fig. 2.1 is on the right-hand side. Fig. 2.1(a) is the electron VDF measured at a distance of 0.3 au from the Sun. This electron VDF is highly anisotropic and shows a prominent

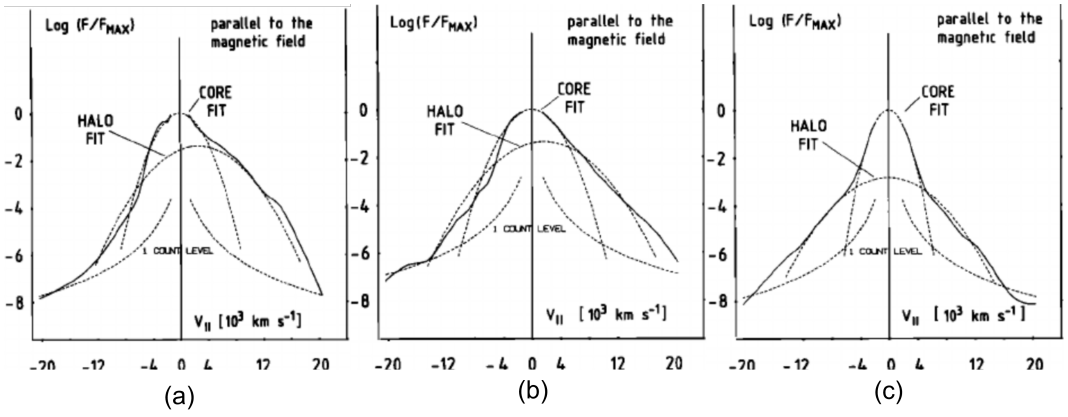

Figure 2.2: One dimensional cuts in the $v_{\|}$-direction of Fig. 2.1 at $v_{\perp} = 0$. (a), (b) and (c) correspond to Fig. 2.1(a), (b) and (c), respectively (Pilipp et al., 1987a).

electron strahl with a very narrow pitch angle at high parallel velocities in the anti-sunward direction. Fig. 2.1(b) is the electron VDF measured at a distance of 0.7 au from the Sun in the fast solar wind. It is moderately anisotropic and shows electron strahl which is diffused towards greater perpendicular velocities. Fig. 2.1(c) is an electron VDF measured at a distance of 0.7 au from the Sun in the slow solar wind. This electron VDF is nearly isotropic and shows that the electron strahl almost disappears.

Fig. 2.2 shows one-dimensional cuts in $v_{\|}$-space of Fig. 2.1 at $v_{\perp} = 0$. The vertical axis is the logarithm of the normalised electron VDF and the horizontal axis is $v_{\|}$. Fig. 2.2(a), (b) and (c) correspond to Fig. 2.1(a), (b) and (c), respectively. Fig. 2.2(a) shows a prominent shoulder of the electron VDF at anti-sunward $v_{\|}$, which is the field-aligned electron strahl. Fig. 2.2(b) shows a less pronounced electron strahl at anti-sunward velocity. In Fig. 2.2(c), the electron strahl nearly disappears. On the other hand, the electron halo population slightly increases and the halo bulk velocity is shifted toward the origin with increasing distance from the Sun. The core parallel VDF always remains quasi-isotropic, but its temperature decreases with distance judging by the contraction of the core parallel VDF.

Fig. 2.3 shows one dimensional cuts in $v_{\perp}$-space of Fig. 2.1 at $v_{\|} = 0$. The vertical axis is the logarithm of the normalised electron VDF and the horizontal axis is $v_{\perp}$. Fig. 2.3(a), (b) and (c) correspond to Fig. 2.1(a), (b) and (c), respec-

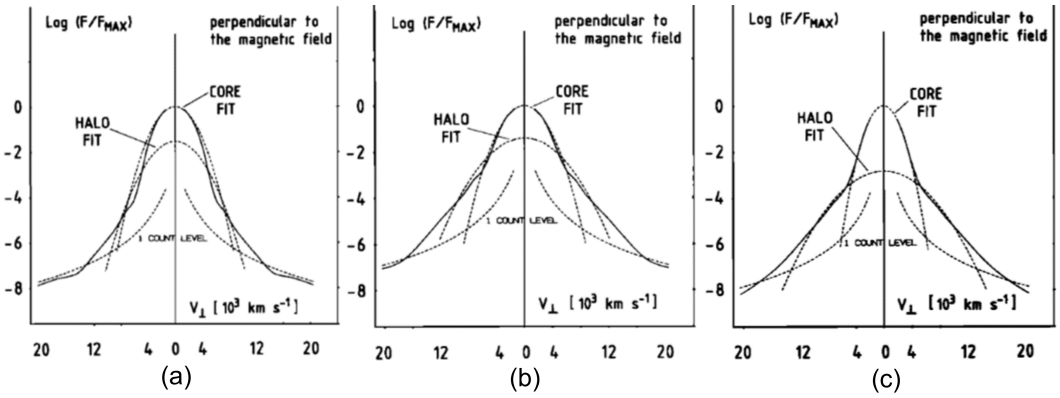

Figure 2.3: One dimensional cuts in the $v_\perp$-space of Fig. 2.1 at $v_\parallel = 0$. (a), (b) and (c) correspond to Fig. 1(a), (b) and (c), respectively (Pilipp et al., 1987a).

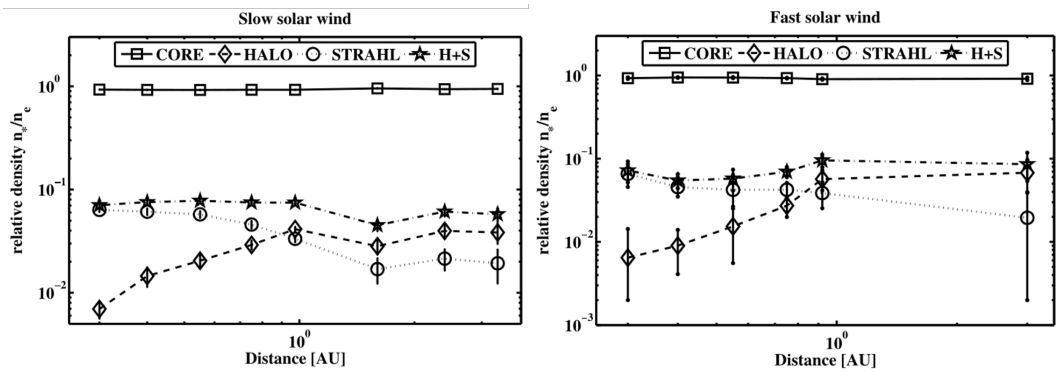

Figure 2.4: The densities of the electron core, halo and strahl, each divided by the local total number of electrons in slow and fast solar wind (Štverák et al., 2009).

tively. Fig. 2.3(a) shows a tenuous halo population at high $v_\perp$ at 0.3 au. However, Fig. 2.3(b) and (c) show an increase of the halo population with distance from the Sun. Like the core parallel VDF, the core perpendicular VDF remains largely symmetric, but its temperature decreases with heliocentric distance.

A statistical study based on data measured by Helios 1 and 2, Cluster and Ulysses shows the relative density evolution of each electron population with heliocentric distance in the fast and slow solar wind (Štverák et al., 2009). Fig. 2.4 shows the relative densities of each electron population in slow and fast solar winds, respectively. The relative density is defined as n_j/n_e where n_j is the local density of an electron population and n_e is the total local electron density. Both plots provide a similar pattern in the inner heliosphere. The relative density of the electron core remains approximately constant. On the other hand, the relative density of the elec-

tron strahl decreases while the relative density of the electron halo increases with distance from the Sun. However, the sum of the relative densities of the electron strahl and halo remains nearly constant in the inner heliosphere. This is evidence that these two electron populations are anti-correlated and that the electron strahl is transferred into the halo population.

In-situ measurements of the electron VDF suggest that the electron strahl is formed near the Sun, carrying most of the heat flux (Feldman et al., 1975; Pilipp et al., 1987b), and scattered into the halo population at large heliocentric distances. However, the strahl formation (Lie-Svendsen et al., 1997; Lie-Svendsen and Leer, 2000; Vocks and Mann, 2003; Owens et al., 2008; Smith et al., 2012; Landi et al., 2012; Seough et al., 2015; Tang et al., 2020) and strahl scattering (Horaites et al., 2018b, 2019; Boldyrev and Horaites, 2019; Vasko et al., 2019; Verscharen et al., 2019; López et al., 2020; Jeong et al., 2020; Micera et al., 2020, 2021; Halekas et al., 2021; Sun et al., 2021) mechanisms in the heliosphere are still unclear. These are two of the important questions that I will address in this thesis.

2.3 Radial Evolution of Solar-Wind Electrons

Because of the rotation of the Sun, the interplanetary magnetic field twists into the Parker-spiral with increasing distance from the Sun (Parker, 1958). The radial gradients in the plasma and field parameters (e.g., radial gradients of the solar-wind speed, temperature, and magnetic field) are greater at smaller heliocentric distances. Our PSP and Helios data confirm this behaviour (see Chapter 5). Since these gradients affect the shape of electron VDFs, the VDFs undergo a stronger modification in the near-Sun environment.

In the acceleration region of the solar wind (Bemporad, 2017; Yakovlev and Pisanko, 2018), the profile of the electron number density exhibits a steeper decrease than a $1/r^2$-profile. The anti-sunwardly propagating ballistic electrons are continuously supplied from the Sun. Ballistic particle streaming along the magnetic field causes the deposition of particle thermal energy of coronal origin into in the solar-wind electron VDF. The temperature gradient has a significant impact on

ballistic particle streaming along the magnetic field line. Because electrons have greater thermal velocities than protons, they leave the corona faster until a balance between the pressure gradient and the polarisation electric field sets in. The separation between protons and electrons creates a positive potential ϕ_E, leading to an ambipolar electric field:

$$E_{ambipolar} = -\nabla_{\mathbf{x}}\phi_E. \tag{2.1}$$

The electron temperature is proportional to $q_e\phi_E$ so that the ambipolar electric field is determined by the electron temperature gradient. The ambipolar electric field returns a large number of thermal core electrons back to the Sun (Boldyrev et al., 2020).

We assume that the local gradients of the interplanetary magnetic field are sufficiently small. This leads to the adiabatic invariance of the magnetic moment, given as

$$\mu = \frac{m_e v_\perp^2}{2B_0} = \text{const.} \tag{2.2}$$

Since μ and the electron's total kinetic energy are constant, the decreasing interplanetary magnetic field creates a magnetic mirror force which focuses outward-streaming electrons towards narrow pitch-angles. However, the magnetic mirror force becomes ineffective at large heliocentric distances due to the weakened large-scale gradient of the magnetic field (Owens et al., 2008). Coulomb collisions also play an important role in a regulation of the electron heat flux (Spitzer and Härm, 1953; Salem et al., 2003; Bale et al., 2013), and are an important mechanism of pitch angle scattering for the electron strahl (Horaites et al., 2018b).

According to observations at larger heliocentric distances than 0.3 au, the electron strahl population becomes faint with increasing heliocentric distance (Pilipp et al., 1987a; Štverák et al., 2009). Observations in the solar wind suggest that the electron strahl exchanges energy with whistler waves, which ultimately leads to a scattering of the electron strahl into the halo population, consistent with the results shown in Fig. 2.4 (Pagel et al., 2007; Lacombe et al., 2014; Graham et al., 2017). In addition, whistler waves can also enhance the electron strahl in the corona (Vocks

and Mann, 2003). These wave–particle interactions are important for the evolution of the electron VDF from the corona to 1 au and beyond.

Linear theory suggests that the fast-magnetosonic/whistler wave propagating obliquely with respect to the background magnetic field scatters the electron strahl through the $n = +1$ cyclotron resonance under typical solar-wind conditions (Vasko et al., 2019; Verscharen et al., 2019). This strahl-driven instability has recently received significant attention as a local strahl scattering mechanism, and has been confirmed by linear and quasi-linear theories and particle-in-cell (PIC) simulations (López et al., 2020; Jeong et al., 2020; Micera et al., 2020, 2021; Sun et al., 2021).

The electron VDF experiences the described global and local kinetic phenomena when it expands into interplanetary space. This thesis aims to study the effects of these global and local kinetic processes on the electron VDF in the following chapters. This thesis also shows the evidence that the description of the action of the fast-magnetosonic/whistler instability is still incomplete, because observations show that the strahl is most of the time far below the instability thresholds. Additional kinetic phenomena such as magnetic reconnection (Mann, G. et al., 2009), turbulence (Ryu et al., 2007; Yoon et al., 2012), shocks (Feldman et al., 1983; Fitzenreiter et al., 2003) and plasma mixing (Borovsky, 2012) are not considered in this thesis.

Chapter 3

A Quasi-Linear Diffusion Model for Resonant Wave-Particle Instability in Homogeneous Plasma

In this chapter, by analysing the quasi-linear diffusion equation, we propose a novel quasi-linear diffusion model for the time evolution of VDFs under the action of a dominant wave–particle instability. This quasi-linear framework confirms that an instability of the fast-magnetosonic/whistler wave in oblique propagation with respect to the background magnetic field is able to scatter the electron strahl into the electron halo. This chapter is based on the published paper "A Quasi-linear Diffusion Model for Resonant Wave–Particle Instability in Homogeneous Plasma", Jeong et al. (2020).

3.1 Introduction

Wave-particle interactions play an important role for the energy exchange between particles and waves in many space and astrophysical plasmas. For example, wave-particle interactions contribute to the acceleration and deceleration of particles in radiation belts (Ukhorskiy and Sitnov, 2014), the deviation of the particle VDF from a Maxwellian equilibrium in the solar wind (Marsch, 2006), the thermodynamic state of the intracluster medium in galaxy clusters (Roberg-Clark et al., 2016), and the scattering and absorption of the surface radiation in neutron-star magnetospheres

(Lyutikov and Gavriil, 2006). Therefore, it is of great importance to study the mechanics of wave-particle interactions in order to advance our understanding of the physics of astrophysical plasmas throughout the universe.

According to kinetic theory, wave-particle interactions can occur in the form of Landau or cyclotron resonances, which contribute to wave instability or wave damping depending on the resonance's characteristics. The quasi-linear theory of magnetized plasma, first established by Yakimenko (1963) and Kennel and Engelmann (1966), provides a mathematical framework to predict the evolution of the particle VDF under the action of the wave-particle interactions. The quasi-linear theory assumes that the spatially averaged VDF evolves slowly compared to the gyroperiod of the particles and the wave period. It furthermore assumes that the fluctuation amplitude is small and that the spatial average of the fluctuations vanishes. Based on this theory, numerous analytical studies have successfully explained the evolution of VDFs resulting from wave-particle interactions.

Resonant particles diffuse along specific trajectories in velocity space determined by the properties of the resonant wave (Kennel and Engelmann, 1966; Gendrin, 1968; Gendrin and Roux, 1980; Gendrin, 1981; Stix, 1992; Isenberg and Lee, 1996; Summers et al., 1998, 2001). Quasi-linear diffusion coefficients determine the diffusion rate of the resonant particles (Lyons et al., 1971; Lyons, 1974; Albert, 2004; Summers, 2005; Glauert and Horne, 2005; Isenberg and Vasquez, 2011; Tang et al., 2020). Alternatively, quasi-linear diffusion models based on a bi-Maxwellian VDF, in which only its moments evolve in time, describe the effective evolution of particle VDFs under the action of micro-instabilities (Yoon and Seough, 2012; Seough and Yoon, 2012; Yoon et al., 2015; Yoon, 2017; Yoon et al., 2017). Moreover, fully non-linear simulations based on kinetic theory model the evolution of the particle VDF consistently with predictions from quasi-linear theory (Vocks and Mann, 2003; Vocks et al., 2005; Gary et al., 2008; Saito et al., 2008, 2010; Saito and Peter Gary, 2012; Micera et al., 2020, 2021). The observation from Helios confirms the validity of basic concepts of ion cyclotron resonances predicted by quasi-linear theory (Marsch and Tu, 2001; Tu and Marsch, 2002; Heuer and Marsch, 2007;

Marsch and Bourouaine, 2011).

Realistic analytical models must describe the diffusive trajectory of the resonant particles in velocity space, taking into account the localized (in wavevector space) energy density of the resonant waves. These models must also account for non-Maxwellian features in the VDF evolution in order to advance our understanding of plasma observations and kinetic simulation results. A rigorous numerical analysis of the diffusion equation, including both the diagonal and off-diagonal diffusion terms, is necessary to support the theoretical description through the quantification of the diffusion rates.

In section 3.2, by analysing the quasi-linear diffusion equation, we develop a novel quasi-linear diffusion model for the time evolution of VDFs under the action of a dominant wave-particle instability and counter-acting damping contributions. Our model describes the creation and evolution of non-Maxwellian features in the particle VDF. We allow for an arbitrary type of the unstable and resonant wave mode with an arbitrary direction of propagation with respect to the background magnetic field. In our analysis, we express the electric field of this wave as a Gaussian wave packet in configuration space. The localisation of such a wave packet in configuration space is the direct consequence of its generation through a linear instability, which is localised in wavevector space.

To investigate the stabilisation of the VDF through quasi-linear diffusion, we apply our analysis of the quasi-linear diffusion equation to Boltzmann's H-theorem. In this scheme, the localised energy density of the Gaussian wave packet in wavevector space defines the velocity-space range in which the dominant wave-particle instability and counter-acting damping contributions are effective. In addition, we derive a relation to describe the diffusive trajectories of resonant particles in velocity space under the action of such an instability and damping. In this way, our model accounts for the diffusive behavior of resonant particles in different regions of velocity space. For the numerical evaluation of our theoretical description, we numerically solve the full quasi-linear diffusion equation based on the Crank–Nicolson scheme (for numerical details, see section 6.2).

In section 3.3, as an example, we apply our model to the scattering of the electron strahl. Our quasi-linear framework confirms that the oblique fast-magnetosonic/whistler (FM/W) instability scatters the electron strahl into the electron halo, as predicted by linear theory (Vasko et al., 2019; Verscharen et al., 2019). In section 3.4, for a more realistic model of the strahl evolution after the collisionless action of the oblique FM/W instability, we numerically solve the full Fokker-Planck equation for Coulomb collisions based on the Crank–Nicolson scheme (for numerical details, see section 6.3). We model the time evolution of the electron-strahl VDF through the action of Coulomb collisions with core electrons and protons. This combined method allows us to compare the timescales for the strahl scattering and collisional relaxation. In section 3.5, we discuss the results of our model for the strahl scattering and electron-halo formation through the instability and Coulomb collisions.

3.2 Quasi-Linear Diffusion Model

In this chapter, we establish our general theoretical framework for the description of a resonant wave-particle instability in quasi-linear theory. To investigate the time evolution of the particle VDF through wave-particle interactions, we study the quasi-linear diffusion equation, Eq. (1.44). We choose the coordinate system in which the proton bulk velocity is zero.

3.2.1 Analysis of Quasi-Linear Diffusion Equation

Linear instabilities typically create fluctuations across a finite range of wavevectors. The Fourier transformation of such a wave packet in wavevector space corresponds to a wave packet in configuration space. For the sake of simplicity, we model this finite wave packet by assuming that the electric field $\mathbf{E_r}$ of the unstable and resonant waves has the shape of a gyrotropic Gaussian wave packet

$$\mathbf{E_r} = \mathbf{E}_p \exp\left[-\frac{\sigma_{\perp 0}^2 x^2 + \sigma_{\perp 0}^2 y^2 + \sigma_{\parallel 0}^2 z^2}{2}\right] \exp\left[i\mathbf{k}_0 \cdot \mathbf{x}\right], \tag{3.1}$$

where $\mathbf{E}_p = \hat{x}E_p^x + \hat{y}E_p^y + \hat{z}E_p^z$, $\mathbf{k}_0 \cdot \mathbf{x} = k_{\perp 0} x \cos\phi + k_{\perp 0} y \sin\phi + k_{\parallel 0} z$, and $\mathbf{k}_0$ is the wavevector of the Gaussian wave packet. We allow for an arbitrary angle θ_0 between $\mathbf{k}_0$ and $\mathbf{B}_0$, which defines the orientation of the wavevector at maximum growth of the wave, and assume that $k_{\parallel 0} \neq 0$. The vector $\mathbf{E}_p$ represents the peak amplitude of the wave electric field. The free parameters $\sigma_{\perp 0}$ and $\sigma_{\parallel 0}$ characterize the width of the Gaussian envelope. Quasi-linear theory requires that $\mathbf{E_r}$ spatially averages to zero. Therefore, we assume that $|k_{\parallel 0}| \gg \sigma_{\parallel 0}$ so that the spatial dimension of the Gaussian wave packet is large compared to the parallel wave length $2\pi/|k_{\parallel 0}|$.

The spatial Fourier transformation of Eq. (3.1) according to Eq. (1.29) then leads to

$$\tilde{\mathbf{E}}_\mathbf{r} = \frac{\mathbf{E}_p}{\sigma_{\parallel 0}\sigma_{\perp 0}^2} \exp\left[-\frac{(k_\parallel - k_{\parallel 0})^2}{2\sigma_{\parallel 0}^2} - \frac{(k_\perp - k_{\perp 0})^2}{2\sigma_{\perp 0}^2} \right]. \tag{3.2}$$

We identify V with the volume of the Gaussian envelope, $V = 1/(\sigma_{\parallel 0}\sigma_{\perp 0}^2)$. Eq. (3.2) represents the localisation of the wave energy density in wavevector space. For the instability analysis through Eq. (3.2), we define the unstable **k**-spectrum as the finite wavevector range in which $\gamma_k > 0$ and argue that resonant waves exist only in this unstable **k**-spectrum. We neglect any waves outside this **k**-spectrum since they are damped.

We define $k_{\parallel 0}$ as the value of $k_\parallel$ at the centre of the unstable **k**-spectrum. We then obtain

$$k_{\perp 0} = k_{\parallel 0} \tan\theta_0. \tag{3.3}$$

In the case of a linear plasma instability, we identify $k_{\perp 0}$ and $k_{\parallel 0}$ with the wavevector components at which the instability has its maximum growth rate as a reasonable approximation. To approximate the wave frequency of the unstable waves at the angle θ_0 of maximum growth, we expand ω_k of the unstable and resonant waves around $k_{\parallel 0}$ as

$$\omega_k(k_\parallel) \approx \omega_{k0} + v_{g0}\left(k_\parallel - k_{\parallel 0}\right), \tag{3.4}$$

where

$$v_{g0} \equiv \left.\frac{\partial \omega_k}{\partial k_\parallel}\right|_{k_\parallel = k_{\parallel 0}}. \tag{3.5}$$

In Eqs. (3.4) and (3.5), ω_{k0} and v_{g0} are the wave frequency and parallel group velocity of the unstable and resonant waves, evaluated at $k_\parallel = k_{\parallel 0}$. We select the values of $\sigma_{\perp 0}$ and $\sigma_{\parallel 0}$ as the half widths of the perpendicular and parallel unstable **k**-spectrum. In the case of a linear plasma instability, the numerical values for $k_{\perp 0}$, $k_{\parallel 0}$, $\sigma_{\perp 0}$, $\sigma_{\parallel 0}$, ω_{k0} and v_{g0} can be found from the solutions of the hot-plasma dispersion relation, which thus closes our set of equations.

By using Eq. (3.2) and Eq. (3.4), we rewrite Eq. (1.44) as

$$\left(\frac{\partial f_j}{\partial t}\right)_{QLD} = \sum_{n=-\infty}^{\infty} \int \hat{G}[k_\parallel]\left[D_j^n \hat{G}[k_\parallel] f_j\right] d^3\mathbf{k}, \tag{3.6}$$

where

$$D_j^n \equiv \frac{\pi q_j^2 v_\perp^2}{\sigma_{\parallel 0}\sigma_{\perp 0}^2 m_j^2}\delta(k_\parallel - k_{\parallel j}^n)\frac{|\psi_{j0}^n|^2}{|v_\parallel - v_{g0}|}\exp\left[-\frac{(k_\parallel - k_{\parallel 0})^2}{\sigma_{\parallel 0}^2} - \frac{(k_\perp - k_{\perp 0})^2}{\sigma_{\perp 0}^2}\right], \tag{3.7}$$

$$\psi_{j0}^n \equiv \frac{1}{\sqrt{2}}\left[E_p^R e^{i\phi} J_{n+1}(\beta_j) + E_p^L e^{-i\phi} J_{n-1}(\beta_j)\right] + \frac{v_\parallel}{v_\perp} E_p^z J_n(\beta_j), \tag{3.8}$$

and

$$k_{\parallel j}^n \equiv \frac{\omega_{k0} - k_{\parallel 0} v_{g0} - n\Omega_j}{v_\parallel - v_{g0}}. \tag{3.9}$$

We note that $E_p^R = (E_p^x - iE_p^y)/\sqrt{2}$ and $E_p^L = (E_p^x + iE_p^y)/\sqrt{2}$ are constant, evaluated at $\mathbf{k}_0$.

Eq. (3.6) is the quasi-linear diffusion equation describing the action of the dominant wave-particle instability and co-existing damping contributions from other resonances in a Gaussian wave packet. We define the n resonance as the contribution to the summation in Eq. (3.6) with only integer n. We note that any n resonance can contribute to wave instability or to wave damping depending on the resonance's characteristics.

3.2.2 Stabilisation through a Resonant Wave-Particle Instability

We define the stabilisation as the process that creates the condition in which $(\partial f_j/\partial t)_{QLD} \to 0$ for all $v_\perp$ and $v_\parallel$. For our analysis of the stabilisation of a VDF through a resonant wave-particle instability, including co-existing damping effects, we use Boltzmann's H-theorem, in which the quantity H is defined as

$$H(t) \equiv \int f_j(\mathbf{v},t) \ln f_j(\mathbf{v},t) d^3\mathbf{v}. \tag{3.10}$$

By using Eq. (3.6), the time derivative of H is given by

$$\frac{dH}{dt} = \sum_{n=-\infty}^{\infty} \int\int (\ln f_j + 1)\hat{G}[k_\parallel]\left[D_j^n \hat{G}[k_\parallel] f_j\right] d^3\mathbf{k} d^3\mathbf{v}. \tag{3.11}$$

The integrand in Eq. (3.11) is equivalent to

$$(\ln f_j + 1)\hat{G}[k_\parallel]\left[D_j^n \hat{G}[k_\parallel] f_j\right] = \hat{G}[k_\parallel]\left[D_j^n \hat{G}[k_\parallel](f_j \ln f_j)\right] - \frac{D_j^n \left[\hat{G}[k_\parallel] f_j\right]^2}{f_j}. \tag{3.12}$$

Upon substituting Eq. (3.12) into Eq. (3.11), the first term on the right-hand side in Eq. (3.12) disappears after the integration over $\mathbf{v}$. Then, by resolving the δ-function in D_j^n through the $k_\parallel$-integral, we obtain

$$\frac{dH}{dt} = -\sum_{n=-\infty}^{\infty} \left(\frac{dH}{dt}\right)^n, \tag{3.13}$$

where

$$\left(\frac{dH}{dt}\right)^n \equiv \int \left\{\widetilde{D}_j^n \left[\hat{G}[k_{\parallel j}^n] f_j\right]^2 / f_j\right\} d^3\mathbf{v}, \tag{3.14}$$

$$\widetilde{D}_j^n \equiv W_j^n \frac{\pi q_j^2 v_\perp^2}{\sigma_{\parallel 0}\sigma_{\perp 0}^2 m_j^2} \int_0^{2\pi}\int_0^\infty |\psi_{j0}^n|^2 \exp\left[-\frac{(k_\perp - k_{\perp 0})^2}{\sigma_{\perp 0}^2}\right] k_\perp dk_\perp d\phi, \tag{3.15}$$

$$W_j^n \equiv \frac{1}{|v_\parallel - v_{g0}|} \exp\left[-\frac{k_{\parallel 0}^2}{\sigma_{\parallel 0}^2}\left(\frac{v_\parallel - v_{\parallel res}^n}{v_\parallel - v_{g0}}\right)^2\right], \tag{3.16}$$

$$v_{\parallel res}^{n} \equiv \frac{\omega_{k0} - n\Omega_j}{k_{\parallel 0}}, \tag{3.17}$$

$$\hat{G}[k_{\parallel j}^{n}] \equiv \left[\frac{n\Omega_j}{\omega_{k0} - k_{\parallel 0} v_{g0} - n\Omega_j}\right] \frac{v_\parallel - v_{g0}}{v_{ph} v_\perp} \frac{\partial}{\partial v_\perp} + \frac{1}{v_{ph}} \frac{\partial}{\partial v_\parallel}, \tag{3.18}$$

and

$$v_{ph} \equiv \frac{\omega_k(k_{\parallel j}^{n})}{k_{\parallel j}^{n}} = \frac{(\omega_{k0} - k_{\parallel 0} v_{g0}) v_\parallel - n\Omega_j v_{g0}}{\omega_{k0} - k_{\parallel 0} v_{g0} - n\Omega_j}. \tag{3.19}$$

The function $\widetilde{D}_j^n$ in Eq. (3.15) plays the role of a diffusion coefficient for the n resonance. In $\widetilde{D}_j^n$, the $v_\parallel$-function W_j^n defined in Eq. (3.16) serves as a window function that determines the region in $v_\parallel$-space in which the quasi-linear diffusion through the n resonance is effective. The window function W_j^n is maximum at $v_{\parallel res}^n$ defined in Eq. (3.17), which is the parallel velocity of the particles that resonate with the waves at $k_\parallel = k_{\parallel 0}$ through the n resonance. Our window function W_j^n is linked to Dirac's δ-function in the limit

$$\lim_{v_{\parallel res}^n \to v_{g0}} W_j^n \approx \sqrt{\pi} \frac{\sigma_{\parallel 0}}{|k_{\parallel 0}|} \delta(v_\parallel - v_{g0}), \tag{3.20}$$

where $|k_{\parallel 0}| \gg \sigma_{\parallel 0}$. Due to this ordering between $|k_{\parallel 0}|$ and $\sigma_{\parallel 0}$, we assume that W_j^n restricts a finite region in $v_\parallel$-space and that the W_j^n for different resonances do not overlap with each other in $v_\parallel$-space.

Only particles distributed within W_j^n experience the n resonance and contribute to the quasi-linear diffusion which is ultimately responsible for the stabilisation. Since all terms in Eq. (3.14) are positive semi-definite, all resonances independently stabilise f_j through quasi-linear diffusion in the $v_\parallel$-range defined by their respective W_j^n, according to Eq. (3.13). Therefore, H decreases and dH/dt tends towards zero during the quasi-linear diffusion through all resonances while f_j is in the process of stabilisation. When f_j reaches a state of full stabilisation through all n resonances, the instability has saturated and its growth ends.

The $v_\parallel$-function $k_{\parallel j}^n$ defined in Eq. (3.9) is the resonant parallel wavenumber, where $k_{\parallel j}^n = k_{\parallel 0}$ at $v_\parallel = v_{\parallel res}^n$. It quantifies the $k_\parallel$-component of the unstable $\mathbf{k}$-spectrum in the $v_\parallel$-range defined by W_j^n. Eq. (3.19) defines the phase velocity at

$k^n_{\|j}$, which is only constant when $v_{g0} = \omega_{k0}/k_{\|0}$, in which case $v_{ph} = v_{g0}$ for all $v_\|$. We discuss the diffusion operator $\hat{G}[k^n_{\|j}]$ in Eq. (3.18) in the next section.

3.2.3 Nature of Quasi-Linear Diffusion in Velocity Space

Considering Eq. (3.13), unless the wave amplitude is zero, the condition for the achievement of stabilisation through the n resonance is

$$\hat{G}[k^n_{\|j}]\mathbb{F}^n_j(v_\perp, v_\|) = 0, \tag{3.21}$$

where $\mathbb{F}^n_j(v_\perp, v_\|)$ represents the stabilised VDF of population j through the n resonance. According to Eq. (3.21), $\hat{G}[k^n_{\|j}]$ is a directional derivative along the isocontour of $\mathbb{F}^n_j$ evaluated at a given velocity position. Considering the role of W^n_j, $\hat{G}[k^n_{\|j}]$ describes only the diffusion of resonant particles within W^n_j along the isocontour of $\mathbb{F}^n_j$. Consequently, the particles experiencing the n resonance diffuse toward the stable state so that $(dH/dt)^n \to 0$, while the isocontour of $\mathbb{F}^n_j$ describes the diffusive trajectory for the n resonance.

To find such that trajectory, we express an infinitesimal variation of $\mathbb{F}^n_j$ along its isocontour as

$$d\mathbb{F}^n_j = \frac{\partial \mathbb{F}^n_j}{\partial v_\perp} dv_\perp + \frac{\partial \mathbb{F}^n_j}{\partial v_\|} dv_\| = 0. \tag{3.22}$$

Eqs. (3.18) and (3.22) allow us to rewrite Eq. (3.21) as

$$v_\perp dv_\perp + \left[\frac{n\Omega_j}{n\Omega_j - \omega_{k0} + k_{\|0} v_{g0}}\right](v_\| - v_{g0}) dv_\| = 0. \tag{3.23}$$

By integrating Eq. (3.23), the diffusive trajectory for the n resonance is then defined by

$$v^2_\perp + \left[\frac{n\Omega_j}{n\Omega_j - \omega_{k0} + k_{\|0} v_{g0}}\right](v_\| - v_{g0})^2 = const. \tag{3.24}$$

Kennel and Engelmann (1966) treat the two limiting cases in which $v_{g0} = \omega_{k0}/k_{\|0}$ and $v_{g0} = 0$. Using their assumptions, our Eq. (3.24) is equivalent to their equation (4.8) if $v_{g0} = \omega_{k0}/k_{\|0}$, and our Eq. (3.24) is equivalent to their equation (4.11) if

$v_{g0} = 0$. Depending on the dispersion properties of the resonant waves, Eq. (3.24) is either an elliptic or a hyperbolic equation when $n \neq 0$. In the case of electron resonances, it is safe to assume that

$$\frac{n\Omega_j}{n\Omega_j - \omega_{k0} + k_{\|0} v_{g0}} \geq 0, \tag{3.25}$$

in Eq. (3.24) if $v_{g0} < (\omega_{k0} + n|\Omega_e|)/k_{\|0}$ for all positive n and $v_{g0} > (\omega_{k0} + n|\Omega_e|)/k_{\|0}$ for all negative n. However, in the case of proton resonances, resonant waves are more likely to violate Eq. (3.25) since $\Omega_p \ll |\Omega_e|$.

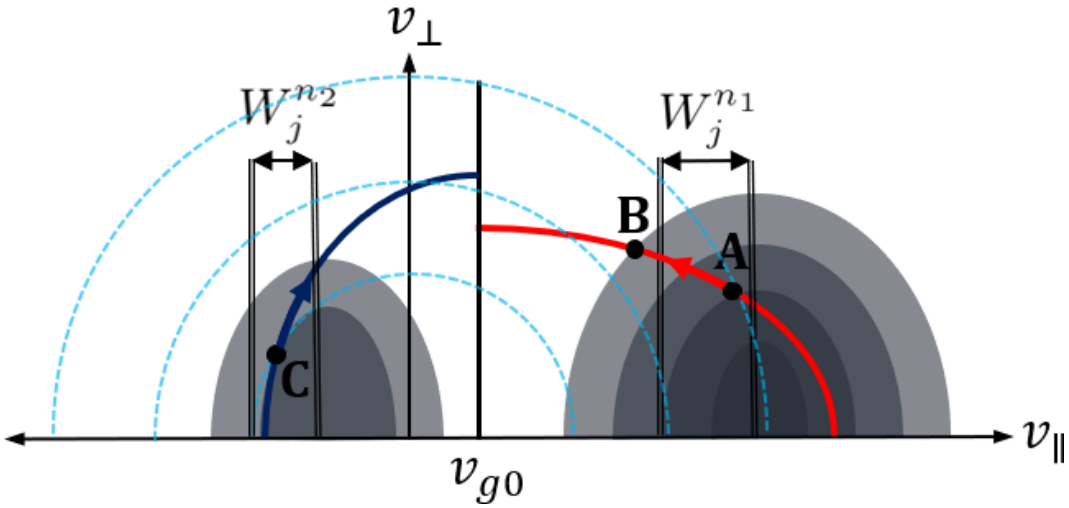

Figure 3.1: The diffusive flux of resonant particles in velocity space under the action of two arbitrary n_1 and n_2 resonances. The dark shaded areas represent isocontours of the VDFs of two particle populations. The red and dark-blue solid curves show the diffusive trajectories, Eq. (3.24) with $n = n_1$ and $n = n_2$. $W_j^{n_1}$ and $W_j^{n_2}$ represent the window functions according to Eq. (3.16), in which the n_1 and n_2 resonances are effective. The light-blue dashed semi-circles correspond to constant-energy contours. The black solid line indicates $v_\| = v_{g0}$.

Fig. 3.1 illustrates the diffusive flux of particles experiencing two arbitrary resonances: the n_1 and n_2 resonances for an unstable wave. The dark shaded areas represent isocontours of the VDFs of two particle populations in velocity space. The red and dark-blue solid curves represent the diffusive trajectories according to Eq. (3.24) with $n = n_1$ and $n = n_2$, assuming that the resonant wave fulfills Eq. (3.25). The window functions $W_j^{n_1}$ and $W_j^{n_2}$ describe the $v_\|$-ranges in which the n_1 and n_2 resonances are effective. The light-blue dashed semi-circles corre-

spond to contours of constant kinetic energy in the proton rest frame, for which

$$v_{\perp}^2 + v_{\parallel}^2 = const. \tag{3.26}$$

In general, the diffusive flux is always directed from higher to lower phase-space densities during the process of stabilisation. At point A, resonant particles in $W_j^{n_1}$ diffuse along the red solid curve towards smaller $v_{\parallel}$. Considering the relative alignment between the diffusive flux and constant-energy contour at point A, the diffusing particles lose kinetic energy. This energy is transferred to the resonant wave, which consequently grows in amplitude. Therefore, this situation corresponds to an instability of the resonant wave. At point B, particles do not diffuse along the red solid curve since this point lies outside $W_j^{n_1}$.

At point C, resonant particles in $W_j^{n_2}$ diffuse along the dark-blue solid curve towards greater $v_{\parallel}$. Considering the relative alignment between the diffusive flux and the constant-energy contour at point C, the diffusing particles gain kinetic energy. This energy is taken from the resonant wave, which consequently shrinks in amplitude. Therefore, this situation corresponds to damping of the resonant wave and counter-acts the driving of the instability through the n_1 resonance. Because the resonant wave is unstable, the n_1 resonant instability must overcome the counter-acting n_2 resonant damping.

According to Eq. (3.14), there are three factors that determine the diffusion rate for the action of an n resonance. The first factor is the particle density f_j within W_j^n. The second factor is $\widetilde{D}_j^n$ whose magnitude is determined by the polarisation properties of the resonant waves. The third factor is the quantity $\hat{G}[k_{\parallel j}^n]f_j/f_j$ which defines the relative alignment between the isocontours of f_i and the diffusive flux along the diffusive trajectory within W_j^n. In Fig. 3.1, the magnitude of $|\hat{G}[k_{\parallel j}^{n_1}]f_j/f_j|$ at point A is greater than the magnitude of $|\hat{G}[k_{\parallel j}^{n_2}]f_j/f_j|$ at point C.

Since the diffusive flux is directed from higher to lower values of f_j, the quantity $\hat{G}[k_{\parallel j}^n]f_j/f_j$ resolves the ambiguity in the directions of the trajectories for resonant particles. A careful analysis of $\hat{G}[k_{\parallel j}^n]$ with the fulfillment of Eq. (3.25) shows that, if $(k_{\parallel}/|k_{\parallel}|)(\hat{G}[k_{\parallel j}^n]f_j/f_j) > 0$ at a given resonant velocity, resonant par-

ticles diffuse toward a smaller value of $v_{\parallel}$ along the diffusive trajectory while, if $(k_{\parallel}/|k_{\parallel}|)(\hat{G}[k^n_{\parallel j}]f_j/f_j) < 0$ at a given resonant velocity, resonant particles diffuse toward a greater value of $v_{\parallel}$.

3.2.4 Numerical Analysis of the Quasi-Linear Diffusion Equation

To simulate the VDF evolution and to compare the diffusion rates between resonances quantitatively, a rigorous numerical analysis of Eq. (3.6) is necessary. For this purpose, we develop a mathematical approach based on the Crank-Nicolson scheme and present the mathematical details in section 6.2. Our numerical solution, given by Eq. (6.32), evolves the VDF under the action of multiple resonances in one time step. We tested our numerical solution by showing that the diffusive flux obeys the predicted diffusion properties discussed in section 3.2.3.

3.3 Fast-Magnetosonic/Whistler wave and Electron-Strahl Scattering

As an example, we apply our model developed in section 3.2 to an electron resonant instability in the solar wind. The fast-magnetosonic/whistler (FM/W) wave propagating in the anti-sunward direction and with an angle of $\sim 60^\circ$ with respect to the background magnetic field scatters the electron strahl (Vasko et al., 2019; Verscharen et al., 2019). Since this prediction is based on linear theory, our quasi-linear framework is appropriate for demonstrating the action of this instability on the electron strahl.

3.3.1 Linear Dispersion Relation

To find the characteristics of the unstable oblique FM/W wave, we numerically solve the hot-plasma dispersion relation with the NHDS code (Verscharen and Chandran, 2018). We use the same plasma parameters as Verscharen et al. (2019), which are, notwithstanding the wide range of natural variation, representative for the average electron parameters in the solar wind (Wilson et al., 2019). We assume that the initial plasma consists of isotropic Maxwellian protons, core electrons and

strahl electrons. The subscripts p, e, c and s indicate protons, electrons, electron core and electron strahl, respectively.

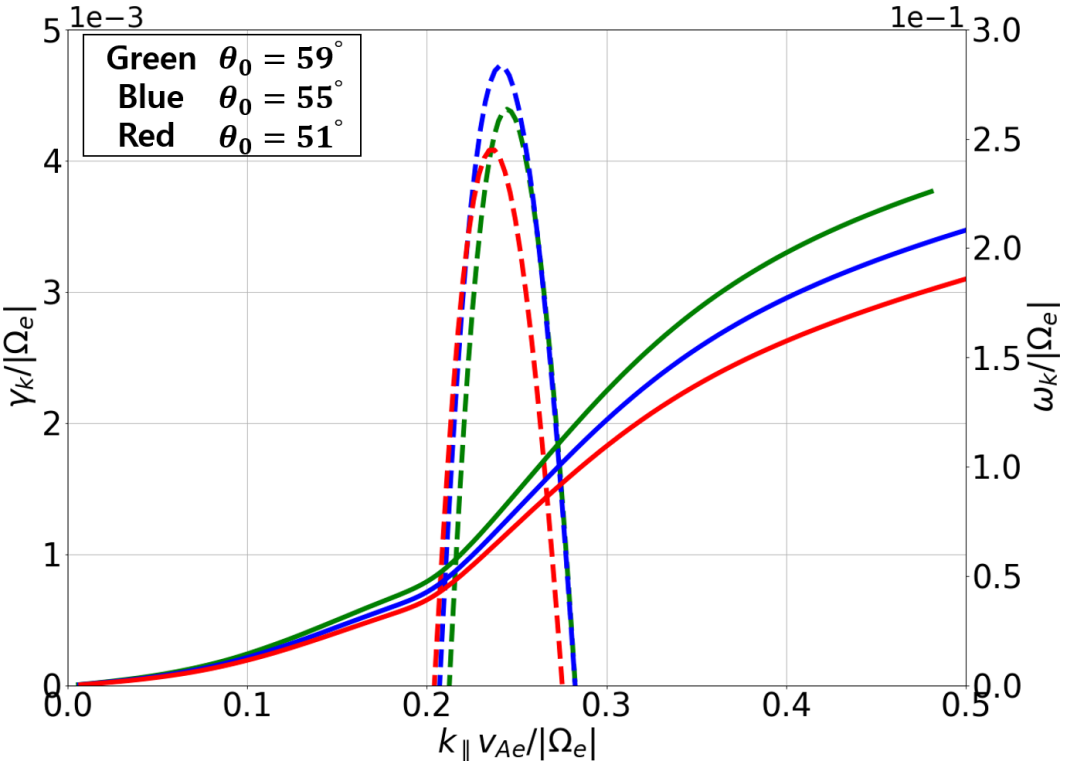

Figure 3.2: NHDS solutions provide γ_k (dashed curves, axis on the left) and ω_k (solid curves, axis on the right) as functions of the $k_\parallel$-component of the wavevector $\mathbf{k}$. We show solutions for $\theta_0 = 51°$, $\theta_0 = 55°$, and $\theta_0 = 59°$.

We choose our coordinate system so that the anti-sunward and obliquely propagating FM/W waves have $k_\parallel > 0$. We set $\beta_c = \beta_p = 1$ and $\beta_s = 0.174$, where $\beta_j \equiv (8\pi n_j k_B T_j)/B_0^2$. We set $n_p = n_e$, $n_c = 0.92 n_p$, $n_s = 0.08 n_p$, $T_c = T_p$, and $T_s = 2T_p$. In the proton rest frame, we set $n_c U_c + n_s U_s = 0$. We initialise the core and strahl bulk velocity with $U_c/v_{Ae} = -0.22$ and $U_s/v_{Ae} = 2.52$ where $v_{Ae} \equiv B_0/\sqrt{4\pi n_e m_e}$ is the electron Alfvén velocity. NHDS finds that, under these plasma parameters, $\gamma_k > 0$ at angles between $\theta_0 = 51°$ and $\theta_0 = 67°$. Our strahl bulk velocity then provides a maximum growth rate of $\gamma_k/|\Omega_e| = 10^{-3}$ (Verscharen et al., 2019).

Fig. 3.2 shows γ_k and ω_k as functions of the $k_\parallel$-component of the wavevector $\mathbf{k}$ for three different θ_0. The oblique FM/W instability has its maximum growth rate at $\theta_0 = 55°$, while $\gamma_k > 0$ for $0.21 \lesssim k_\parallel v_{Ae}/|\Omega_e| \lesssim 0.28$ which is the parallel unstable $\mathbf{k}$-spectrum. As defined in section 3.2.1, we acquire $k_{\parallel 0} v_{Ae}/|\Omega_e| \approx 0.245$.

This value with Eqs. (3.3)-(3.5) leads to $k_{\perp 0}v_{Ae}/|\Omega_e| = 0.35$, $\omega_{k0}/|\Omega_e| \approx 0.07$ and $v_{g0}/v_{Ae} \approx 0.86$. We also acquire $\sigma_{\parallel 0}v_{Ae}/|\Omega_e| \approx 0.035$ and $\sigma_{\perp 0}v_{Ae}/|\Omega_e| \approx 0.05$ from the obtained unstable **k**-spectrum.

3.3.2 Theoretical Description of the Quasi-Linear Diffusion in the FM/W Instability

Using the wave and plasma parameters from the previous chapter, we describe the electron strahl and core diffusion in velocity space. In our analysis, we only consider $n = +1$, -1 and 0 resonances, neglecting higher-n resonances due to their negligible contributions.

Upon substituting our wave parameters into Eq. (3.16), we quantify the dimensionless window functions $W_e^n v_{Ae}$ with $n = +1$, -1 and 0. In Fig. 3.3, the red, dark-blue and orange lines represent $W_e^{+1}v_{Ae}$, $W_e^{-1}v_{Ae}$ and $W_e^0 v_{Ae}$, which are maximum at $v_{\parallel res}^{+1}/v_{Ae} = 4.37$, $v_{\parallel res}^{-1}/v_{Ae} = -3.8$ and $v_{\parallel res}^{0}/v_{Ae} = 0.29$, respectively. We reiterate that the superscripts indicate the n resonance. The black line indicates $v_\parallel = v_{g0}$. Each $W_e^n v_{Ae}$ shows the $v_\parallel$-range in which the quasi-linear diffusion through each resonance is effective. We note that $W_e^n v_{Ae}$ for the three resonances have a different width in $v_\parallel$-space and maximum value due to a different magnitude of $|v_{\parallel res}^n - v_{g0}|$ (see Eq. (3.20)). By substituting our wave parameters into Eq. (3.24), the diffusive trajectories for the $n = +1$, -1 and 0 resonances are given by

$$(v_\perp/v_{Ae})^2 + 1.16\left(v_\parallel/v_{Ae} - 0.86\right)^2 = const, \tag{3.27}$$

$$(v_\perp/v_{Ae})^2 + 0.88\left(v_\parallel/v_{Ae} - 0.86\right)^2 = const, \tag{3.28}$$

and

$$(v_\perp/v_{Ae})^2 = const. \tag{3.29}$$

Eqs. (3.27) and (3.28) describe ellipses with their axes oriented along the $v_\perp$- and $v_\parallel$-directions. In Eq. (3.29), the perpendicular velocity of resonant particles is constant.

Fig. 3.4 illustrates the electron diffusion from these three resonances. We show the $v_\parallel$-ranges in which these three resonances are effective according to $W_e^{+1}v_{Ae}$,

$W_e^{-1} v_{Ae}$ and $W_e^{0} v_{Ae}$ from Fig. 3.3. The red, dark-blue and orange solid lines represent the contours given by Eqs. (3.27)-(3.29), respectively. The light-blue dashed semi-circles correspond to constant-energy contours in the proton rest frame (see Eq. (3.26)). The black line indicates $v_\parallel = v_{g0}$. For the initial strahl and core VDF, we apply the plasma parameters in section 3.3.1 to the dimensionless Maxwellian distribution

$$f_j^M = \frac{n_j v_{Ae}^3}{\pi^{3/2} n_p v_{th,j}^3} \exp\left[-\frac{v_\perp^2 + (v_\parallel - U_j)^2}{v_{th,j}^2} \right]. \tag{3.30}$$

The red and blue areas in Fig. 3.4 represent f_s^M and f_c^M which are normalised by the maximum value of f_c^M and plotted up to a value of 10^{-5}. In this normalisation, Fig. 3.4 does not reflect the relative density between both electron populations.

Due to the $v_\parallel$-profile of W_e^{+1}, the $n = +1$ resonance has a significant effect on f_s^M. As discussed in section 3.2.3, since $(k_\parallel/|k_\parallel|)(\hat{G}[k_{\parallel e}^{+1}] f_s^M / f_s^M) > 0$, this resonance leads to the diffusion of the resonant strahl electrons in W_e^{+1} along the red arrows. According to Eq. (3.26), the phase-space trajectory of particles that diffuse without a change in kinetic energy is described by

$$\left(\frac{dv_\perp}{dv_\parallel} \right)_E = -\frac{v_\parallel}{v_\perp}. \tag{3.31}$$

According to Eq. (3.27), the phase-space trajectory of resonant particles fulfilling the $n = +1$ resonance, indicated by superscript $+1$, is described by

$$\left(\frac{dv_\perp}{dv_\parallel} \right)^{+1} = -1.16 \frac{v_{Ae}}{v_\perp} \left(\frac{v_\parallel}{v_{Ae}} - 0.86 \right). \tag{3.32}$$

Evaluating Eqs. (3.31) and (3.32) in W_e^{+1} shows that $|(dv_\perp/dv_\parallel)^{+1}| < |(dv_\perp/dv_\parallel)_E|$ for the resonant electrons. Therefore, resolving the ambiguity in the directions of the trajectories, the distance of resonant strahl electrons from the origin of the coordinate system decreases. This decrease in $v_\perp^2 + v_\parallel^2$ represents a loss of kinetic energy of the resonant strahl electrons. The $n = +1$ resonance, therefore, contributes to the driving of the FM/W instability.

Due to the $v_\parallel$-profile of W_e^{-1}, the $n = -1$ resonance has a significant effect

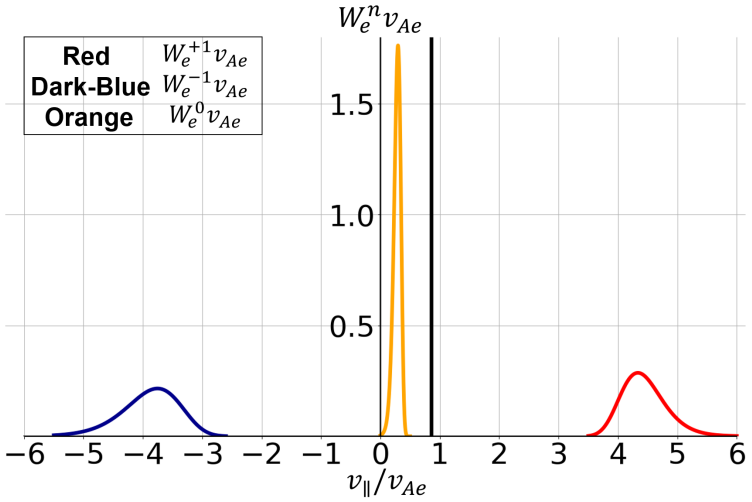

Figure 3.3: The red, dark-blue and orange plots illustrate $W_e^{+1} v_{Ae}$, $W_e^{-1} v_{Ae}$ and $W_e^0 v_{Ae}$ for the oblique FM/W wave. The black solid line represents $v_\parallel = v_{g0}$. Each $W_e^n v_{Ae}$ shows the $v_\parallel$-range in which each resonance is effective. Each $W_e^n v_{Ae}$ has a different width in $v_\parallel$-space and maximum value due to a different magnitude of $|v_{\parallel res}^n - v_{g0}|$ (see Eq. (3.20)).

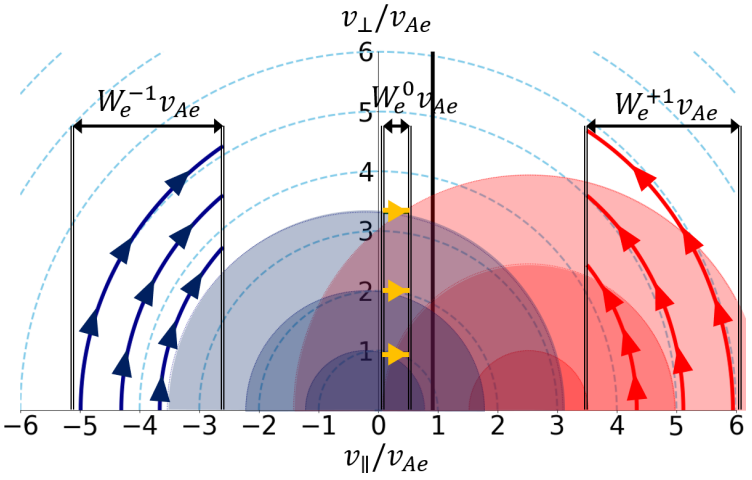

Figure 3.4: The red, dark-blue and orange arrows illustrate the diffusive flux according to the $n = +1, -1$ and 0 resonances for the oblique FM/W instability. The red and dark-blue filled semi-circles represent isocontours of the strahl and core VDF. This figure does not reflect the relative densities of both electron species. The light-blue dashed semi-circles correspond to constant-energy contours. The black solid line indicates $v_\parallel = v_{g0}$.

on f_c^M. Since $(k_\parallel/|k_\parallel|)(\hat{G}[k_{\parallel e}^{-1}]f_c^M/f_c^M) < 0$, this resonance leads to the diffusion of the resonant core electrons in W_e^{-1} along the dark-blue arrows. According to Eq. (3.28), the phase-space trajectory of resonant particles fulfilling the $n = -1$ resonance, indicated by superscript -1, is described by

$$\left(\frac{dv_\perp}{dv_\parallel}\right)^{-1} = -0.88\frac{v_{Ae}}{v_\perp}\left(\frac{v_\parallel}{v_{Ae}} - 0.86\right). \tag{3.33}$$

Evaluating Eqs. (3.31) and (3.33) in W_e^{-1} shows that $|(dv_\perp/dv_\parallel)^{-1}| > |(dv_\perp/dv_\parallel)_E|$ for the resonant electrons. Therefore, resolving the ambiguity in the directions of the trajectories, the distance of resonant core electrons from the origin of the coordinate system increases. This increase in $v_\perp^2 + v_\parallel^2$ represents a gain of kinetic energy of the resonant core electrons. The $n = -1$ resonance, therefore, counter-acts the FM/W instability through the $n = +1$ resonance.

Due to the $v_\parallel$-profile of W_e^0, the $n = 0$ resonance has a significant effect on electrons in the $v_\parallel$-range in which $f_c^M > f_s^M$ and $\partial f_c^M/\partial v_\parallel < 0$. Since $(k_\parallel/|k_\parallel|)(\hat{G}[k_{\parallel e}^0]f_c^M/f_c^M) < 0$, the resonant electrons in W_e^0 diffuse along the yellow arrows. Because the distance of these electrons from the origin of the coordinate system increases, these resonant electrons diffuse towards greater kinetic energies. This diffusion removes energy from the resonant FM/W waves and thus counter-acts the driving of the FM/W instability through the $n = +1$ resonance.

The illustration in Fig. 3.4 describes the nature of the quasi-linear diffusion through the $n = +1$, -1 and 0 resonances in velocity space. It does not give any information regarding the relative strengths of the diffusion rates between the three resonances. Since the FM/W wave is unstable according to linear theory, the $n = +1$ resonant instability must dominate over any counter-acting contributions from the $n = -1$ and 0 resonances.

3.3.3 Numerical Description of the Quasi-Linear Diffusion in the FM/W Instability

We use our numerical analysis in section 6.2 to simulate the quasi-linear diffusion through the $n = +1$, -1 and 0 resonances, predicted in section 3.3.2. According to the definitions in section 6.2, we select the discretisation parameters $N_v = 45$, $v_{\perp\max}/v_{Ae} = v_{\parallel\max}/v_{Ae} = 7$ and $|\Omega_e|\Delta t = 1$. For the computation of Eq. (6.32), we use the parameters of resonant FM/W waves presented in section 3.3.1 and quantify $\widetilde{D}_e^{\pm 1}$ and $\widetilde{D}_e^{0}$ in Eq. (3.15).

In $\widetilde{D}_e^n$ for each resonance, we only consider the J_0 term in ψ_{j0}^n, neglecting higher-order Bessel functions due to their small contributions. Our NHDS solutions show that $|E_p^y| \approx 0.2|E_p^x|$ and $|E_p^z| \approx 0.14|E_p^x|$ in the unstable $\mathbf{k}$-spectrum. Then, we set $|E_p^R| \approx |E_p^L| \approx 0.72|E_p^x|$. Faraday's law yields $E_p^x \approx [\omega_{k0}/(k_{\parallel 0}c)]B_p^y$ when neglecting the small contributions from E_p^z terms. This allows us to express E_p^x through B_p^y in ψ_{j0}^n, where B_p^y represents the peak amplitude of the wave magnetic-field fluctuations. For simplicity, we assume that B_p^y is constant in time during the quasi-linear diffusion. Under these assumptions, we acquire

$$\widetilde{D}_e^{\pm 1} \approx W_e^{\pm 1} \frac{0.52\pi^2|\Omega_e|^2 v_\perp^2}{\sigma_{\parallel 0}\sigma_{\perp 0}^2} \left[\frac{B_p^y}{B_0}\frac{\omega_{k0}}{k_{\parallel 0}}\right]^2 \times \int_0^\infty J_0(\beta_e)^2 \exp\left[-\frac{(k_\perp - k_{\perp 0})^2}{\sigma_{\perp 0}^2}\right] k_\perp dk_\perp, \tag{3.34}$$

and

$$\widetilde{D}_e^{0} \approx W_e^{0} \frac{0.04\pi^2|\Omega_e|^2 v_\parallel^2}{\sigma_{\parallel 0}\sigma_{\perp 0}^2} \left[\frac{B_p^y}{B_0}\frac{\omega_{k0}}{k_{\parallel 0}}\right]^2 \times \int_0^\infty J_0(\beta_e)^2 \exp\left[-\frac{(k_\perp - k_{\perp 0})^2}{\sigma_{\perp 0}^2}\right] k_\perp dk_\perp, \tag{3.35}$$

where the relative amplitude B_p^y/B_0 is a free parameter and we set $B_p^y/B_0 = 0.001$. Then, we apply Eqs. (3.34) and (3.35) to Eq. (6.32).

We initialise our numerical computation with the same f_s^M and f_c^M as defined in

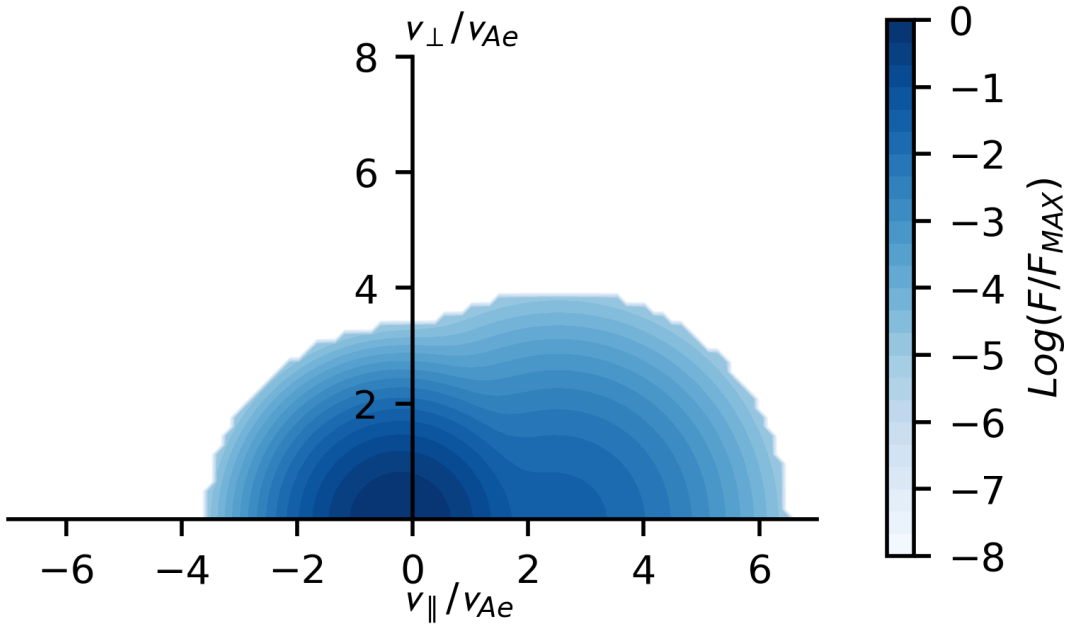

(a) $|\Omega_e|t = 0$

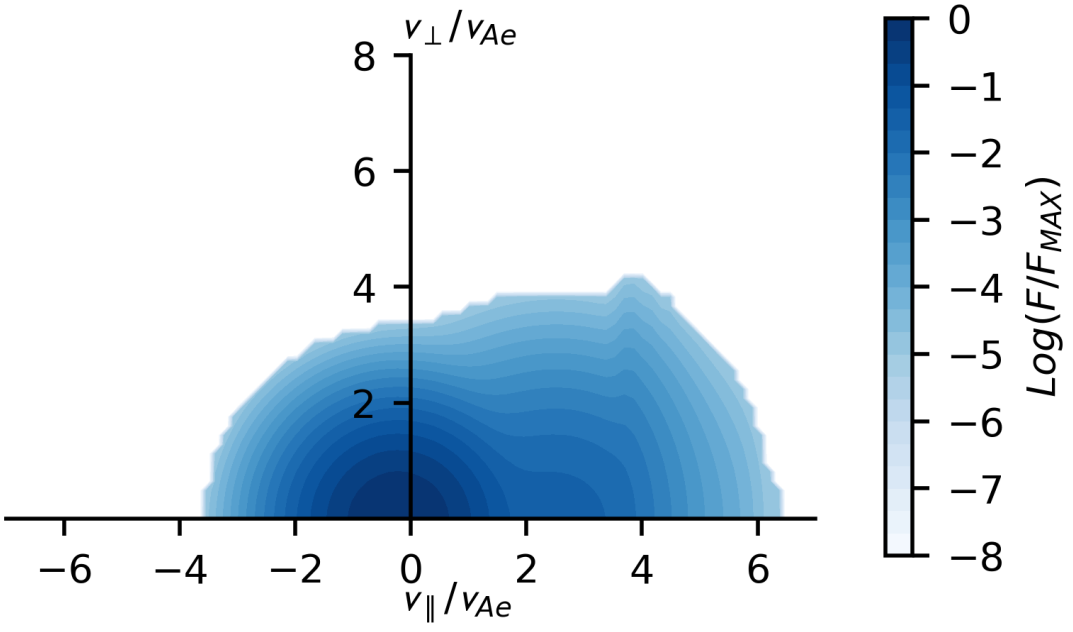

(b) $|\Omega_e|t = 5 \times 10^2$

Figure 3.5: Fig. 3.5a: the initial electron VDF; Fig. 3.5b: the electron VDF evolved through the $n = +1$, -1 and 0 resonances. Compared to Fig. 3.4, only the effect of the $n = +1$ resonance is noticeable during the time $\gamma_k t \sim 1$. It causes a significant pitch-angle gradient at $v_\parallel / v_{Ae} \approx 3.8$ through the scattering of strahl electrons. The figure shows the time evolution of the distribution function from $|\Omega_e|t = 0$ to $|\Omega_e|t = 5 \times 10^2$. During this evolution, the strahl scattering towards larger $v_\perp$ is visible.

section 3.3.2. Fig. 3.5a represents $f_e = f_c^M + f_s^M$, normalised by the maximum value of f_c^M and plotted up to a value of 10^{-5}. Fig. 3.5b shows f_e evolved through the $n = +1$, -1 and 0 resonances, resulting from the iterative calculation of Eq. (6.32). Considering the maximum value of the instability's growth rate, $\gamma_k/|\Omega_e| = 4.8 \times 10^{-3}$ in Fig. 3.2, we finish the evaluation of our numerical computation at $|\Omega_e|t = 5 \times 10^2$ which corresponds to $\gamma_k t \sim 1$ and thus a reasonable total growth of the unstable FM/W waves.

The strahl electrons at around $v_\parallel/v_{Ae} \approx 4.4$ diffuse through the $n = +1$ resonance, as theoretically predicted in Fig. 3.4. This diffusion increases the pitch-angle of the resonant strahl electrons and generates a strong pitch-angle gradient at $v_\parallel/v_{Ae} \approx 3.8$. During this process, the $v_\perp$ of the scattered strahl electrons increases while their $v_\parallel$ decreases.

Since the longitudinal component of the electric-field fluctuations is much weaker than their transverse components, the diffusion through the $n = 0$ resonance is not noticeable over the modeled time interval. The diffusion through the $n = -1$ resonance is not noticeable even though $\widetilde{D}_e^{-1}$ and $\widetilde{D}_e^{+1}$ have a similar magnitude. This is because the magnitude of $|\hat{G}[k_{\parallel e}^{-1}] f_e/f_e|$ in W_e^{-1} is much smaller than the magnitude of $|\hat{G}[k_{\parallel e}^{+1}] f_e/f_e|$ in W_e^{+1}, as discussed in section 3.2.3, and the number of core electrons in W_e^{-1} is very small (see Fig. 3.4 and 3.5).

3.4 The Secondary Effect of Coulomb Collisions

Since the collisionless action of resonant wave-particle instabilities often form strong pitch-angle gradients (see, for example, Fig. 3.5), the collisions can be enhanced in the plasma. Therefore, a more realistic evolution of the total electron VDF must account for the action of Coulomb collisions of strahl electrons with core electrons and protons. For this purpose, we adopt the Fokker-Planck operator given by Ljepojevic et al. (1990) with Rosenbluth potentials (Rosenbluth et al., 1957). In Appendix A, we provide the great detail analysis for the Fokker-Planck operator. We use the Fokker-Planck operator, Eq. (A.44), normalised with the dimensionless

unit system of this chapter as

$$\left(\frac{\partial f_s}{\partial t}\right)_{\rm col} = \sum_b \Gamma_{eb}\left(4\pi\frac{m_e}{m_b}f_b f_s + \frac{\partial H_b}{\partial v_\perp}\frac{\partial f_s}{\partial v_\perp} + \frac{\partial H_b}{\partial v_\parallel}\frac{\partial f_s}{\partial v_\parallel} + \frac{1}{2v_\perp^2}\frac{\partial G_b}{\partial v_\perp}\frac{\partial f_e}{\partial v_\perp} + \frac{1}{2}\frac{\partial^2 G_b}{\partial v_\perp^2}\frac{\partial^2 f_s}{\partial v_\perp^2} + \frac{1}{2}\frac{\partial^2 G_b}{\partial v_\parallel^2}\frac{\partial^2 f_s}{\partial v_\parallel^2} + \frac{\partial^2 G_b}{\partial v_\perp \partial v_\parallel}\frac{\partial^2 f_s}{\partial v_\perp \partial v_\parallel}\right), \tag{3.36}$$

where

$$G_b(\mathbf{v}) \equiv \int f_b(\mathbf{v}')|\mathbf{v}-\mathbf{v}'|d^3\mathbf{v}', \tag{3.37}$$

$$H_b(\mathbf{v}) \equiv \frac{m_b - m_j}{m_b}\int f_b(\mathbf{v}')|\mathbf{v}-\mathbf{v}'|^{-1}d^3\mathbf{v}', \tag{3.38}$$

and

$$\Gamma_{eb} \equiv \frac{4\pi n_b}{v_{Ae}^3|\Omega_e|}\left(\frac{Z_b q_e^2}{m_e}\right)^2 \ln\Lambda_{eb}. \tag{3.39}$$

In Eq. (4.44), f_s is the electron-strahl VDF evolved by the oblique FM/W instability at time $|\Omega_e|t = 5\times10^2$ from our quasi-linear analysis. The subscript b indicates the species of background particles, with which the electron strahl Coulomb-collides. The quantity $\ln\Lambda_{eb}$ is the Coulomb logarithm and typically $\ln\Lambda_{eb}\approx 25$ in space plasmas. The parameter Z_b is the charge number of a particle of species b.

We assume that the timescale of Coulomb collisions is much longer than the timescale of the quasi-linear diffusion in the solar wind under our set of parameters. This assumption allows us to model the resonant wave-particle instability first and to use the resulting VDF as the input for the model of the subsequent, secondary effects of collisions. In this setup, our initial f_s for this Coulomb collision analysis is same as the electron VDF shown in Fig. 3.5b.

In section 6.3, we numerically solve Eq. (4.44), and we tested our numerical solutions, Eq. (6.49), by showing that a set of arbitrary test VDFs diffuses toward f_b with time. For the computation of Eq. (6.49), we set isotropic Maxwellian electron-core and proton VDFs as background populations, $f_b = f_c^M$ and $f_b = f_p^M$, for which we apply the plasma parameters presented in section 3.3.1 to Eq. (3.30). In this numerical computation, we select the discretisation parameters $N_v = 45$, $v_{\perp\max}/v_{Ae} = v_{\parallel\max}/v_{Ae} = 7$ and $|\Omega_e|\Delta t = 10$. Moreover, we set $B_0 = 5\times10^{-4}G$ and

$n_b = 10^2 cm^{-3}$ in Eq. (4.47), which are representative for the conditions in the solar wind at a distance of 0.3 au from the Sun. The iterative calculation of Eq. (6.49) results in the time evolution of the electron-strahl VDF under the action of Coulomb collisions with core electrons and protons. The result of this computation at the time $|\Omega_e|t = 7 \times 10^7$ is shown in Fig. 3.6.

A detailed comparison of the distribution function before (Fig. 3.6a) and after (Fig. 3.6b) our calculation of the effect of Coulomb collisions reveals that Coulomb collisions relax the strong pitch-angle gradient at $v_{\parallel}/v_{Ae} \approx 3.8$, which resulted from the action of the oblique FM/W instability. However, the Coulomb collisions are only capable of affecting strong pitch-angle gradients in the modified electron VDF under our plasma parameters. In addition, the required time for a noticeable collisional effect on this pitch-angle gradient is of order 10^5 times longer than the characteristic timescale of the quasi-linear diffusion.

3.5 Discussion

Wave–particle interactions are important plasma-physics processes in many astrophysical plasmas. Often, fully non-linear simulations with codes solving the equations of kinetic plasma theory are used to model the evolution of the particle VDF under the action of wave–particle interactions. However, quasi-linear theory augments this approach since it allows us to study the contributions of different processes to these interactions as a local physical mechanism. Therefore, quasi-linear theory is a very helpful tool to improve our understanding of wave–particle interactions in astrophysical plasmas beyond the direct numerical evaluation of the particles' equations of motion.

We provide a quasi-linear diffusion model for any generalised wave–particle instability, and apply this model to the oblique FM/W instability scattering the electron strahl. During the action of the oblique FM/W instability, the scattered strahl electrons reduce their collimation along the $\mathbf{B}_0$-direction and become more isotropic. Even though this instability does not cause significant strahl scattering, we argue that it contributes to the initial formation of the halo population. However,

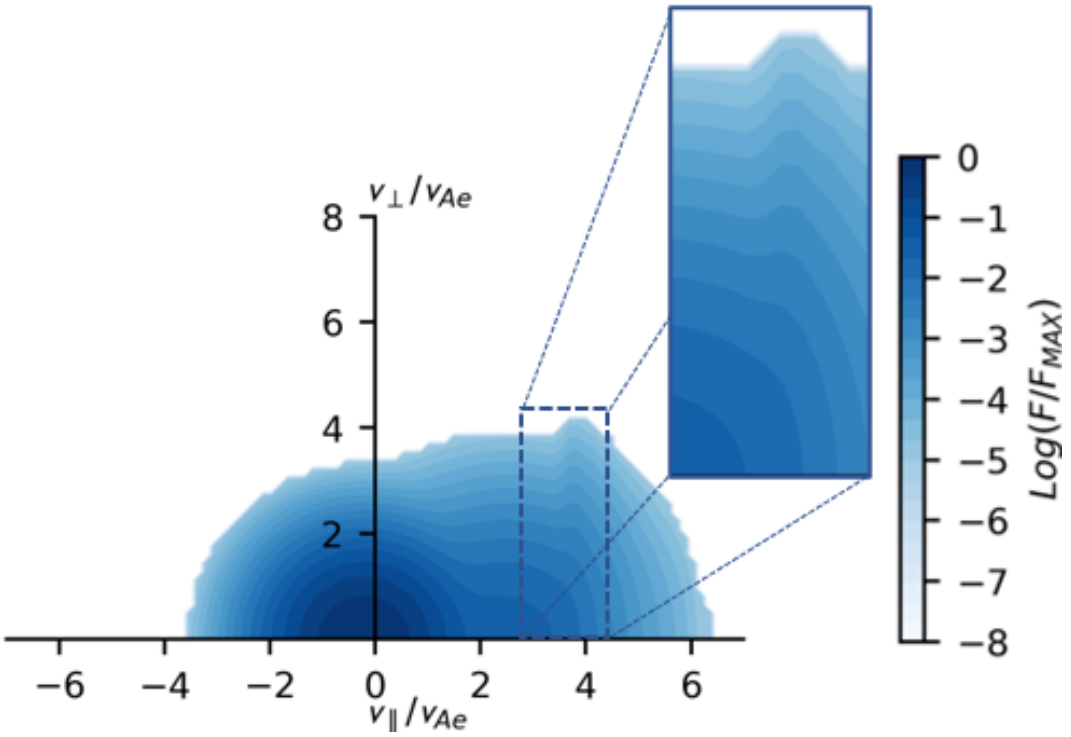

(a) $|\Omega_e|t = 5 \times 10^2$

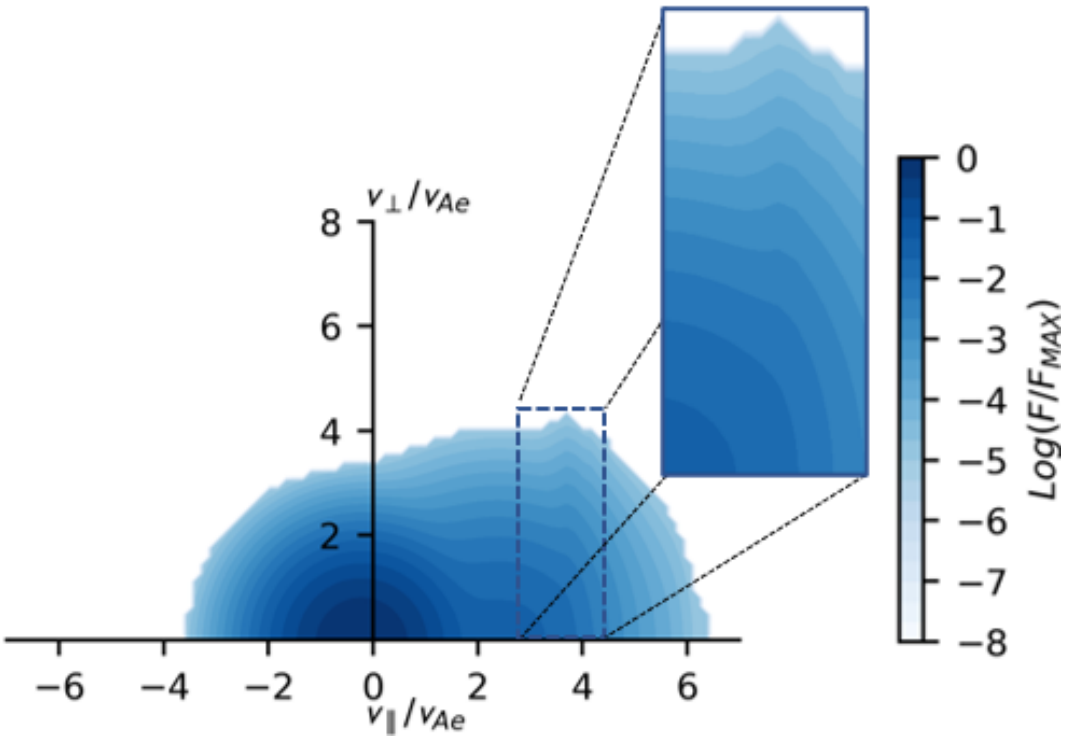

(b) $|\Omega_e|t = 7 \times 10^7$

Figure 3.6: Fig. 3.6a: the electron VDF as initial condition for our collision analysis; Fig. 3.6b: the electron VDF evolved through Coulomb collisions of strahl electrons with core electrons and protons. The strong pitch-angle gradient at $v_\parallel/v_{Ae} \approx 3.8$ (shown in Fig. 3.6a and Fig. 3.5b) is relaxed through the Coulomb collisions. However, the required time for a noticeable collisional effect on that gradient is around 10^5 times longer than the timescale of the strahl scattering. The figure shows the time evolution of the distribution function from $|\Omega_e|t = 5 \times 10^2$ to $|\Omega_e|t = 7 \times 10^7$. During this evolution, the collisional smoothing of the pitch-angle gradients is visible.

other mechanisms must be considered to account for the full strahl scattering in agreement with observations (Gurgiolo et al., 2012; Gurgiolo and Goldstein, 2016).

The numerical computation of Eq. (3.13) shows that dH/dt is negative and asymptotically tends towards zero as the electron VDF evolves through the oblique FM/W instability and the counter-acting damping effects until the time $|\Omega_e|t = 5 \times 10^2$, which is presented in Fig. 3.5. Therefore, our quasi-linear diffusion model reflects the stabilisation of the particle VDF through the participating wave-particle resonances.

We note that our analysis includes the subsequent action of Coulomb collisions after the action of collisionless wave-particle resonances assuming plasma parameters consistent with the solar wind at a distance of 0.3 au from the Sun. Our collisional effects are similar to those proposed by Vocks et al. (2005). However, our model predicts that the collisional relaxation is so subtle that the strahl scattering through collisions is barely noticeable for the analysed phase of the VDF evolution.

The clear separation of timescales between wave-particle effects and Coulomb-collisional effects complicates the description of the VDF evolution on heliospheric scales, since other processes act on comparable timescales. These additional processes, which our analysis neglects, include turbulence, shocks, plasma mixing, plasma expansion, and magnetic focusing (Yoon et al., 2012; Ryu et al., 2007; Feldman et al., 1983; Fitzenreiter et al., 2003; Tang et al., 2020). A complete model for the radial evolution of the VDF must quantify and account for these processes as well. In the context of our work, these processes can potentially push a VDF that has undergone stabilisation as shown in Fig. 3.5b into the unstable regime again. In this case, dH/dt in Eq. (3.13) returns to a non-zero value, which signifies a new onset of wave-particle resonances and further scattering of resonant particles.

Chapter 4

The Kinetic Expansion of Solar-Wind Electrons: Transport Theory and Predictions for the very Inner Heliosphere

In this chapter, we derive a gyro-averaged kinetic transport equation that accounts for the spherical expansion of the solar wind and the geometry of the Parker-spiral magnetic field. By using our kinetic transport equation, we propose a transport model for the kinetic evolution of solar-wind electrons in the very inner heliosphere. This chapter is based on the submitted paper "The Kinetic Expansion of Solar-Wind Electrons: Transport Theory and Predictions for the very Inner Heliosphere", Jeong et al. (2022b).

4.1 Introduction

The electron VDF in the expanding solar wind experiences global kinetic phenomena caused by the radial gradients in the plasma and field parameters. Previous theoretical models for the evolution of the electron VDF primarily account for the global temperature gradient, magnetic mirror forces, and wave–particle interactions near the Sun (Lie-Svendsen et al., 1997; Lie-Svendsen and Leer, 2000; Vocks and Mann, 2003; Owens et al., 2008; Smith et al., 2012; Landi et al., 2012; Seough

et al., 2015; Tang et al., 2020; Kolobov et al., 2020). Coulomb collisions affect the evolution of the electron VDF in the solar wind near the corona, which has important implications for exospheric solar-wind models (Jockers, 1970; Landi and Pantellini, 2003; Zouganelis et al., 2005). However, at large distances from the Sun, other mechanisms must be considered for local strahl scattering (Horaites et al., 2018b, 2019; Boldyrev and Horaites, 2019). For instance, the strahl-driven oblique fast-magnetosonic/whistler instability has recently received much attention as such a mechanism (Vasko et al., 2019; Verscharen et al., 2019; López et al., 2020; Jeong et al., 2020; Micera et al., 2020, 2021; Halekas et al., 2021; Sun et al., 2021).

Since the gradients in the plasma and field parameters (e.g., gradients of the solar-wind speed, temperature, and magnetic field) are greater at smaller heliocentric distances, we expect that the electron VDF undergoes a stronger modification near the Sun. Therefore, it is important to model the electron VDF evolution near the Sun, especially in regions that we have not explored with spacecraft yet. For the understanding of local strahl scattering, it is also important to model the evolution of the electron VDF up to large heliocentric distances where the effect of the Parker-spiral geometry of the interplanetary magnetic field is noticeable (Horaites et al., 2018a; Schroeder et al., 2021; Halekas et al., 2021). Many previous studies for the radial kinetic evolution are based on a simplified radial magnetic-field geometry. However, exospheric models suggest that the inclusion of a more realistic, non-radial magnetic field significantly modifies the kinetic properties of the expanding plasma at heliocentric distances beyond $100r_s$ (Chen et al., 1972; Pierrard et al., 2001), where r_s is the solar radius. Moreover, for a comparison of the electron VDF with observations, analytical models must quantify both the bulk parameters and the shape of the electron VDF.

In section 4.2, we derive a gyro-averaged kinetic transport equation that accounts for the spherical expansion of the solar wind and the geometry of the Parker-spiral magnetic field in the heliosphere. Our derivation leads to a kinetic transport equation similar to the transport equations derived by Skilling (1971), Webb (1985), Isenberg (1997), le Roux et al. (2007), le Roux and Webb (2009) and Zank (2013).

In section 4.3, we lay out our numerical treatment for our kinetic transport equation. In section 4.4, we model the kinetic expansion of solar-wind electrons from the corona at a heliocentric distance of $5r_s$, where collisions are more important, to a heliocentric distance of $20r_s$. By applying a fitting scheme to our modeled electron VDFs, we analyse the evolution of the fit parameters with heliocentric distance in the spherically expanding solar wind. We then compare our fit parameters with measurements from Parker Solar Probe (PSP). Furthermore, we show that, at heliocentric distances below $20r_s$, the generated electron strahl is not scattered by the oblique FM/W instability. In section 4.5, we discuss our results. In section 6.4, we present our mathematical strategy for the solution of our three-dimensional kinetic transport equation (2D in velocity space and 1D in configuration space) based on the combination of a Crank–Nicolson scheme in velocity space and a finite-difference Euler scheme in configuration space. In Appendix B, we discuss the effect of our numerical smoothing algorithm in velocity space.

4.2 Kinetic Transport Theory

In this section, we derive a gyro-averaged kinetic transport equation accounting for the non-radial, average spiral shape of the interplanetary magnetic field. Our kinetic transport equation describes the radial evolution of the electron VDF in the spherically expanding solar wind.

4.2.1 Non-Inertial Co-moving Reference Frame

Due to the Sun's rotation, the heliospheric magnetic field follows on average the Parker spiral (Parker, 1958). The spiral structure begins radially near the Sun and then exhibits an increasing relative contribution from the magnetic field's azimuthal component. In Fig. 4.1a, we define two reference frames: (i) the Sun-at-rest frame in spherical coordinates $\mathbf{x} = (R, \Theta, \Phi)$ and (ii) the co-moving wind frame (blue axes) in cylindrical coordinates $\mathbf{q} = (\rho, \phi, z)$. The vector $\mathbf{r} = \hat{\mathbf{e}}_R r$ describes the origin of the co-moving wind frame in the Sun-at-rest frame. The origin of the co-moving wind frame moves into the anti-sunward direction in the Sun-at-rest frame with the wind speed $\mathbf{U}(\mathbf{x}) = \dot{\mathbf{r}} = \hat{\mathbf{e}}_R U$ along the radial direction. We set our solar-wind speed

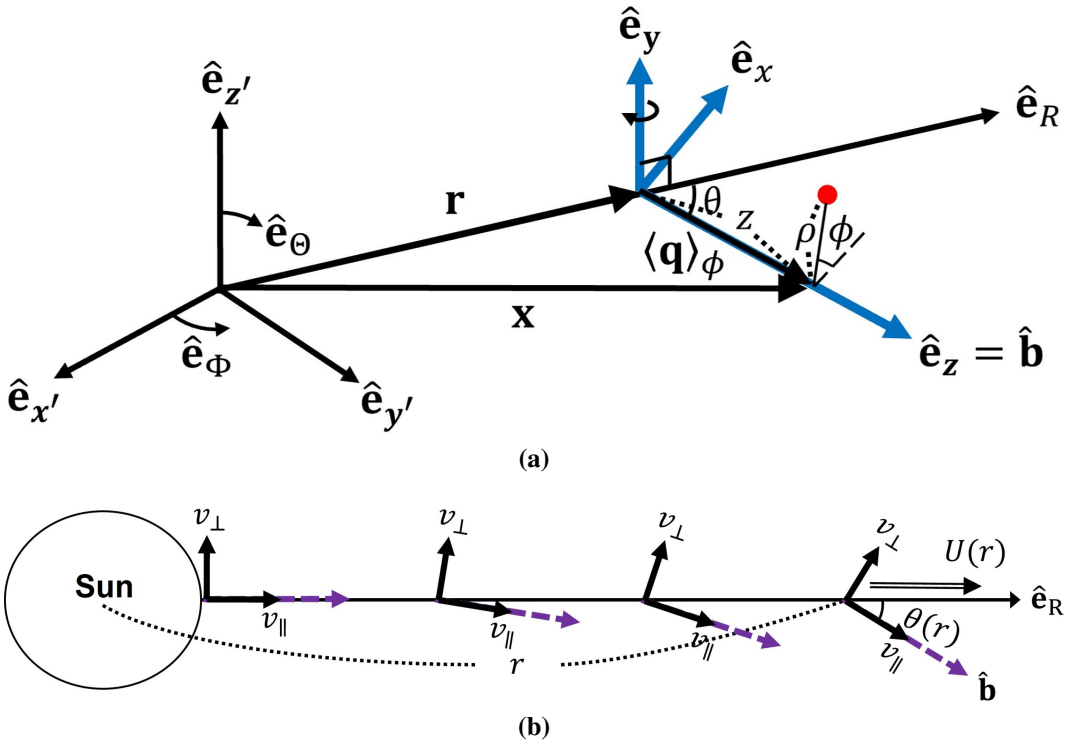

Figure 4.1: (a) Schematic of our reference frames. The Sun-at-rest frame (black axes) is described by the spherical coordinates $\mathbf{x} = (R, \Theta, \Phi)$, and the co-moving wind frame (blue axes) is described by the cylindrical coordinates $\mathbf{q} = (\rho, \phi, z)$. The z-axis of the co-moving wind frame is parallel to the direction of the local magnetic field at distance r, and θ is the angle between the z-axis and the R-axis. (b) Evolution of the velocity-space coordinates in the co-moving reference frame depending on distance from the Sun. The purple dashed arrow indicates the local magnetic field.

profile $\mathbf{U}$ and our background magnetic field profile $\mathbf{B}_0(\mathbf{x}) = \hat{\mathbf{e}}_R B_R - \hat{\mathbf{e}}_\Phi B_\Phi$ so that $\nabla \times (\mathbf{U} \times \mathbf{B}_0) = 0$. We require that the z-axis of the co-moving wind frame is always parallel to the direction of the local magnetic field at distance r. Our wind frame is a non-inertial reference frame due to the acceleration of $\mathbf{U}$ and the rotation of the reference frame from the r-dependence of the angle θ between $\hat{\mathbf{e}}_R$ and $\hat{\mathbf{b}}$, so that fictitious forces occur.

In Fig. 4.1a, the red circle represents a test particle. We define the vector $\mathbf{x}'$ as the spatial coordinate of the test particle:

$$\mathbf{x}' = \mathbf{r} + \mathbf{q} \tag{4.1}$$

and the vector **x** as its gyro-averaged guiding center:

$$\mathbf{x} = \mathbf{r} + \langle \mathbf{q} \rangle_{\phi} = \mathbf{r} + z\hat{\mathbf{b}}, \tag{4.2}$$

where

$$\langle \alpha \rangle_{\phi} \equiv \frac{1}{2\pi} \int_0^{2\pi} \alpha \, d\phi, \tag{4.3}$$

and α is an arbitrary function of ϕ. Using Parker's model (Parker, 1958), we define the unit vector along $\mathbf{B}_0$ as

$$\hat{\mathbf{b}} = \frac{\mathbf{B}_0}{|\mathbf{B}_0|} = \hat{\mathbf{e}}_R \frac{B_R}{B_z} - \hat{\mathbf{e}}_\Phi \frac{B_\Phi}{B_z} = \hat{\mathbf{e}}_R \cos\theta - \hat{\mathbf{e}}_\Phi \sin\theta \tag{4.4}$$

where

$$B_z(r) = \sqrt{B_R^2(r) + B_\Phi^2(r)}, \tag{4.5}$$

$$B_R(r) = B_0 \left(\frac{r_0}{r}\right)^2, \tag{4.6}$$

$$B_\Phi(r) = B_0 \frac{\Omega_\odot}{U(r)} \frac{r_0^2}{r} \sin\Theta, \tag{4.7}$$

B_0 is the reference value of the radial component of the magnetic field at the reference distance r_0, $\Omega_\odot$ is the Sun's rotation frequency and Θ is constant.

Fig. 4.1b illustrates the radial evolution of the velocity-space coordinates in the co-moving solar-wind frame, rotating in accordance with the Parker-spiral geometry. For any given particle, we define its velocity coordinates in the directions perpendicular and parallel with respect to the background magnetic field in the co-moving solar-wind frame as

$$v_\perp = \sqrt{\dot{\rho}^2 + \rho^2 \dot{\phi}^2} \tag{4.8}$$

and

$$v_\parallel = \dot{z}, \tag{4.9}$$

so that $\mathbf{v} = \dot{\mathbf{q}} = \hat{\mathbf{e}}_x v_\perp \cos\phi_v + \hat{\mathbf{e}}_y v_\perp \sin\phi_v + \hat{\mathbf{b}} v_\parallel$, where ϕ_v is the azimuthal angle of the velocity vector in the cylindrical co-moving reference frame. We note that $\hat{\mathbf{e}}_\perp = \hat{\mathbf{e}}_x \cos\phi_v + \hat{\mathbf{e}}_y \sin\phi_v$.

4.2.2 Kinetic Expansion of Solar-Wind Electrons

To study the kinetic evolution of solar-wind electrons along the radial direction, as shown in Fig. 4.1b, we define the electron VDF in six-dimensional phase-space and time as

$$f_e \equiv f_e\left(\mathbf{x}', \mathbf{v}, t\right). \tag{4.10}$$

We define the coordinates so that the configuration space coordinates $\mathbf{x}'$ are in the Sun-at-rest frame while the velocity space coordinates $\mathbf{v}$ are in the co-moving wind frame. The subscript e indicates electron quantities. Based on Eq. (4.10), we calculate the kinetic evolution of f_e under the action of ballistic particle streaming, internal and external forces, and Coulomb collisions. In this thesis, we do not include a term for local wave–particle interactions in our equation. We evaluate the total time derivative of Eq. (4.10) along particle trajectories in phase space according to Liouville's theorem as

$$\frac{\partial f_e}{\partial t} + (\mathbf{U}+\mathbf{v})\cdot\nabla_{\mathbf{x}'} f_e - \left\{\left[(\mathbf{U}+\mathbf{v})\cdot\nabla_{\mathbf{x}'}\right]\mathbf{U}\right\}\cdot\nabla_{\mathbf{v}} f_e + \dot{\mathbf{v}}\cdot\nabla_{\mathbf{v}} f_e = \left(\frac{\partial f_e}{\partial t}\right)_{\text{col}}, \tag{4.11}$$

where

$$\nabla_{\mathbf{v}} \equiv \hat{\mathbf{b}}\frac{\partial}{\partial v_\parallel} + \hat{\mathbf{e}}_\perp \frac{\partial}{\partial v_\perp} + \hat{\mathbf{e}}_{\phi_v}\frac{1}{v_\perp}\frac{\partial}{\partial \phi_v}. \tag{4.12}$$

We discuss the Coulomb-collision term $(\partial f_e/\partial t)_{\text{col}}$ in section 4.2.5. On the left-hand side of Eq. (4.11), the first term describes the explicit variation of f_e with time, the second term quantifies the ballistic particle streaming, the third term corresponds to internal forces caused by the velocity transformation into the (accelerating) co-moving wind frame, and the fourth term corresponds to external forces. We assume that these external forces are only due to the electromagnetic field.

By assuming that the electron's gyro-period is much smaller than the other

involved time scales, f_e can be safely assumed to be gyrotropic and a function of $\mathbf{x}$ instead of $\mathbf{x}'$, so that $f_e \equiv f_e(\mathbf{x}, v_\perp, v_\parallel, t)$. We then apply gyro-phase averaging to Eq. (4.11) as

$$\begin{aligned}&\frac{\partial f_e}{\partial t}+\left(\mathbf{U}+\langle\mathbf{v}\rangle_{\phi_v}\right)\cdot\nabla_{\mathbf{x}} f_e-\left\langle\left[(\mathbf{v}\cdot\nabla_{\mathbf{x}})\mathbf{U}\right]\cdot\hat{\mathbf{e}}_\perp\right\rangle_{\phi_v}\frac{\partial f_e}{\partial v_\perp}\\&-\left\{\left[\left(\mathbf{U}+\langle\mathbf{v}\rangle_{\phi_v}\right)\cdot\nabla_{\mathbf{x}}\right]\mathbf{U}\right\}\cdot\hat{\mathbf{b}}\frac{\partial f_e}{\partial v_\parallel}+\left\langle\dot{v}_\parallel\right\rangle_{\phi_v}\frac{\partial f_e}{\partial v_\parallel}+\langle\dot{v}_\perp\rangle_{\phi_v}\frac{\partial f_e}{\partial v_\perp}=\left(\frac{\partial f_e}{\partial t}\right)_{\text{col}},\end{aligned} \tag{4.13}$$

where

$$\langle\beta\rangle_{\phi_v}\equiv\frac{1}{2\pi}\int_0^{2\pi}\beta\, d\phi_v, \tag{4.14}$$

and β is an arbitrary function of ϕ_v.

4.2.3 Hamiltonian Analysis of External Forces

We apply the Hamiltonian formalism to analyse the external forces exerted on the electrons in the co-moving wind frame, corresponding to the last two terms on the left-hand side of Eq. (4.13). The fundamental mathematics is explained in great detail by Nolting (2016) and Gurnett and Bhattacharjee (2017).

We begin our analysis by defining the Lagrangian $\mathscr{L}$ in the generalised cylindrical coordinates $\mathbf{q}=(\rho,\phi,z)$ in the co-moving wind frame as

$$\mathscr{L}=\frac{1}{2}m_e\mathbf{v}^2+\frac{q_e}{c}\left(\mathbf{A}\cdot\mathbf{v}\right)-q_e\varphi, \tag{4.15}$$

where $\mathbf{v}=\hat{\mathbf{e}}_\rho\dot{\rho}+\hat{\mathbf{e}}_\phi\rho\dot{\phi}+\hat{\mathbf{b}}v_\parallel$, q_e and m_e are the charge and mass of an electron ($q_e=-e$), and c is the speed of light. We assume that, on average, the electric and magnetic fields are static and only depend on the configuration space coordinate $\mathbf{x}'$ so that $\mathbf{E}_0(\mathbf{x}')=\hat{\mathbf{e}}_\rho E_\rho+\hat{\mathbf{e}}_\phi E_\phi+\hat{\mathbf{b}}E_z$ and $\mathbf{B}_0(\mathbf{x}')=\hat{\mathbf{e}}_\rho B_\rho+\hat{\mathbf{e}}_\phi B_\phi+\hat{\mathbf{b}}B_z$. We define the scalar potential $\varphi(\mathbf{x}')$ so that $\mathbf{E}_0=-\nabla_{\mathbf{q}}\varphi$, and the vector potential $\mathbf{A}(\mathbf{x}')=\hat{\mathbf{e}}_\rho A_\rho+\hat{\mathbf{e}}_\phi A_\phi+\hat{\mathbf{b}}A_z$ so that $\mathbf{B}_0=\nabla_{\mathbf{q}}\times\mathbf{A}$. The components of the generalised momentum $\mathbf{p}$ are then given as

$$p_\rho=m_e\dot{\rho}+\frac{q_e}{c}A_\rho, \tag{4.16}$$

$$p_\phi = m_e \rho^2 \dot{\phi} + \frac{q_e}{c} \rho A_\phi, \tag{4.17}$$

and

$$p_z = m_e v_\parallel + \frac{q_e}{c} A_z. \tag{4.18}$$

Assuming that the scalar potential φ depends only on the guiding center $\mathbf{x}$, the electric field $\mathbf{E}_0(\mathbf{x}')$ has no component perpendicular to $\mathbf{B}_0(\mathbf{x})$ and is determined as

$$E_\rho = 0, \quad E_\phi = 0 \quad \text{and} \quad E_z = -\frac{\partial \varphi}{\partial z}. \tag{4.19}$$

Assuming that $\mathbf{B}_0(\mathbf{x}')$ is axially symmetric in the co-moving wind frame (i.e., $B_\phi = 0$), and evaluating $\partial B_z / \partial z$ at the guiding center, Maxwell's equation $\nabla_\mathbf{q} \cdot \mathbf{B}_0 = 0$ leads to

$$B_\rho \approx -\frac{\rho}{2} \left. \frac{\partial B_z}{\partial z} \right|_{\rho=0}. \tag{4.20}$$

Upon substituting Eq. (4.20) into $\mathbf{B}_0 = \nabla_\mathbf{q} \times \mathbf{A}$ and using the Coulomb gauge, we find

$$A_\rho = 0, \quad A_\phi = \frac{\rho}{2} B_z(\mathbf{x}) \quad \text{and} \quad A_z = 0. \tag{4.21}$$

Following Eqs. (4.15) through (4.18) and Eq. (4.21), the Hamiltonian function is given from $\mathscr{H} = \mathbf{p} \cdot \dot{\mathbf{q}} - \mathscr{L}$ as

$$\mathscr{H} = \frac{p_\rho^2}{2m_e} + \frac{p_z^2}{2m_e} + \frac{1}{2m_e \rho^2} \left(p_\phi - \frac{q_e \rho A_\phi}{c} \right)^2 + q_e \varphi. \tag{4.22}$$

The motion of a particle is fully described by Hamilton's equations

$$\dot{\mathbf{p}} = -\frac{\partial \mathscr{H}}{\partial \mathbf{q}} \tag{4.23}$$

and

$$\dot{\mathbf{q}} = \frac{\partial \mathscr{H}}{\partial \mathbf{p}}. \tag{4.24}$$

According to Eq. (4.23), we identify the force terms

$$\dot{p}_\rho = \frac{1}{m_e \rho^3}\left[p_\phi^2 - \left(\frac{q_e \rho^2}{2c} B_z\right)^2\right] \tag{4.25}$$

and

$$\dot{p}_z = \frac{q_e}{2m_e c}\left(p_\phi - \frac{q_e \rho^2}{2c} B_z\right)\hat{\mathbf{b}} \cdot \nabla_{\mathbf{x}} B_z + q_e E_z. \tag{4.26}$$

where we use $B_z = B_z(\mathbf{x})$, $E_z = E_z(\mathbf{x})$, and

$$\frac{\partial B_z(\mathbf{x})}{\partial z} \equiv \hat{\mathbf{b}} \cdot \nabla_{\mathbf{x}} B_z(\mathbf{x}). \tag{4.27}$$

Because ϕ is a cyclic coordinate in Eq. (4.22), the azimuthal equation of motion is

$$p_\phi = m_e \rho^2 \dot{\phi} + \frac{q_e \rho^2}{2c} B_z = \text{const.} \tag{4.28}$$

Without loss of generality, we choose our coordinate axis (z-axis) for a given particle so that ρ is approximately constant on the timescale of a few gyro-periods; i.e., the particle gyrates about the coordinate axis without quickly changing its ρ-coordinate.[1] With this choice, p_ϕ from Eq. (4.25) is

$$p_\phi = -\frac{q_e \rho^2}{2c} B_z. \tag{4.29}$$

Then, Eq. (4.28) leads to

$$\dot{\phi} = -\frac{q_e B_z}{m_e c}, \tag{4.30}$$

which is the electron cyclotron frequency. Using Eqs. (4.25) through (4.30), the

[1] It can be shown that such a coordinate system exists for each individual particle in a homogeneous magnetic field. Even if the magnetic field is inhomogeneous, this choice of coordinate system is still appropriate as long as the gyro-orbits are quasi-circular, which is fulfilled in the regime of adiabatic invariance.

external forces in the $v_{\parallel}$- and $v_{\perp}$-directions are determined by

$$\dot{v}_{\parallel} = \frac{q_e E_z}{m_e} - \frac{v_{\perp}^2}{2B_z}\hat{\mathbf{b}} \cdot \nabla_{\mathbf{x}} B_z \tag{4.31}$$

and

$$\dot{v}_{\perp} = \frac{v_{\perp}}{2B_z}\mathbf{v} \cdot \nabla_{\mathbf{x}} B_z, \tag{4.32}$$

where we use

$$\frac{d}{dt} = \mathbf{v} \cdot \nabla_{\mathbf{x}} \tag{4.33}$$

as the total time derivative in the co-moving reference frame under steady-state conditions. Eqs. (4.31) and (4.32) describe the magnetic mirror force and the electric force exerted on all individual electrons in the co-moving solar-wind frame.

4.2.4 Kinetic Transport Equation and Moments

Substituting Eqs. (4.31) and (4.32) into Eq. (4.13), we obtain

$$\begin{aligned}
&\frac{\partial f_e}{\partial t} + (\mathbf{U} + \langle \mathbf{v} \rangle_{\phi_v}) \cdot \nabla_{\mathbf{x}} f_e - \left\langle \left[(\mathbf{v} \cdot \nabla_{\mathbf{x}}) \mathbf{U} \right] \cdot \hat{\mathbf{e}}_{\perp} \right\rangle_{\phi_v} \frac{\partial f_e}{\partial v_{\perp}} \\
&- \left\{ \left[(\mathbf{U} + \langle \mathbf{v} \rangle_{\phi_v}) \cdot \nabla_{\mathbf{x}} \right] \mathbf{U} \right\} \cdot \hat{\mathbf{b}} \frac{\partial f_e}{\partial v_{\parallel}} + \left(\frac{q_e E_z}{m_e} - \frac{v_{\perp}^2}{2B_z} \hat{\mathbf{b}} \cdot \nabla_{\mathbf{x}} B_z \right) \frac{\partial f_e}{\partial v_{\parallel}} \\
&+ \frac{v_{\perp}}{2B_z} \langle \mathbf{v} \rangle_{\phi_v} \cdot \nabla_{\mathbf{x}} B_z \frac{\partial f_e}{\partial v_{\perp}} = \left(\frac{\partial f_e}{\partial t} \right)_{\mathrm{col}}.
\end{aligned} \tag{4.34}$$

Without loss of generality, we model the kinetic evolution of f_e only at the origin of the co-moving wind frame:

$$\left\langle \frac{df_e}{dt} \right\rangle_{\phi_v} \Bigg|_{z=0} = \left(\frac{\partial f_e}{\partial t} \right)_{\mathrm{col}} \Bigg|_{z=0}. \tag{4.35}$$

We assume that f_e, $\mathbf{U}$, $\mathbf{E}_0$, and $\mathbf{B}_0$ are symmetric in Φ and Θ. We note that $\langle \mathbf{v} \rangle_{\phi_v} = \hat{\mathbf{b}} v_{\parallel}$. We resolve the coefficient of the third term in Eq. (4.34) by applying the

coordinate choice that $\hat{\mathbf{e}}_x = \hat{\mathbf{e}}_R \sin\theta + \hat{\mathbf{e}}_\Phi \cos\theta$, $\hat{\mathbf{e}}_y = -\hat{\mathbf{e}}_\Theta$ (see Fig. 4.1a), and

$$\begin{aligned} \frac{\partial \ln B_z}{\partial r} &= \frac{\partial \ln B_R}{\partial r} - \frac{\partial \ln \cos\theta}{\partial r} \\ &= -\frac{2}{r} + \frac{\sin^2\theta}{r} - \frac{\sin^2\theta}{U}\frac{\partial U}{\partial r}. \end{aligned} \tag{4.36}$$

Then, Eq. (4.35) becomes

$$\begin{aligned} &\frac{\partial f_e}{\partial t} + \left(U + v_\parallel \cos\theta\right)\frac{\partial f_e}{\partial r} + \frac{q_e E_z}{m_e}\frac{\partial f_e}{\partial v_\parallel} \\ &- \left[\left(U + v_\parallel \cos\theta\right)\cos\theta\frac{\partial U}{\partial r} + v_\parallel \sin^2\theta\frac{U}{r}\right]\frac{\partial f_e}{\partial v_\parallel} \\ &+ \frac{v_\perp}{2}\frac{\partial \ln B_z}{\partial r}\left[\left(U + v_\parallel \cos\theta\right)\frac{\partial f_e}{\partial v_\perp} - v_\perp \cos\theta\frac{\partial f_e}{\partial v_\parallel}\right] = \left(\frac{\partial f_e}{\partial t}\right)_{\text{col}}, \end{aligned} \tag{4.37}$$

where $f_e \equiv f_e(r, v_\perp, v_\parallel, t)$, $U \equiv U(r)$, $\theta \equiv \theta(r)$, $E_z \equiv E_z(r)$ and $B_z \equiv B_z(r)$. Eq. (4.37) is our kinetic transport equation for the kinetic evolution in the co-moving frame shown in Fig. 4.1b. Considering Eq. (4.36), our Eq. (4.37) is equivalent to equation (15) by le Roux et al. (2007) after transforming Eq. (4.37) from cylindrical to spherical velocity coordinates. Likewise, our Eq. (4.37) is consistent with the transport equations derived by Lindquist (1966), Skilling (1971), Webb (1985), Isenberg (1997), le Roux and Webb (2009), and Zank (2013).

Assuming that Coulomb collisions do not change the number of particles, we confirm that the zeroth moment of Eq. (4.37) is equivalent to the continuity equation in spherical coordinates with Φ- and Θ-symmetry:

$$\frac{\partial n_e}{\partial t} + \frac{1}{r^2}\frac{\partial [r^2 n_e (U + \overline{U})]}{\partial r} = 0, \tag{4.38}$$

where

$$n_e = \int f_e d^3\mathbf{v}, \tag{4.39}$$

and

$$\overline{U} = \frac{1}{n_e} \int v_{\parallel} f_e d^3\mathbf{v}. \tag{4.40}$$

The $\overline{U}$-term in Eq. (4.38) arises only if our system develops a non-zero bulk velocity in the co-moving reference frame. Our numerical approach guarantees that $\overline{U} = 0$ when the system is in steady state. In such a steady-state configuration leading to $\overline{U} = 0$, the particle flux $r^2 n_e U$ is conserved.

We determine the self-consistent electric field by taking the first moment of Eq. (4.37) and re-arranging the resulting expression to

$$\begin{aligned} E_z(r) = & \frac{m_e}{q_e n_e} \frac{\partial (n_e \overline{U})}{\partial t} + \cos\theta \frac{k_B}{q_e n_e} \frac{\partial (n_e T_{\parallel e})}{\partial r} - \cos\theta \frac{k_B}{q_e} \frac{\partial \ln B_z}{\partial r} (T_{\parallel e} - T_{\perp e}) \\ & + \frac{m_e U}{q_e} \cos\theta \frac{\partial U}{\partial r} - \frac{m_e}{q_e n_e} \int v_{\parallel} \left(\frac{\partial f_e}{\partial t} \right)_{\text{col}} d^3\mathbf{v}, \end{aligned} \tag{4.41}$$

where

$$T_{\parallel e}(r) = \frac{m_e}{k_B n_e} \int v_{\parallel}^2 f_e d^3\mathbf{v}, \tag{4.42}$$

and

$$T_{\perp e}(r) = \frac{m_e}{2 k_B n_e} \int v_{\perp}^2 f_e d^3\mathbf{v}. \tag{4.43}$$

Eq. (4.41) is the same as the generalised Ohm's law based on the electron fluid equation of motion under our assumptions (Lie-Svendsen et al., 1997; Landi and Pantellini, 2003). As our system relaxes to a steady state, the first term in Eq. (4.41) disappears (i.e., Eq. (4.40) is zero). The last term of Eq. (4.41) corresponds to the thermal force by Coulomb collisions (Scudder, 2019). We evaluate the integral in this term numerically.

4.2.5 Coulomb Collisions

In order to model the scattering through Coulomb collisions, we adopt the Fokker–Planck operator given by Ljepojevic et al. (1990) and Vocks (2002) with Rosenbluth potentials (Rosenbluth et al., 1957):

$$\begin{aligned}\left(\frac{\partial f_e}{\partial t}\right)_{\text{col}} = \sum_b \Gamma_{eb}\Bigg(&4\pi\frac{m_e}{m_b}f_b f_e + \frac{\partial H_b}{\partial v_\perp}\frac{\partial f_e}{\partial v_\perp} \\ &+ \frac{\partial H_b}{\partial v_\parallel}\frac{\partial f_e}{\partial v_\parallel} + \frac{1}{2}\frac{\partial^2 G_b}{\partial v_\perp^2}\frac{\partial^2 f_e}{\partial v_\perp^2} + \frac{1}{2}\frac{\partial^2 G_b}{\partial v_\parallel^2}\frac{\partial^2 f_e}{\partial v_\parallel^2} \\ &+ \frac{\partial^2 G_b}{\partial v_\perp \partial v_\parallel}\frac{\partial^2 f_e}{\partial v_\perp \partial v_\parallel} + \frac{1}{2v_\perp^2}\frac{\partial G_b}{\partial v_\perp}\frac{\partial f_e}{\partial v_\perp}\Bigg),\end{aligned} \tag{4.44}$$

where

$$G_b(\mathbf{v}) \equiv \int f_b(\mathbf{v}')|\mathbf{v}-\mathbf{v}'|d^3\mathbf{v}', \tag{4.45}$$

$$H_b(\mathbf{v}) \equiv \frac{m_b - m_e}{m_b}\int f_b(\mathbf{v}')|\mathbf{v}-\mathbf{v}'|^{-1}d^3\mathbf{v}', \tag{4.46}$$

and

$$\Gamma_{eb} \equiv 4\pi\left(\frac{Z_b q_e^2}{m_e}\right)^2 \ln\Lambda_{eb}. \tag{4.47}$$

The subscript b indicates the background particle species. The quantity $\ln\Lambda_{eb}$ is the Coulomb logarithm. We set it to a constant value of $\ln\Lambda_{eb} \approx 25$, which is typical for space plasmas. The parameter Z_b is the charge number of a particle of species b. For the background VDFs, we only consider electrons and protons and assume that the background electron and proton VDFs are gyrotropic and Maxwellian:

$$f_b(r,v) = \frac{n_b}{\pi^{3/2}v_{th,b}^3}\exp\left(-\frac{v^2}{v_{th,b}^2}\right), \tag{4.48}$$

where $v_{th,b}(r) \equiv \sqrt{2k_B T_b(r)/m_b}$, $v^2 = v_\perp^2 + v_\parallel^2$, $n_b(r)$ is the density and $T_b(r)$ is the temperature of the background particles at distance r. Then, the Rosenbluth potentials yield

$$G_b(r,v) = \pi v_{th,b}^4 f_b + n_b\frac{v_{th,b}^2 + 2v^2}{2v}\,\text{erf}\left(\frac{v}{v_{th,b}}\right), \tag{4.49}$$

and

$$H_b(r,v) = \frac{m_b - m_j}{m_b}\frac{n_b}{v}\,\mathrm{erf}\left(\frac{v}{v_{th,b}}\right), \tag{4.50}$$

where $\mathrm{erf}(x)$ is the error function. For numerical reasons, we apply a Taylor expansion for $(v_{th,b}/v)\,\mathrm{erf}(v/v_{th,b})$ at $v/v_{th,b} = 0$ to Eqs. (4.49) and (4.50) if $v/v_{th,b} < 1$.

In our study, we assume that the temperatures of the background electrons and the background protons are equal in our region of interest. The proton-to-electron temperature ratio varies in the solar wind and is generally close to unity only when collisions are sufficient to equilibrate the temperatures (Cranmer, 2020; Verscharen et al., 2019). However, this temperature ratio has only a small impact on our results since it enters our calculation solely via the collision operator.

4.3 Numerical Treatment of the Kinetic Transport Equation

As a first step, we aim to evaluate our model near the Sun at distances (from $r/r_s = 5$ to $r/r_s = 20$), at which direct in-situ measurements of the electron VDF are missing. Even though we only evaluate our kinetic equation Eq. (4.37) near the Sun in this thesis, it is generally valid also at greater distances from the Sun where the effect of the spiral field geometry is greater.

In section 6.4, we present our mathematical approach to numerically solve Eq. (4.37) based on a combination of a Crank–Nicolson scheme in velocity space and an Euler scheme in radial space. Our numerical solution given in Eq. (6.73) implements the time evolution of the electron VDF as a function of r, $v_\perp$ and $v_\parallel$.

4.3.1 Overall Numerical Strategy

We normalise r by r_s, and $v_\perp$ and $v_\parallel$ by the electron Alfvén velocity estimated at 1 au, denoted as v_{Ae0}. We consequently normalise time t in units of r_s/v_{Ae0}. We define the discrete electron VDF as $f^T_{L,M,N} \equiv f_e(r_L, v_{\perp M}, v_{\parallel N}, t^T)$, where the radial index L counts as 1, 2, …, N_r, the velocity indexes M and N count as 1, 2, …, N_v, and the time index T counts as 1, 2, …(see also section 6.4). We iterate the calculation of our numerical solution according to Eq. (6.73) until the 2-norm of the

residual difference in subsequent VDFs,

$$\|f^{T+1}_{L,M,N} - f^{T}_{L,M,N}\|_2 = \left[\sum_{L=1}^{N_r}\sum_{M=1}^{N_v}\sum_{N=1}^{N_v} |f^{T+1}_{L,M,N} - f^{T}_{L,M,N}|^2\right]^{1/2}, \tag{4.51}$$

reaches a minimum value, which we identify with a quasi-steady state. After reaching this quasi-steady state, we only analyse the dependence of $f^{T}_{L,M,N}$ on r, $v_\perp$, and $v_\parallel$.

During our calculation, we update the electric field every 50 time steps via Eq. (4.41) and the collisional background species parameters in Eq. (4.48) through Eqs. (4.39), (4.42), (4.43) and

$$T_e = \frac{2T_{\perp e} + T_{\parallel e}}{3}. \tag{4.52}$$

In our calculation, the radial step size is $\Delta r/r_s = 0.25$, the step size in velocity space is $\Delta v/v_{Ae0} = 0.45$, and the size of the time step is $\Delta t/(v_{Ae0}/r_s) = 1.2\times10^{-3}$.

4.3.2 Initial Conditions

At the coronal lower boundary of our simulation domain, collisions are sufficient to create a Maxwellian thermal core of the electrons. However, non-thermal tails can already exist at $r = 5r_s$. Non-Maxwellian electron distributions in the corona are often evoked in kinetic models of the solar wind (Scudder, 1992b,a; Maksimovic et al., 1997; Viñas et al., 2000). Therefore, we select a κ-distribution with $\kappa = 8$ for the initial electron VDF (Livadiotis and McComas, 2009; Livadiotis and McComas, 2013; Nicolaou and Livadiotis, 2016):

$$f_e = \frac{n_e}{v^3_{th,e}}\left[\frac{2}{\pi(2\kappa-3)}\right]^{3/2}\frac{\Gamma(\kappa+1)}{\Gamma(\kappa-0.5)}\left(1+\frac{2}{2\kappa-3}\frac{v^2}{v^2_{th,e}}\right)^{-\kappa-1}, \tag{4.53}$$

where $\Gamma(x)$ is the Γ-function and $\kappa > 3/2$ is the κ-index.

Even though there is a wide range of natural variation, we prescribe representative initial profiles in our region of interest for the bulk speed as (Bemporad, 2017;

Yakovlev and Pisanko, 2018)

$$U(r) = (400\,\mathrm{km/s})\tanh\left(\frac{r}{10r_s}\right), \tag{4.54}$$

for the electron density as

$$n_e(r) = (5\,\mathrm{cm}^{-3})\left(\frac{215r_s}{r}\right)^2\left(\frac{U(r=215r_s)}{U(r)}\right), \tag{4.55}$$

and for the electron temperature as (Marsch et al., 1989; Moncuquet et al., 2020)

$$T_e(r) = (10^6\,\mathrm{K})\left(\frac{5r_s}{r}\right)^{0.8}. \tag{4.56}$$

In Eq. (4.55), the factor $U(r=215\,r_s)/U(r)$ guarantees mass-flux conservation under steady-state conditions (i.e., $r^2 n_e U = \mathrm{const}$). We assume that the profile of $U(r)$ stays constant during our calculation. Thus, $U(r)$ starts from 185 km/s at the inner boundary and reaches 385 km/s at the outer boundary of our integration domain. However, the profiles of n_e and T_e evolve through the evolution of f_e. By applying Eqs. (4.54) through (4.56) to Eq. (4.53), we initially define our electron VDF at all radial distances. We also initially apply Eqs. (4.54) through (4.56) to Eq. (4.48) for the collisional background species. For the background magnetic field in Eq. (4.5), we set $B_0 = 0.037\,\mathrm{G}$ and $r_0 = 5r_s$ based on the PSP measurements presented by Badman et al. (2021). We focus our analysis on the equatorial heliospheric plane (i.e., $\Theta = 90^\circ$). We then calculate $v_{Ae0} = 836\,\mathrm{km/s}$ by using Eq. (4.5) and Eq. (4.55).

4.3.3 Boundary Conditions and Smoothing in Velocity Space

For the boundary conditions in velocity space, we first estimate the ratios between adjacent VDFs in $v_\parallel$ and $v_\perp$ as

$$\Upsilon^T_{\parallel L,M,N} = \frac{f^T_{L,M,N}}{f^T_{L,M,N+1}} \tag{4.57}$$

and

$$\Upsilon^{T}_{\perp L,M,N} = \frac{f^{T}_{L,M,N}}{f^{T}_{L,M+1,N}}. \tag{4.58}$$

We then update the VDF values at the given boundary in each time step by using Eqs. (4.57) and (4.58), evaluated at the previous time step, as

$$f^{T}_{L,M,1} = f^{T}_{L,M,2}\Upsilon^{T-1}_{\parallel L,M,1}, \tag{4.59}$$

$$f^{T}_{L,M,N_v} = \frac{f^{T}_{L,M,N_v-1}}{\Upsilon^{T-1}_{\parallel L,M,N_v-1}}, \tag{4.60}$$

$$f^{T}_{L,1,N} = f^{T}_{L,2,N}\Upsilon^{T-1}_{\perp L,1,N}, \tag{4.61}$$

and

$$f^{T}_{L,N_v,N} = \frac{f^{T}_{L,N_v-1,N}}{\Upsilon^{T-1}_{\perp L,N_v-1,N}}. \tag{4.62}$$

To avoid numerical errors caused by our limited velocity resolution, we apply an averaging scheme to smooth the VDFs in velocity space. We average $f^{T}_{L,M,N}$ in each time step by using Eqs. (4.57) and (4.58), evaluated at the previous time step, as

$$\begin{aligned}\langle f\rangle^{T}_{L,M,N} = &\frac{f^{T}_{L,M,N+1}\Upsilon^{T-1}_{\parallel L,M,N+1}}{8} + \frac{f^{T}_{L,M,N-1}}{8\Upsilon^{T-1}_{\parallel L,M,N-1}} \\ &+ \frac{f^{T}_{L,M,N}}{2} + \frac{f^{T}_{L,M+1,N}\Upsilon^{T-1}_{\perp L,M,N}}{8} + \frac{f^{T}_{L,M-1,N}}{8\Upsilon^{T-1}_{\perp L,M-1,N}},\end{aligned} \tag{4.63}$$

where we denote the averaged VDF as $\langle f\rangle^{T}_{L,M,N}$. The approach described by Eq. (4.63) improves the numerical stability without changing the physics of the model. In Appendix B, we show the result of our model without smoothing for comparison.

4.3.4 Boundary Conditions and Smoothing in Configuration Space

For the outer boundary in our r-coordinate, we first estimate the ratio between radially adjacent VDFs at the initial time step $T = 1$ as

$$\Upsilon_{L,M,N} = \frac{f^1_{L,M,N}}{f^1_{L+1,M,N}}. \tag{4.64}$$

We then update the VDF at the outer boundary in each time step by using Eq. (4.64) as

$$f^T_{N_r,M,N} = \frac{f^T_{N_r-1,M,N}}{\Upsilon_{N_r-1,M,N}}. \tag{4.65}$$

This corresponds to an open outer boundary condition at $L = N_r$.

The corona is so collisional that the assumption of a constant isotropic VDF at the inner boundary at $r = 5r_s$ is reasonable. Thus, we require that our initial VDF at the inner boundary, denoted as $f^T_{1,M,N}$, remains constant throughout our calculation. This choice of a constant inner boundary in conjunction with the large radial gradients at small r can lead to a fast growth of numerical errors. In order to compensate for these errors, we apply an averaging scheme to smooth the VDF in configuration space, following a similar scheme as described in section 4.3.3 for velocity space. We average $f^T_{L,M,N}$ (except for $f^T_{1,M,N}$ and $f^T_{N_r,M,N}$) in each time step by using Eq. (4.64) as

$$\langle f \rangle^T_{L,M,N} = \frac{f^T_{L-1,M,N}}{4\Upsilon_{L-1,M,N}} + \frac{f^T_{L,M,N}}{2} + \frac{f^T_{L+1,M,N}\Upsilon_{L,M,N}}{4}. \tag{4.66}$$

We apply the averaging in configuration space before the averaging in velocity space.

4.4 Results

4.4.1 Kinetic Expansion

Following the numerical treatment discussed in section 4.3, we acquire the results for the kinetic evolution of the electron VDF from $r/r_s = 5$ to $r/r_s = 20$ according to Eq. (4.37). We show the two-dimensional electron VDF both at $r/r_s = 5$ and at $r/r_s = 20$ in Fig. 4.2. Fig. 4.3 shows one-dimensional cuts along the $v_{\parallel}$-direction

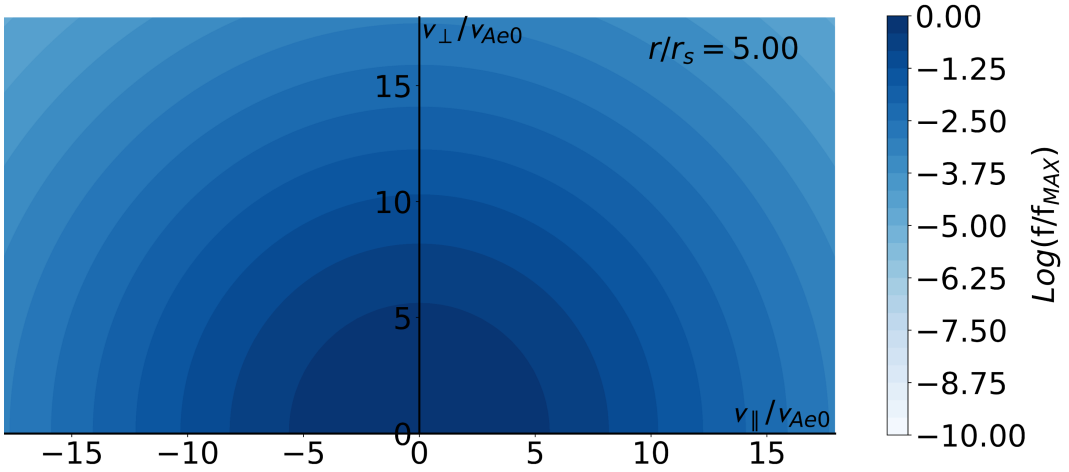

(a) $r/r_s = 5$

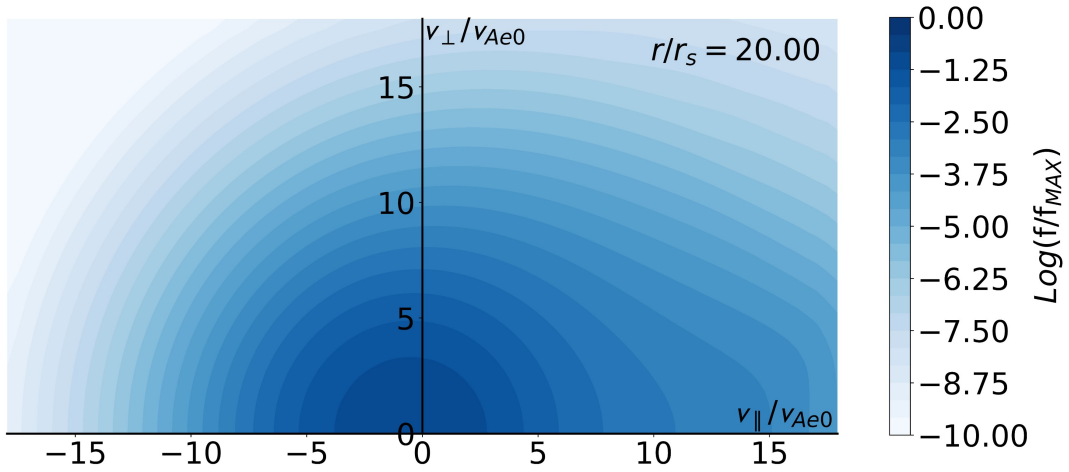

(b) $r/r_s = 20$

Figure 4.2: Kinetic evolution of the electron VDF from (a) $r/r_s = 5$ to (b) $r/r_s = 20$. The value of the distribution function is normalised to the maximum value of the VDF at the inner boundary. The electron density decreases due to spherical expansion. The effects of particle streaming and the magnetic mirror force mainly contribute to the formation of the electron strahl at positive $v_{\parallel}$ and small $v_{\perp}$. Because of the electric field, the electron core slightly shifts towards negative $v_{\parallel}$. Panels (a) and (b) show the initial and final snapshots of the electron VDF.

of the same distributions shown in Fig. 4.2. Fig. 4.2a and the black solid curve in Fig. 4.3 show the electron VDF at $r/r_s = 5$. Fig. 4.2b and the black dashed curve in Fig. 4.3 show the electron VDF at $r/r_s = 20$. This kinetic evolution is the result from the combined effects of the accelerating solar wind, particle streaming, the magnetic mirror force, the electric field, the geometry of the Parker-spiral magnetic field, and Coulomb collisions throughout the spherical expansion.

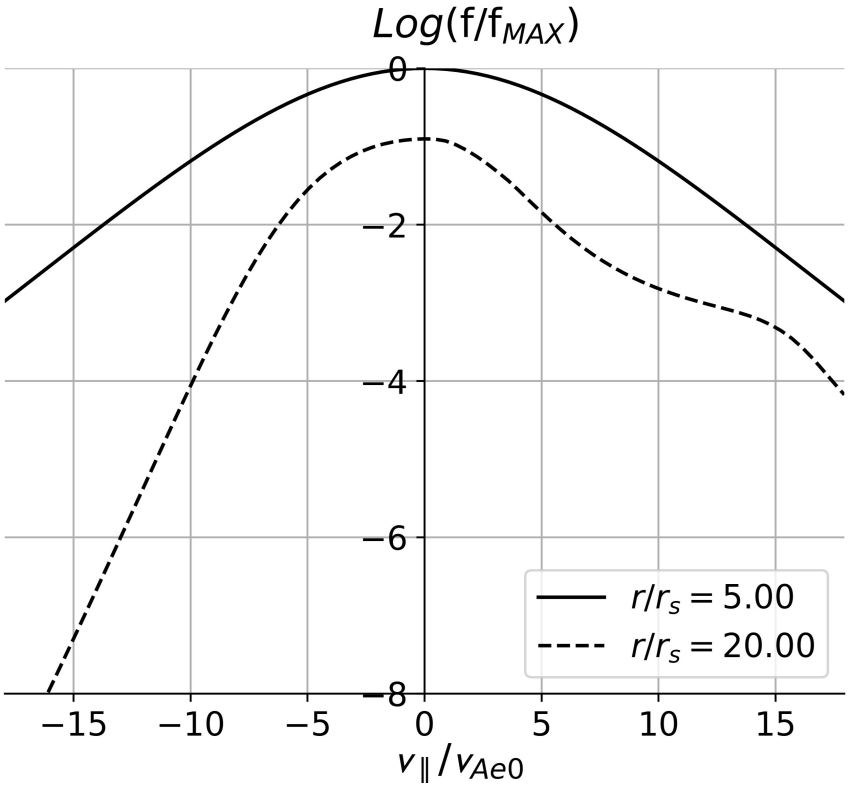

Figure 4.3: Kinetic evolution of the electron VDF as cuts in the $v_{\parallel}$-direction. The figure shows the initial and final snapshots of the electron VDF.

In Fig. 4.4, the black solid curve represents the radial density profile calculated with Eq. (4.39). Both Figs. 4.2 and 4.3 illustrate that the electron density decreases from $1.9 \times 10^4\,\mathrm{cm}^{-3}$ to $0.1 \times 10^4\,\mathrm{cm}^{-3}$ in our region of interest as a consequence of the spherical expansion. The blue dashed curve in Fig. 4.4 is our initial density profile according to Eq. (4.55). The difference between both profiles shows that, during our calculation, the density profile of the electron VDF stays nearly constant to satisfy Eq. (4.38) under steady-state conditions as expected. The red dashed curve represents a $1/r^2$-profile for comparison. Because the solar wind still under-

goes acceleration in our model domain according to Eq. (4.54), the electron density decreases faster with distance than the $1/r^2$-profile (see the first term in the second line of Eq. (4.37)).

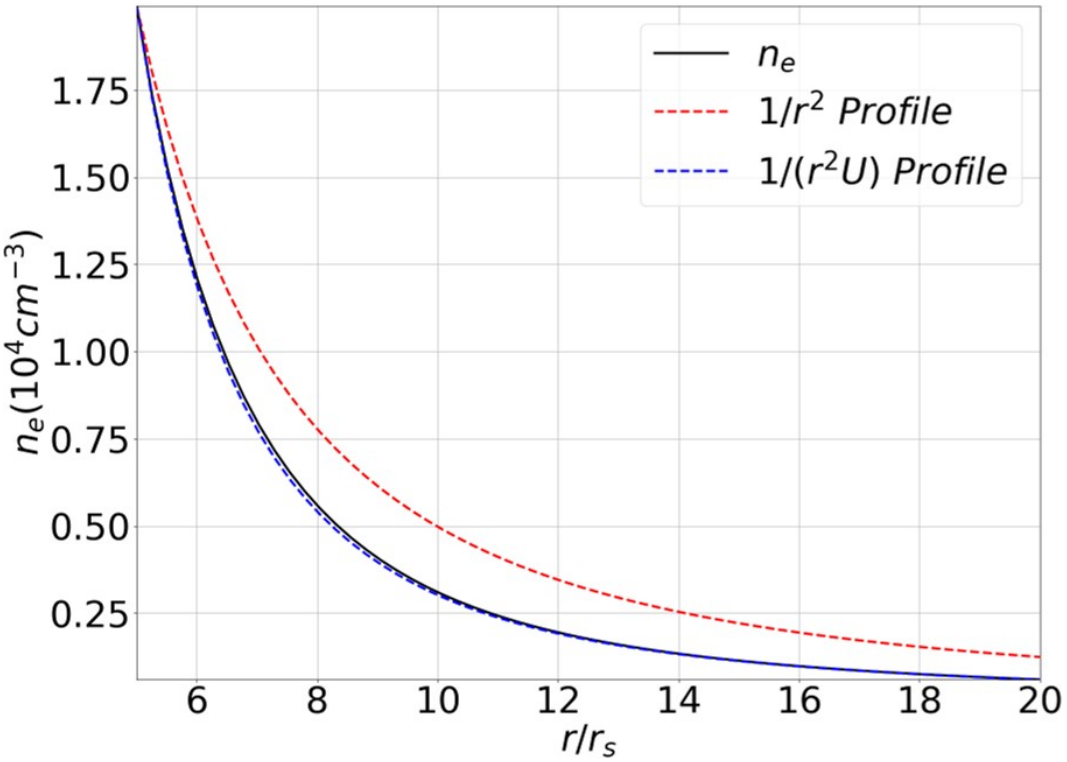

Figure 4.4: Profiles of the electron density as a function of radial distance. The black solid curve shows the density as calculated from the electron VDFs with Eq. (4.39). The blue dashed curve is the initial profile of the electron density given by Eq. (4.55). The red dashed curve shows a $1/r^2$-profile for reference.

Electrons with $(U + v_{\parallel}\cos\theta) < 0$ stream into the sunward direction, while electrons with $(U + v_{\parallel}\cos\theta) > 0$ stream into the anti-sunward direction. Electrons with $(U + v_{\parallel}\cos\theta) > 0$ are continuously supplied from the Sun to our system. The streaming, in combination with our radial temperature gradient given in Eq. (4.56), causes a deformation of the VDF with time according to the second term in the first line of Eq. (4.37). Therefore, the streaming effect contributes to the creation of the electron strahl above around $v_{\parallel}/v_{Ae0} = 10$. Because of this deformation of the VDF, the magnetic mirror force (the terms in the third line of Eq. (4.37)) becomes more effective in the anti-sunward direction and focuses the electrons towards smaller $v_{\perp}$ at $(U + v_{\parallel}\cos\theta) > 0$.

The electric field contributes with a sunward acceleration to the electron bulk motion. This effect moves the center of the electron core, whose thermal energy is well below the electric potential energy, toward negative $v_{\parallel}$ as the solar wind expands (see the third term in the first line of Eq. (4.37)). Moreover, the electric field guarantees that the bulk speed in the co-moving wind frame, Eq. (4.40), stays at a value of zero. This situation means that our system always fulfils $\overline{U} = 0$. Because of the fictitious force in the co-moving wind frame (second term in the second line of Eq. (4.37)), most of the electrons in the VDF are accelerated to larger $v_{\parallel}$. At small velocities in Fig. 4.2, the electrons are isotropic, which is the core part of the VDF. This core isotropy is due to the Coulomb collisions that isotropize more efficiently at small velocities.

4.4.2 Electron VDF Fits

We apply fits to our numerical results for the electron VDF to quantify the core and strahl parameters and to compare our results with observations. Our fit routine uses the Nelder–Mead method in logarithmic space. We fit our electron VDFs with the sum of two bi-Maxwellian distributions for the electron core and strahl (Štverák et al., 2009):

$$f_{\text{fit}} = f_c + f_s, \tag{4.67}$$

where

$$f_c = \frac{n_c}{\pi^{3/2} v_{\perp th,c}^2 v_{\parallel th,c}} \exp\left[-\frac{v_{\perp}^2}{v_{\perp th,c}^2} - \frac{(v_{\parallel} - U_c)^2}{v_{\parallel th,c}^2} \right], \tag{4.68}$$

$$f_s = \frac{n_s}{\pi^{3/2} v_{\perp th,s}^2 v_{\parallel th,s}} \exp\left[-\frac{v_{\perp}^2}{v_{\perp th,s}^2} - \frac{(v_{\parallel} - U_s)^2}{v_{\parallel th,s}^2} \right], \tag{4.69}$$

$v_{\perp th,j} \equiv \sqrt{2k_B T_{\perp j}/m_e}$, $v_{\parallel th,j} \equiv \sqrt{2k_B T_{\parallel j}/m_e}$, and the subscript j indicates each electron population ($j = c$ for the core and $j = s$ for the strahl). In our fit parameters, we set $n_s = n_e - n_c$, where n_c and n_s are the core and strahl densities, $T_{\perp c}$ ($T_{\parallel c}$) and $T_{\perp s}$ ($T_{\parallel s}$) are the perpendicular (parallel) temperatures of core and strahl, and U_c and U_s are the bulk velocities of the core and the strahl.

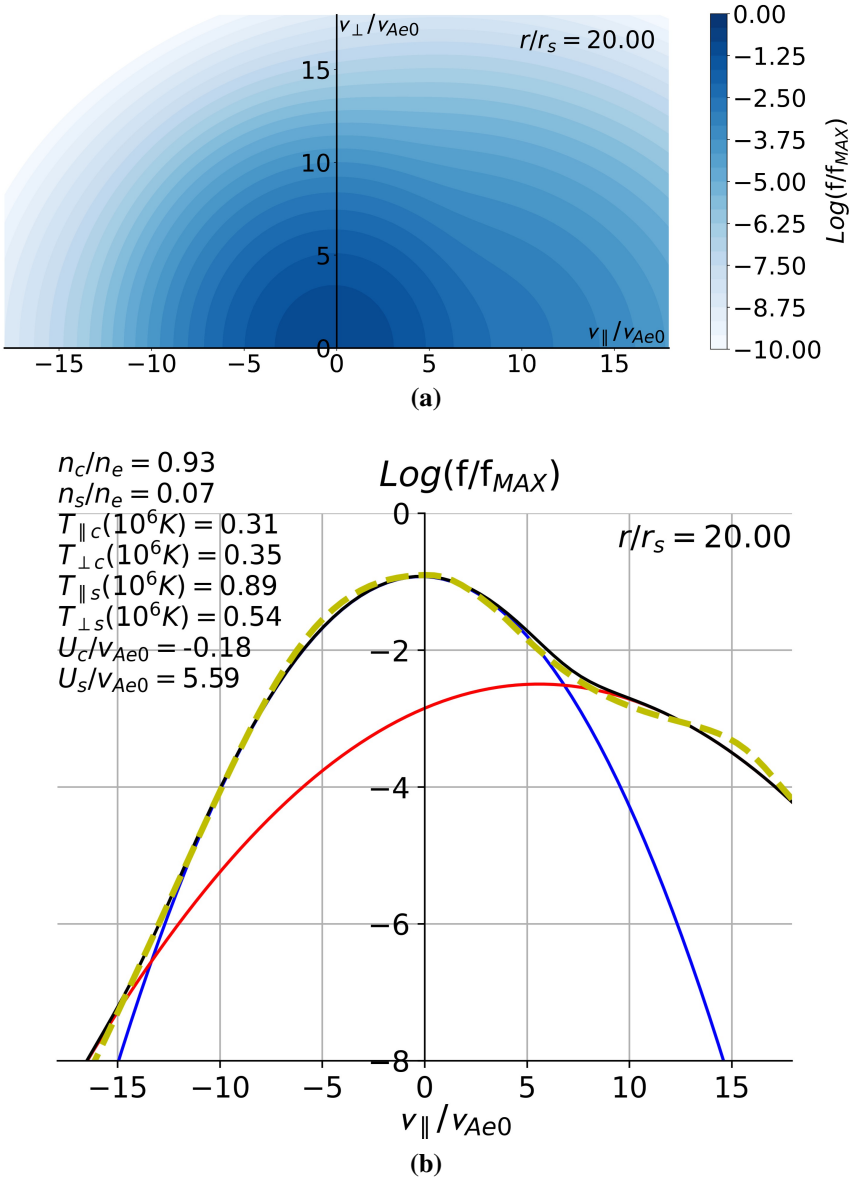

Figure 4.5: Fit results for the electron VDF. (a) Two-dimensional fit result at $r/r_s = 20$. The input VDF is the simulation result shown in Fig. 4.2b; (b) one-dimensional cut of the electron VDF in the $v_\parallel$-direction. The fit parameters are given in the figure. The blue and red solid curves are the fit results for the core and strahl, respectively. The black solid curve is the sum of both fits according to Eq. (4.67), and the yellow dashed curve is the same as the dashed curve in Fig. 4.3.

Fig. 4.5a shows our fit result for the electron VDF at $r/r_s = 20$, for which Fig. 4.2b shows the underlying direct numerical output. Fig. 4.5b shows the corresponding one-dimensional cut of the VDF in the $v_\parallel$-direction. In the top left corner of Fig. 4.5b, we provide the fit parameters from our analysis. The blue and red solid

curves show the fitted VDFs for the core and strahl, respectively. The black solid curve shows the total f_{fit}, and the yellow dashed curve is our direct numerical result; i.e., the same as the black dashed curve in Fig. 4.3. We fit the electron VDFs at all radial distances from our numerical results. After fitting all electron VDFs, the normalised sum of squared residuals is always less than 0.013, which quantifies the good agreement between our numerical results and the fit results (Abraham et al., 2021).

Fig. 4.6 shows radial profiles for a selection of fit parameters from our model. The blue and red curves in each profile correspond to the core and strahl fit parameters, respectively. The small discontinuity at $r/r_s \approx 13$ in Fig. 4.6 is a numerical error originating from the fitting. According to Fig. 4.6a, the relative density of the electron strahl near the inner boundary is around 26% of the total electron density. Such a high percentage is mostly a numerical artifact from our fitting scheme, which occurs whenever the fitted core and strahl VDFs largely overlap because of a small U_c and U_s (Maksimovic et al., 2005; Štverák et al., 2009). At larger distances, the relative strahl density decreases continuously towards 7% at the outer boundary.

According to Fig. 4.6b, U_s increases from the inner boundary and then stays nearly constant at around $U_s/v_{Ae0} = 5.6$ for $r/r_s \gtrsim 15$. At the same time, U_c decreases near the inner boundary as a consequence of the strong electric field near the corona.

As shown in Fig. 4.6c, $T_{\parallel s}$ decreases rapidly near the inner boundary, and then stays nearly constant at around 9×10^5 K at larger distances. On the other hand, $T_{\perp s}$, $T_{\perp c}$ and $T_{\parallel c}$ steadily decrease. We find that $T_{\perp c} > T_{\parallel c}$ in all of our fit results (except for the inner boundary, where $T_{\perp c} = T_{\parallel c}$).

Fig. 4.6d shows the ratio between the parallel thermal pressure to the magnetic-field pressure, $\beta_{\parallel j} = 8\pi n_j k_B T_{\parallel j}/B_z^2$ separately for the core and for the strahl population. Both $\beta_{\parallel c} \ll 1$ and $\beta_{\parallel s} \ll 1$. We find that $\beta_{\parallel s}$ stays approximately constant at around 0.02 while $\beta_{\parallel c}$ steadily increases with distance.

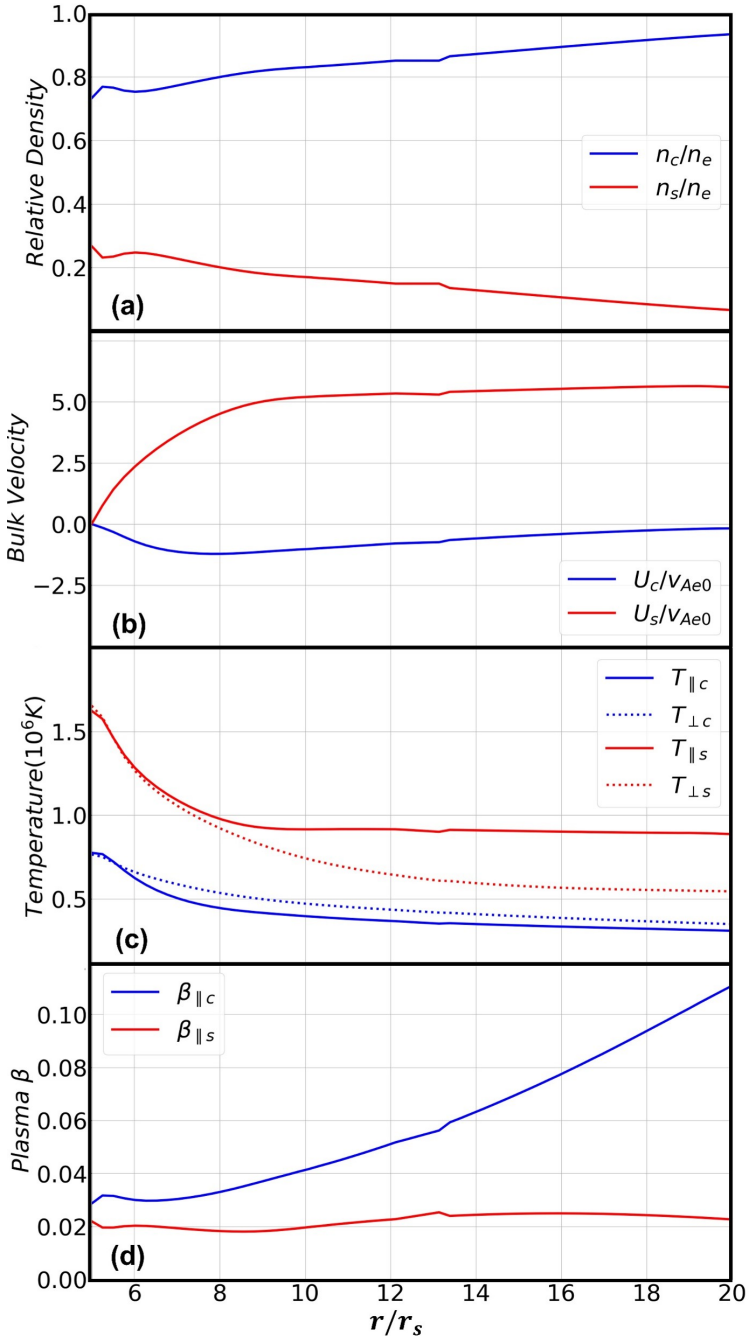

Figure 4.6: Radial profiles from our fit results of (a) the relative densities, where $n_e = n_c + n_s$; (b) the population bulk velocities; (c) their temperatures; and (d) $\beta_{\parallel c}$ and $\beta_{\parallel s}$. The blue curves show core parameters, and the red curves show strahl parameters.

4.4.3 Comparison with PSP Data

We compare our numerical results with measurements from the dataset by Abraham et al. (2021). This dataset is based on fits to the observed level-3 electron

distributions provided by the Solar Wind Electron Alphas and Protons (SWEAP) instrument suite (Kasper et al., 2016; Whittlesey et al., 2020) on board PSP. The analysis method fits bi-Maxwellian distributions to the core and strahl and a bi-κ-distribution to the halo. Because data below 30 eV are contaminated with secondary electrons, the dataset neglects all measurement points below 30 eV. In the Abraham et al. (2021) dataset, most VDFs ($\sim$4200 in total) can be fully modelled with bi-Maxwellian core and strahl VDFs, without the need to include a halo distribution in the range of radial distances between $r/r_s = 20.3$ and $r/r_s = 21.3$.

Fig. 4.7a shows, as a typical example, the fitted electron VDF measured by PSP at a distance of $r/r_s = 20.96$ on 27 September 2020 at 20:24:18 UTC during encounter 6. Fig. 4.7b is the corresponding one-dimensional cut of the electron VDF in the $v_{\parallel}$-direction. The blue and red solid curves are the fitted VDFs for the core and strahl from the PSP data. We provide the fit parameters in the top left corner of Fig. 4.7b. The black solid curve is the sum of the core and strahl fits, and the yellow dashed curve is the same as the black dashed curve in Fig. 4.3 from our numerical results.

Comparing the PSP measurement with the fitted VDF from our numerical results in Fig. 4.5, we find that our model produces $n_s/n_e = 7\%$ at $r/r_s = 20$ which is close to the observed value. The values of $T_{\parallel s}$ and $T_{\perp s}$ from our model are 1.2 and 1.7 times greater, while the values of $T_{\parallel c}$ and $T_{\perp c}$ from our model are 0.7 and 0.9 times less than the values from the PSP observation. The shoulder-like strahl structure at around $v_{\parallel}/v_{Ae0} \gtrsim 10$ is more distinct in our model results than in the PSP data. We find a core temperature anisotropy with $T_{\perp c} < T_{\parallel c}$ in Fig. 4.7b, which is opposite to the anisotropy found in Fig. 4.5b. We note that U_c is zero in Fig. 4.7 while U_c in Fig. 4.5 is slightly negative; however, this difference is likely due to the choice of reference frame in the PSP level-3 data and associated uncertainties when U_c is small. Lastly, our model produces $U_s/v_{Ae0} = 5.59$ at $r/r_s = 20$ which is close to the observed value.

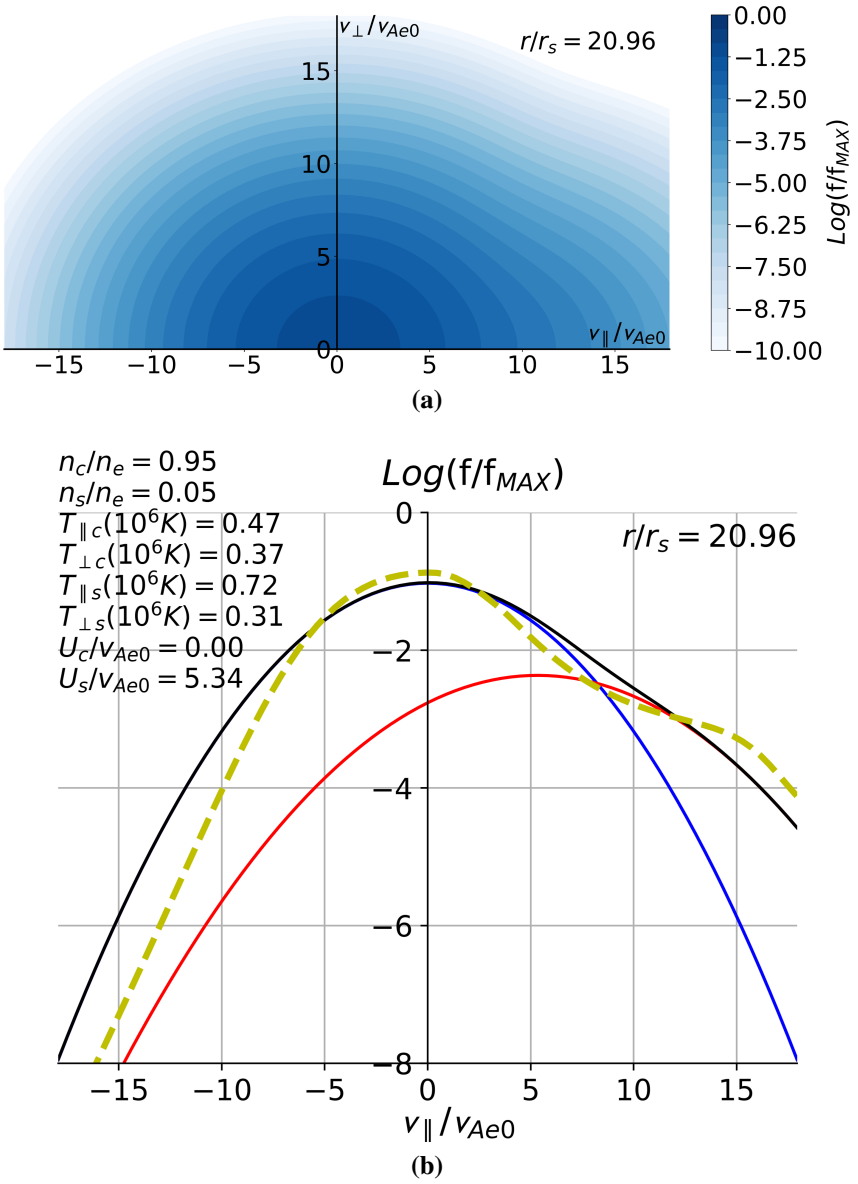

Figure 4.7: (a) The fitted electron VDF measured by PSP at a distance of $r/r_s = 20.96$ on 27 September 2020 at 20:24:18 UTC during encounter 6; (b) the corresponding one-dimensional cut of the electron VDF in the $v_\parallel$-direction, with the fit parameters in the top left corner. The blue and red solid curves are the fit results for the core and strahl based on the PSP data. The black solid curve is the sum of the core and strahl fits, and the yellow dashed curve is the same as the black dashed curve in Fig. 4.3.

4.4.4 Oblique Fast-magnetosonic/Whistler Instability

We now investigate the possibility for the oblique FM/W instability to scatter strahl electrons into the halo as the solar wind expands into the heliosphere. The oblique FM/W instability has received major attention lately as a mechanism to explain

the halo formation (Vasko et al., 2019; Verscharen et al., 2019; López et al., 2020; Jeong et al., 2020; Micera et al., 2020, 2021; Halekas et al., 2021; Sun et al., 2021). For this investigation, we compare our fit parameters from section 4.4.2 with the theoretically predicted threshold for the oblique FM/W instability in the low-$\beta_{\|c}$ regime given by Verscharen et al. (2019). According to this framework, the oblique FM/W instability is unstable if

$$U_s \gtrsim 3v_{\|th,c}. \tag{4.70}$$

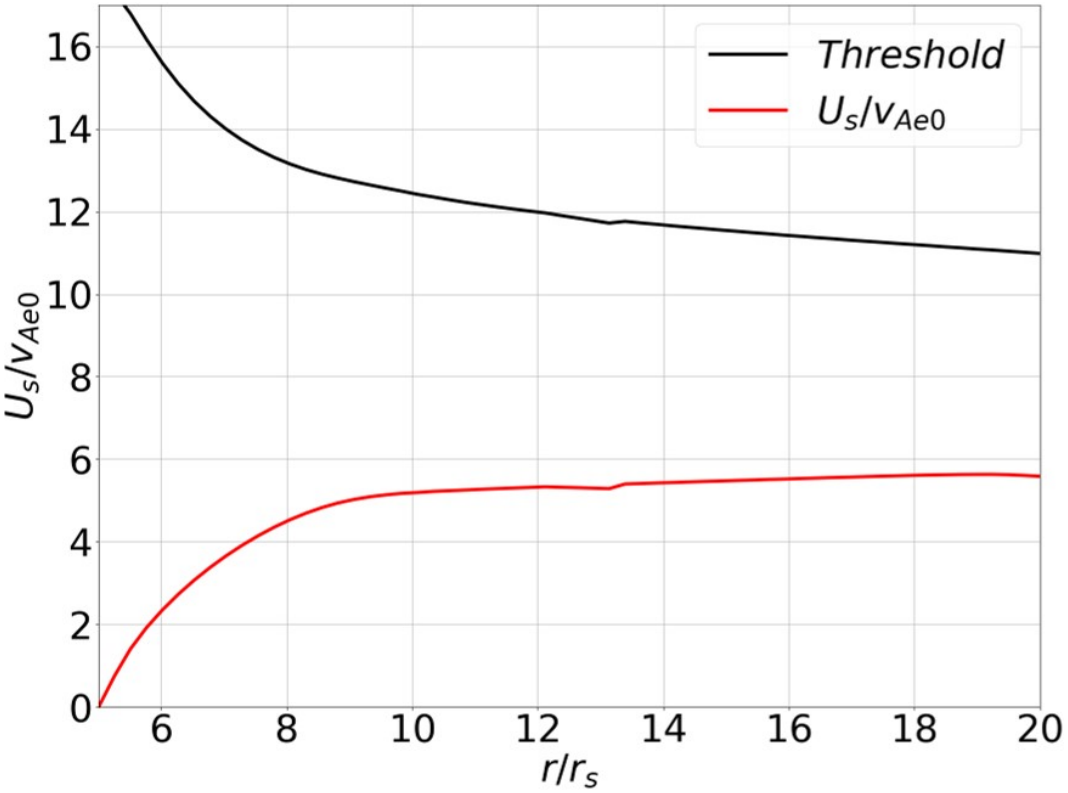

Figure 4.8: Comparison of the strahl bulk velocity with the threshold for the oblique FM/W instability. The red curve corresponds to U_s/v_{Ae0}, and the black curve shows $3v_{\|th,c}/v_{Ae0}$. According to Eq. (4.70), the oblique FM/W instability is unstable if $U_s \gtrsim 3v_{\|th,c}$. In our region of interest, the electron strahl does not cross the instability threshold.

Fig. 4.8 shows U_s/v_{Ae0} as a red solid curve and the threshold from Eq. (4.70) normalised in units of v_{Ae0} as a black solid curve, both as functions of radial dis-

tance. In our region of interest, the plasma does not cross the threshold for the oblique FM/W instability. This suggests that the electron strahl, under the typical parameters reproduced by our model, is not scattered by the oblique FM/W instability at these distances from the Sun. However, U_s stays approximately constant at distances greater than $r/r_s = 15$ while the threshold decreases with distance due to the decrease in $T_{\|c}$. The difference between the strahl speed and the threshold decreases with increasing distance. Therefore, assuming that this trend continues, we hypothesise that the electron strahl scattering by the oblique FM/W instability sets in at a critical distance $r_{\rm crit}/r_s > 20$ from the Sun. The value of $r_{\rm crit}$ is not known yet. In addition, the oblique FM/W instability transitions into a high-$\beta_{\|c}$ regime when $\beta_{\|c} \gtrsim 0.25$ (Verscharen et al., 2019), which occurs beyond $r/r_s = 20$. We also note that, within the natural variability of the solar-wind parameters, crossings of the oblique FM/W-instability threshold can occur sporadically at times of particularly fast strahl or cold core conditions. These outlier conditions are not covered in our representative model.

4.5 Discussion

We derive a gyro-averaged kinetic transport equation for the global kinetic expansion of the solar wind in a Parker-spiral magnetic field. By numerically solving our kinetic transport equation, we model the spherical expansion of an isotropic electron VDF at heliocentric distances from $r/r_s = 5$ to $r/r_s = 20$. The comparison of electron VDFs between our results and PSP observation shows a good agreement on average. Our numerical model creates a slightly stronger strahl than observed, possibly because we set our lower-boundary VDF to a κ-distribution with $\kappa = 8$ instead of a Maxwellian. We confirm that, if the lower-boundary VDF is a κ-distribution, the strahl formation is more distinct. We attribute this minor difference to the increased population of suprathermal strahl seed particles in the tail of the lower-boundary κ-distribution compared to a Maxwellian.

The core temperature anisotropy in our model ($T_{\perp c} > T_{\|c}$ in Fig. 4.5b) is opposite to the anisotropy in the PSP observation ($T_{\perp c} < T_{\|c}$ in Fig. 4.7b). In our model

results, the core anisotropy with $T_{\perp c} > T_{\parallel c}$ is likely generated because the sunward-streaming electrons in the VDF (i.e., those electrons with $U + v_{\parallel} \cos\theta < 0$) de-focus with increasing time. This result implies that the core parallel heating is absent in our model. A possible explanation for the difference in core anisotropy between our numerical results and the observations is that, in reality, the core electrons already have a temperature anisotropy with $T_{\perp c} < T_{\parallel c}$ at the lower boundary of our integration domain. Additional core parallel-heating mechanisms, such as electron Landau damping of kinetic Alfvén waves (Chen et al., 2019), are a possible explanation for this difference in core anisotropy.

Beyond $r/r_s = 20$, we expect that the electron strahl continues to evolve because the electron temperature continuously decreases and the magnetic mirror force is still effective. However, with further distance, this type of strahl processing becomes ineffective due to the weakened gradients of the magnetic field and temperature (Owens et al., 2008; Štverák et al., 2015; Moncuquet et al., 2020). Then, the initially formed strahl traverses towards larger distances without undergoing a significant evolution (apart from a density decrease due to expansion), unless it experiences local scattering mechanisms. As suggested in section 4.4.4, if the strahl bulk velocity stays constant with distance, the threshold for the oblique FM/W instability crosses the strahl bulk velocity at a critical distance $r_{\mathrm{crit}}/r_s > 20$ because $T_{\parallel c}$ continues to decrease with distance. However, the plasma transitions from the low-$\beta_{\parallel c}$ regime into the high-$\beta_{\parallel c}$ regime of the oblique FM/W instability with distance. The transition between both regimes is defined at $\beta_{\parallel c} \approx 0.25$ (Verscharen et al., 2019), which is not crossed at the distances explored in our model (see Fig. 4.6d). If the plasma does not fulfill Eq. (4.70) before it reaches the high-$\beta_{\parallel c}$ regime, we must consider a greater threshold for the oblique FM/W instability as given by Verscharen et al. (2019). The extension of our model to larger heliocentric distances and the comparison of the instability thresholds in these different regimes lie beyond the scope of this work.

Evidence for strahl scattering through the oblique FM/W instability in the near-Sun environment has been recently provided based on PSP data (Halekas et al.,

2021). In a small selection of cases, the observed electron strahl parameters at heliocentric distances $\lesssim 50 r_s$ cross the threshold for the oblique FM/W instability. However, in agreement with our results, the majority of the parameter combinations are found to be stable with respect to this instability. This leaves the question open as to what process regulates the electron heat flux in the inner heliosphere. Our results suggest that the average strahl evolution within $r/r_s = 20$ from the Sun is dominated by the kinetic effects included in our transport equation rather than wave–particle processes such as instabilities and resonant dissipation. However, wave–particle interactions are a possible explanation for the slight discrepancy between our model output and the PSP observations in terms of $T_{\parallel c}$.

Chapter 5

The Stability of the Electron Strahl against the Oblique Fast-magnetosonic/Whistler Instability in the Inner Heliosphere

In this chapter, we confirm the stability of the electron strahl in the solar wind depending on heliocentric distance. Based on data from PSP and Helios, we compare the measured strahl properties with the analytical thresholds for the oblique FM/W instability in the low- and high-$\beta_{\|c}$ regimes. The PSP data was provided by Joel Baby Abraham, and the Helios data was provided by Laura Bercic. This chapter is based on the published paper "The Stability of the Electron Strahl against the Oblique Fast-magnetosonic/Whistler Instability in the Inner Heliosphere", Jeong et al. (2022a).

5.1 Introduction

The strahl scattering mechanism in the heliosphere is very important for the definition of the electron heat flux; however, its nature is still unknown. Electron measurements in the solar wind provide evidence that whistler waves exchange energy with the electron strahl, which makes them a candidate to explain the scattering of the strahl into the halo population (Pagel et al., 2007; Lacombe et al., 2014; Gra-

ham et al., 2017). Linear theory suggests that the FM/W wave propagating in the anti-Sunward direction with an oblique wavevector with respect to the background magnetic field can be driven unstable by the strahl through the anomalous cyclotron resonance and scatter strahl electrons in velocity space (Vasko et al., 2019; Verscharen et al., 2019). This strahl-driven instability has recently received a significant amount of attention in the literature as a local strahl scattering mechanism. Linear and quasi-linear theories as well as numerical particle-in-cell (PIC) simulations support this picture (López et al., 2020; Jeong et al., 2020; Micera et al., 2020, 2021; Sun et al., 2021).

As the solar wind begins its journey in the corona where Coulomb collisions are more frequent than in the heliosphere, we anticipate that the core–halo–strahl configuration develops outside the corona. It is unknown at which heliocentric distance the local strahl scattering sets in. Based on a linear stability analysis, Horaites et al. (2018a) and Schroeder et al. (2021) argue against the action of a strahl-driven instability in the inner heliosphere at all. Parker Solar Probe (PSP) data from encounters 4 and 5 suggest that the strahl, at times, drives the oblique FM/W wave unstable at heliocentric distances below $54r_s$ (Halekas et al., 2021), where r_s is the solar radius. A kinetic expansion model for the solar-wind electrons suggests, however, that the oblique FM/W instability is unlikely to occur regularly and scatter the electron strahl at heliocentric distances below $20r_s$ (Jeong et al., 2022b). Moreover, whistler waves are barely detected by PSP within $28r_s$ (Cattell et al., 2021), supporting the notion that strahl scattering by the oblique FM/W instability is not a universal – or even common – process in the inner heliosphere.

In the present chapter, we use the analytical thresholds for the oblique FM/W instability derived by Verscharen et al. (2019) to investigate the stability of the electron strahl in the inner heliosphere. By using PSP and Helios data, we quantify the analytical thresholds as functions of heliocentric distance. Our results show that, on average, the electron strahl is not scattered by the oblique FM/W instability in the inner heliosphere.

5.2 Method

5.2.1 Thresholds for the Oblique FM/W Instability

To analyse the strahl scattering through the oblique FM/W instability, we evaluate the analytical thresholds in the low- and high-$\beta_{\parallel c}$ regimes provided by Verscharen et al. (2019). These analytical equations have been tested against numerical solutions for the thresholds of the oblique FM/W instability from linear hot-plasma theory. The transition between the low-$\beta_{\parallel c}$ and high-$\beta_{\parallel c}$ regimes occurs at

$$\beta_{\parallel c} \approx 0.25, \tag{5.1}$$

where $\beta_{\parallel j} \equiv 8\pi n_j k_B T_{\parallel j}/|\mathbf{B}_0|^2$. The subscripts e, c and s indicate quantities related to the total electrons, the core and the strahl, respectively. The plasma crosses the analytical threshold of the oblique FM/W instability in the low-$\beta_{\parallel c}$ regime if

$$U_s \gtrsim 3v_{\parallel th,c}, \tag{5.2}$$

where $v_{\parallel th,c} = \sqrt{2k_B T_{\parallel c}/m_e}$ is the core parallel thermal speed and U_s is the strahl bulk velocity. The plasma crosses the analytical threshold of the oblique FM/W instability in the high-$\beta_{\parallel c}$ regime if

$$U_s \gtrsim \left[2\frac{n_s}{n_c}\sqrt{\frac{T_{\parallel s}}{T_{\parallel c}}}v_{Ae}^2 v_{\parallel th,c}^2 \frac{(1+\cos\theta_0)}{(1-\cos\theta_0)\cos\theta_0}\right]^{0.25}, \tag{5.3}$$

where $v_{Ae} = |\mathbf{B}_0|/\sqrt{4\pi n_e m_e}$, and θ_0 is the angle between wavevector $\mathbf{k}_0$ and $\mathbf{B}_0$[1].

5.2.2 Data Analysis of PSP and Helios Data

We base our data analysis on the PSP dataset created by Abraham et al. (2021). Our PSP data range from heliocentric distances between $25r_s$ and $90r_s$. This dataset uses fits to the observed level-3 electron VDFs provided by the Solar Wind Electron Alphas and Protons (SWEAP) instrument suite (Kasper et al., 2016; Whittlesey et al.,

[1] The original derivation of the instability thresholds by Verscharen et al. (2019) assumes isotropic electrons. However, it is straight-forward to extend this framework to anisotropic electrons, in which case we retrieve Eqs. (5.2) and (5.3).

2020) on board PSP. SWEAP consists of two electrostatic analysers, SPAN A and B, which combined measure electrons arriving from across almost the full sky using orthogonally positioned $120^\circ \times 240^\circ$ fields of view, over an energy range from 2 eV to 1793 eV during our measurement intervals. We fit the VDFs in the magnetic-field-aligned velocity frame and ignore any data points below 30 eV to avoid the inclusion of secondary electrons. The analysis method fits a bi-Maxwellian distribution to the core, a bi-κ distribution to the halo and a drifting bi-Maxwellian distribution to the strahl. We only allow the strahl to drift in the parallel direction to the magnetic field.

We base our data analysis on the Helios dataset created by Berčič et al. (2019). On Helios 1 and 2 (Rosenbauer et al., 1981; Pilipp et al., 1987a), electrons were measured by the electron particle instrument I2, part of the E1 Plasma Experiment. Our Helios data ranges from heliocentric distances between $62r_s$ and $210r_s$. A narrow instrument aperture ($19^\circ \times 2^\circ$) spins with the spacecraft and covers a full range of 360° in azimuth, providing two-dimensional electron VDFs. For context, we also use proton density and velocity as well as magnetic field measurements as described by Berčič et al. (2019) in Section 3. We analyse the electron VDFs in the magnetic-field-aligned frame, in which the solar wind protons have zero bulk velocity. We model the distributions with a sum of a bi-Maxwellian distribution representing the core, a bi-κ distribution representing the halo, and a bi-Maxwellian distribution representing the strahl. We only allow the core and the strahl to have drift velocities in the direction parallel to magnetic field. We discard all VDFs for which the fit results for the density of the halo or the strahl is greater than the density of the core.

5.3 Results

5.3.1 Fit Parameters from PSP and Helios

We bin the fitted data from both PSP and Helios into 50 radial-distance bins of equal width. We first separate our PSP and Helios data into the low-$\beta_{\parallel c}$ regime and high-$\beta_{\parallel c}$ regime according to Eq. (5.1). We show the profiles of $T_{\parallel c}$, $T_{\parallel s}$, $|\mathbf{B}_0|$, n_c/n_e,

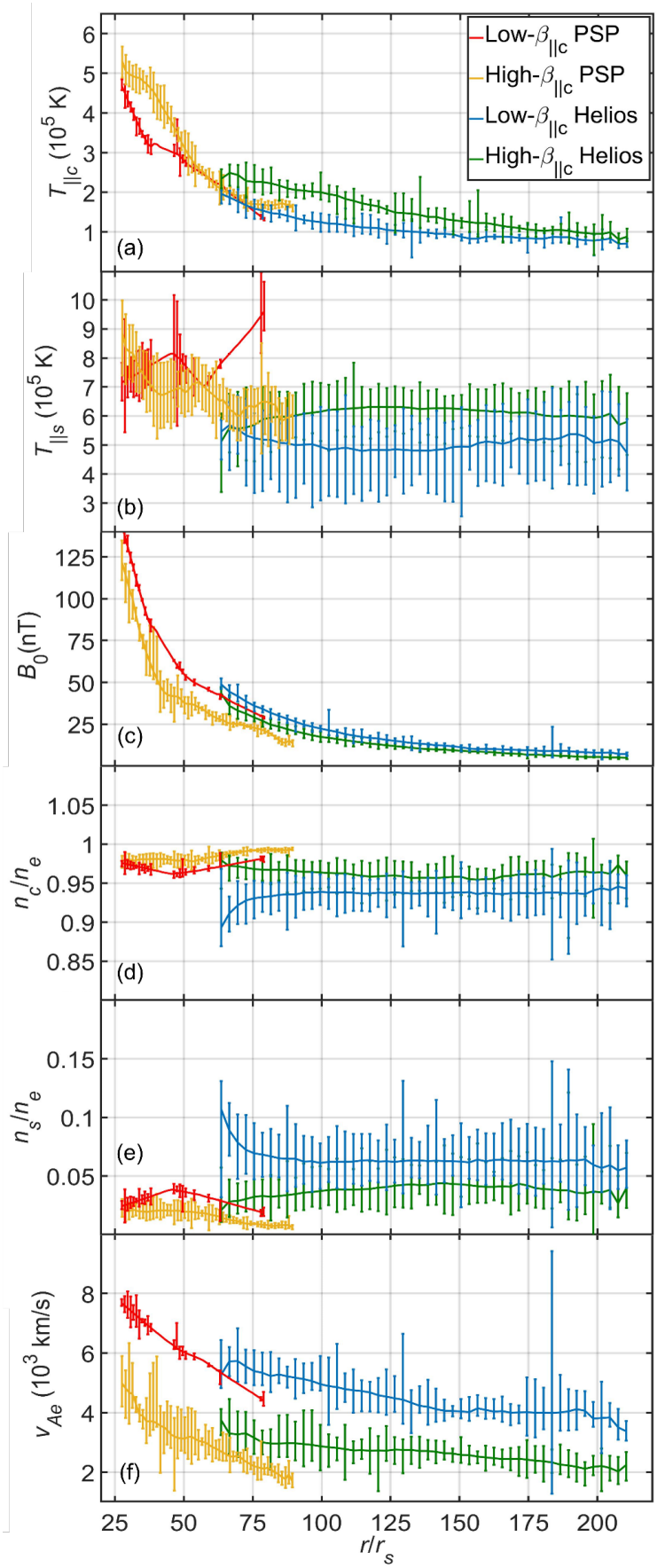

Figure 5.1: Radial profiles of $T_{||c}$, $T_{||s}$, $|\mathbf{B}_0|$, n_c/n_e, n_s/n_e and v_{Ae} in our PSP and Helios datasets, separated between the low-$\beta_{||c}$ and the high-$\beta_{||c}$ regimes.

n_s/n_e and v_{Ae}, which all appear on the right-hand sides of Eqs. (5.2) and (5.3), as functions of heliocentric distance in Fig. 5.1. The logarithmic profiles of Fig. 5.1 are shown in Fig. C.3. The red and blue lines correspond to the parameters in the low-$\beta_{\|c}$ regime while the yellow and green lines correspond to the parameters in the high-$\beta_{\|c}$ regime from PSP and Helios.

PSP predominately samples streams of slow solar wind while the Helios dataset includes a broader variety of solar wind. Therefore, the PSP and Helios datasets do not connect exactly, especially in terms of $T_{\|s}$, n_c/n_e and n_s/n_e in the low-$\beta_{\|c}$ cases.

For our evaluation of the instability thresholds as functions of heliocentric distance, we apply the binned mean profiles of the parameters shown in Fig. 5.1 to Eqs. (5.2) and (5.3).

5.3.2 Threshold in the Low-$\beta_{\|c}$ Regime

In Fig. 5.2, the blue (PSP) and red (Helios) lines show the profiles of the right-hand side of Eq. (5.2), and the yellow (PSP) and green (Helios) lines show the measured profiles of U_s. The logarithmic profile of Fig. 5.2 is shown in Fig. C.1. The strahl

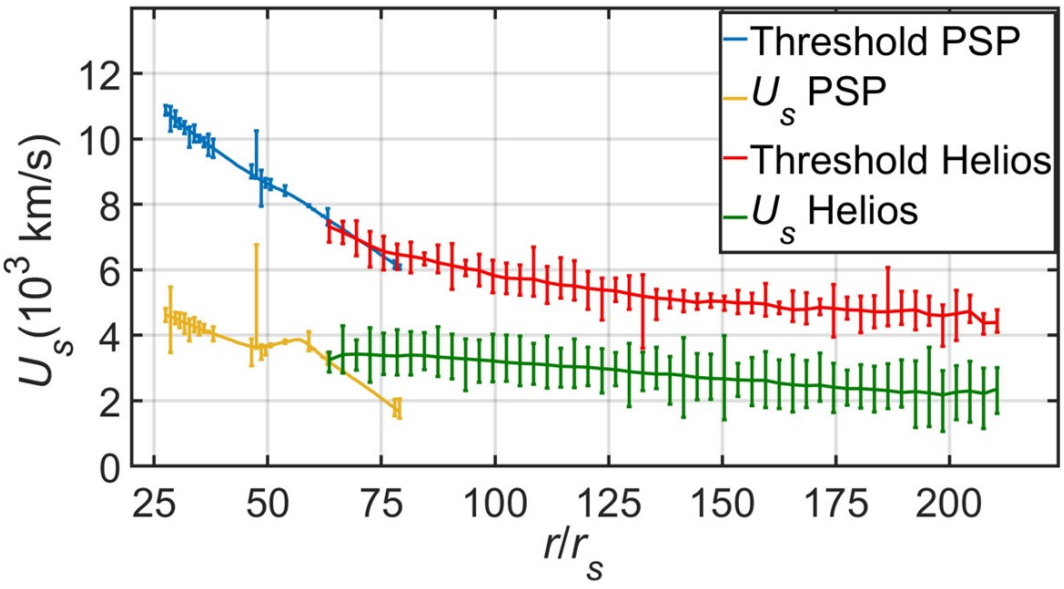

Figure 5.2: Profiles of the low-$\beta_{\|c}$ threshold of the oblique FM/W instability from Eq. (5.2) and U_s as functions of heliocentric distance. All PSP and Helios data underlying this figure have $\beta_{\|c} < 0.25$.

bulk velocity does not cross the low-$\beta_{\|c}$ threshold in the shown range of heliocentric

distances on average and, thus, does not fulfill Eq. (5.2). The low-$\beta_{\|c}$ threshold and U_s decrease quasi-monotonously. Near the Sun, the difference between the low-$\beta_{\|c}$ threshold and U_s decreases with heliocentric distance. However, beyond about $80r_s$ from the Sun, the difference is nearly constant. The error bars of the low-$\beta_{\|c}$ threshold and U_s do not overlap with each other in the shown range of heliocentric distances.

5.3.3 Threshold in the High-$\beta_{\|c}$ Regime

Previous studies of the oblique FM/W instability by Vasko et al. (2019), Verscharen et al. (2019), López et al. (2020), Jeong et al. (2020), Micera et al. (2020), Micera et al. (2021), and Sun et al. (2021) suggest that the angle θ_0 in Eq. (5.3) typically ranges from $\theta_0 = 55°$ to $65°$. Eq. (5.3) does not significantly depend on θ_0 in this range compared to its much stronger dependence on $T_{\|c}$, $T_{\|s}$, n_c, n_s and v_{Ae}. Therefore, we use a representative value of $\theta_0 = 60°$.

In Fig. 5.3, the blue (PSP) and red (Helios) lines show the profiles of the right-hand side of Eq. (5.3), and the yellow (PSP) and green (Helios) lines show the measured profile of U_s. The logarithmic profile of Fig. 5.3 is shown in Fig. C.2. The strahl bulk velocity does not cross the high-$\beta_{\|c}$ threshold in the shown range

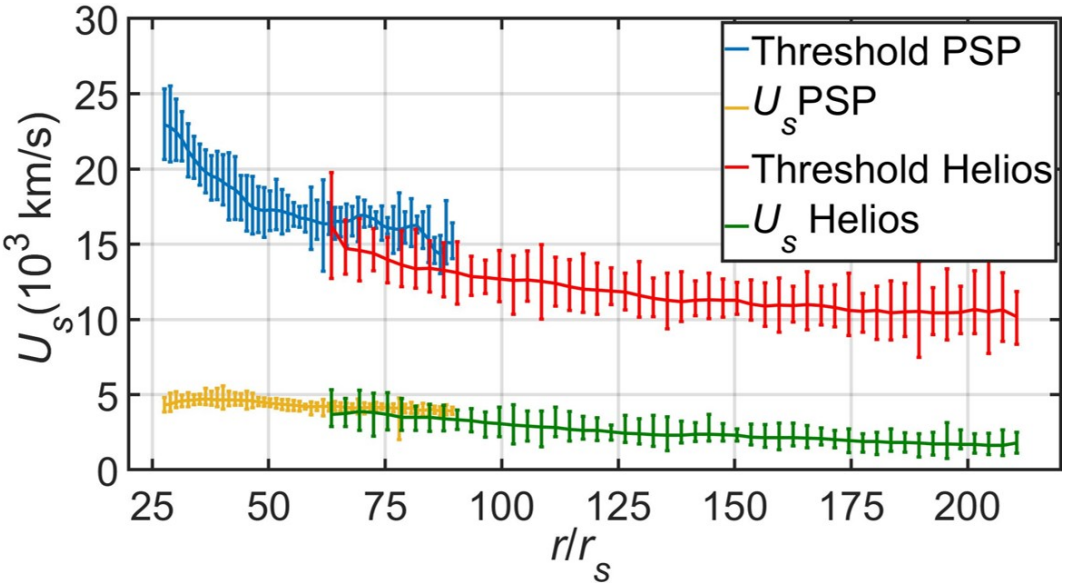

Figure 5.3: Profiles of the high-$\beta_{\|c}$ threshold of the oblique FM/W instability from Eq. (5.3) and U_s as functions of heliocentric distance. All PSP and Helios data underlying this figure have $\beta_{\|c} > 0.25$.

of heliocentric distances on average and, thus, does not fulfill Eq. (5.3). The high-$\beta_{\|c}$ threshold and U_s quasi-monotonously decrease at all explored heliocentric distances. Like in the low-$\beta_{\|c}$ case, near the Sun, the difference between the high-$\beta_{\|c}$ threshold and U_s decreases with heliocentric distance. However, beyond about $80r_s$ from the Sun, the difference is approximately constant. The error bars of the high-$\beta_{\|c}$ threshold and U_s do not overlap with each other at all explored heliocentric distances.

5.4 Discussion

Our results show that Eqs. (5.2) and (5.3) are, for plasma with the observed average radial profiles, not satisfied at heliocentric distances between $25r_s$ and $210r_s$. In Figs. 5.2 and 5.3, the low- and high-$\beta_{\|c}$ thresholds are always greater than U_s. For both the low-$\beta_{\|c}$ and for the high-$\beta_{\|c}$ case, the difference between the threshold and U_s decreases with heliocentric distance near the Sun as predicted by Jeong et al. (2022b) in section 4.4.4. However, beyond a heliocentric distance of $\sim 80r_s$, the difference between the thresholds and U_s is nearly constant. Assuming that our PSP and Helios data are representative and that our Eqs. (5.2) and (5.3) reflect the thresholds accurately, our findings suggest that the strahl is not scattered by the oblique FM/W instability in the inner heliosphere, in agreement with the arguments presented by Horaites et al. (2018a) and Schroeder et al. (2021).

According to quasi-linear theory and particle-in-cell simulations (Jeong et al., 2020; Micera et al., 2020, 2021), the oblique FM/W instability, if excited, scatters the electron strahl efficiently on a timescale shorter than one second in the inner heliosphere. This rapid action of the instability and the radial decrease of the thresholds suggest that the measured U_s would closely follow the threshold of marginal stability at all distances beyond the critical distance r_{crit}, at which the threshold is crossed for the first time. However, neither Fig. 5.2 nor Fig. 5.3 suggest the existence of r_{crit} at heliocentric distances less than 1 au.

The derivation of Eqs. (5.2) and (5.3) by Verscharen et al. (2019) is based on the assumption that the oblique FM/W instability is most efficiently driven by elec-

trons with $v_{\parallel} = U_s$. However, according to the predictions by quasi-linear theory and PIC simulations (Jeong et al., 2020; Micera et al., 2020, 2021), strahl scattering by the oblique FM/W instability most efficiently occurs in the $v_{\parallel}$-range $\gtrsim U_s$. For example, Jeong et al. (2020) in section 3.3 show that the oblique FM/W instability in the high-$\beta_{\parallel c}$ regime is most efficiently driven by electrons with $v_{\parallel} \approx 2U_s$. Applying this argument in the derivation of Eqs. (5.2) and (5.3), we find a threshold for the high-$\beta_{\parallel c}$ case that is lower by a factor of two than given in Fig. 5.3. Such a modification would lead to a small difference between the two curves shown in Fig. 5.3. If we adjusted the analytical thresholds by a constant factor greater than 2, the discovered constant difference between the thresholds and U_s at $r \gtrsim 80r_s$ would be consistent with the limitation of U_s through the oblique FM/W instability with $r_{\mathrm{crit}} \approx 80r_s$.

The uncertainties of the analytical instability thresholds can be circumvented by calculating the stability of individually measured electron VDFs with numerical tools like the ALPS (Verscharen and Chandran, 2018) or LEOPARD codes (Astfalk and Jenko, 2017). These numerical tools are able to calculate the full hot-plasma dispersion relation based on our PSP and Helios data without assuming a bi-Maxwellian shape of the electron VDF. In addition, it would be worthwhile to investigate the occurrence of oblique FM/W waves as a result of the oblique FM/W instability. This method would also allow for an independent determination of r_{crit} and thus an independent determination of a potential correction factor to our analytical instability thresholds.

Chapter 6

Numerical Analysis for Kinetic Diffusion Equations

In this chapter, we develop our mathematical approach based on the Crank–Nicolson scheme to numerically solve the kinetic diffusion equations used in the previous chapters, such as the quasi-linear diffusion equation, the Fokker–Planck operator and the kinetic transport equations. This chapter is based on the appendix of the submitted paper "The Kinetic Expansion of Solar-Wind Electrons: Transport Theory and Predictions for the very Inner Heliosphere", Jeong et al. (2021) and the published paper "A Quasi-linear Diffusion Model for Resonant Wave–Particle Instability in Homogeneous Plasma", Jeong et al. (2020).

6.1 Introduction of Crank-Nicolson Scheme

For the numerical evaluation of our theoretical description, a rigorous numerical analysis is necessary. Because of its reliable stability, the Crank–Nicolson scheme has been used previously to solve the diffusion equations in a variety of fields (Khazanov et al., 2002; Albert, 2004; Brügmann et al., 2004; Yang et al., 2009; Klein and Chandran, 2016; Taran et al., 2019). The Crank–Nicolson scheme is based on the trapezoidal rule (Iserles, 2008):

$$\begin{aligned} y(t) &= y(t_0) + \int_{t_0}^{t} f(\tau) d\tau \\ &\approx y(t_0) + (t - t_0) \frac{1}{2} \left[f(t) + f(t_0) \right] \end{aligned} \tag{6.1}$$

where $f(t)$ is an arbitrary function and t_0 is the reference time. The Crank–Nicolson scheme is then given as

$$\frac{y(t_{n+1}) - y(t_n)}{t_{n+1} - t_n} = \frac{1}{2}\left[f(t_{n+1}) + f(t_n)\right] \tag{6.2}$$

where t_{n+1} and t_n are adjacent time steps in a discrete time space. Eq. (6.2) is an implicit method of order 2 in time. The implicit method means that a system of algebraic equations needs to be solved in order to achieve the desired solution $f(t_{n+1})$. However, depending on the complexity and dimension of a given diffusion equation, solving a system of algebraic equations can be simple or extremely difficult. Most approaches based on Crank–Nicolson schemes neglect the off-diagonal derivatives in the diffusion equation such as $\partial^2/\partial v_\parallel \partial v_\perp$ because the approach solving a diffusion equation with those terms based on the Crank–Nicolson scheme has not existed previously. However, the off-diagonal derivative terms are important in our case (see the quasi-linear diffusion equation Eq. (3.6), Fokker–Planck operator Eq. (A.44) and kinetic transport equation Eq. (4.37)).

In this chapter, we provide a mathematical approach using a multi-layer tridiagonal matrix, which is able to solve any diffusion equation with any dimension based on the Crank–Nicolson scheme. Instead of explaining this approach in a completely general case, we explain our mathematical approach with the diffusion equations which appear in the previous chapters. In section 6.2, we numerically solve the full two-dimensional quasi-linear diffusion equation, Eq. (3.6). In section 6.3, we numerically solve the full two-dimensional Fokker–Planck operator, Eq. (A.44). In section 6.4, we numerically solve the full three-dimensional kinetic transport equation in two different ways.

6.2 Numerical Analysis for Quasi-Linear Diffusion Equation

Eq. (3.6) is a second-order two-dimensional diffusion equation. We divide velocity space into $N_v \times N_v$ steps with equal step sizes of Δv by defining the outer boundaries

of velocity space as $\pm v_{\perp\max}$ and $\pm v_{\parallel\max}$. The $v_\perp$-index M and the $v_\parallel$-index N both step through 1, 2, 3, ..., N_v. We define the discrete velocity coordinates as $v_{\perp M} \equiv -v_{\perp\max} + (M-1)\Delta v$ and $v_{\parallel N} \equiv -v_{\parallel\max} + (N-1)\Delta v$. We note that this definition introduces negative $v_\perp$-values that, although they simplify our numerical analysis, we neglect in our computational results. We divide the time t with equal step sizes of Δt and the t-index T steps through $1, 2, 3, \cdots$. We define the discrete time as $t^T \equiv (T-1)\Delta t$. We then define the discrete two-dimensional VDF as $f^T_{M,N} \equiv f_j(v_{\perp M}, v_{\parallel N}, t^T)$. For the discretization of the velocity derivatives, we adopt the two-point central difference operator (Gilat and Subramaniam, 2011)

$$\frac{\partial f_j(v_{\perp M}, v_{\parallel N}, t^T)}{\partial v_\perp} \approx \frac{f^T_{M+1,N} - f^T_{M-1,N}}{2\Delta v}, \tag{6.3}$$

and

$$\frac{\partial f_j(v_{\perp M}, v_{\parallel N}, t^T)}{\partial v_\parallel} \approx \frac{f^T_{M,N+1} - f^T_{M,N-1}}{2\Delta v}. \tag{6.4}$$

For the discretization of the time derivative, we adopt the forward difference operator

$$\frac{\partial f_j(v_{\perp M}, v_{\parallel N}, t^T)}{\partial t} \approx \frac{f^{T+1}_{M,N} - f^T_{M,N}}{\Delta t}. \tag{6.5}$$

By using Eqs. (6.4) and (6.3), we discretize the right-hand side of Eq. (3.6) and express it as $(\partial f/\partial t)^T_{M,N}$

$$\begin{aligned}\left(\frac{\partial f}{\partial t}\right)^T_{M,N} \equiv \sum_{n=-\infty}^{\infty} \int \Bigg[&\left(1 - \frac{k_\parallel v_{\parallel N}}{\omega_{k0} + v_{g0}(k_\parallel - k_{\parallel 0})}\right) \\ &\times \frac{1}{v_{\perp M}} \frac{D^n_{M+1,N}[\hat{G}f]^T_{M+1,N} - D^n_{M-1,N}[\hat{G}f]^T_{M-1,N}}{2\Delta v} \\ &+ \frac{k_\parallel}{\omega_{k0} + v_{g0}(k_\parallel - k_{\parallel 0})} \frac{D^n_{M,N+1}[\hat{G}f]^T_{M,N+1} - D^n_{M,N-1}[\hat{G}f]^T_{M,N-1}}{2\Delta v} \Bigg] d^3\mathbf{k},\end{aligned} \tag{6.6}$$

where

$$[\hat{G}f]^T_{M,N} \equiv \left(1 - \frac{k_\parallel v_{\parallel N}}{\omega_{k0} + v_{g0}(k_\parallel - k_{\parallel 0})}\right) \frac{1}{v_{\perp M}} \frac{f^T_{M+1,N} - f^T_{M-1,N}}{2\Delta v} + \frac{k_\parallel}{\omega_{k0} + v_{g0}(k_\parallel - k_{\parallel 0})} \frac{f^T_{M,N+1} - f^T_{M,N-1}}{2\Delta v}, \tag{6.7}$$

and

$$D^n_{M,N} \equiv D^n_j \Big|_{\substack{v_\perp = v_{\perp M} \\ v_\parallel = v_{\parallel N}}}. \tag{6.8}$$

According to the Crank-Nicolson scheme Eq. (6.2), the full discretization of Eq. (3.6) in its time and velocity derivatives is then given by

$$f^{T+1}_{M,N} - \frac{\Delta t}{2}\left(\frac{\partial f}{\partial t}\right)^{T+1}_{M,N} = f^T_{M,N} + \frac{\Delta t}{2}\left(\frac{\partial f}{\partial t}\right)^{T}_{M,N}. \tag{6.9}$$

By using Eqs. (6.6)-(6.8) and resolving the δ-functions in $D^n_{M\pm1,N}$ and $D^n_{M,N\pm1}$ through the $k_\parallel$-integral, we rewrite Eq. (6.9) as

$$
\begin{aligned}
f^{T+1}_{M,N} - \sum_{n=-\infty}^{\infty} \Bigg\{ & \frac{\mu_{vv}}{8} P^n_{M,N} \widetilde{D}^n_{M+1,N} \\
& \times \left[P^n_{M+1,N} \left(f^{T+1}_{M+2,N} - f^{T+1}_{M,N} \right) + Q^n_N \left(f^{T+1}_{M+1,N+1} - f^{T+1}_{M+1,N-1} \right) \right] \\
& - \frac{\mu_{vv}}{8} P^n_{M,N} \widetilde{D}^n_{M-1,N} \\
& \times \left[P^n_{M-1,N} \left(f^{T+1}_{M,N} - f^{T+1}_{M-2,N} \right) + Q^n_N \left(f^{T+1}_{M-1,N+1} - f^{T+1}_{M-1,N-1} \right) \right] \\
& + \frac{\mu_{vv}}{8} Q^n_{N+1} \widetilde{D}^n_{M,N+1} \\
& \times \left[P^n_{M,N+1} \left(f^{T+1}_{M+1,N+1} - f^{T+1}_{M-1,N+1} \right) + Q^n_{N+1} \left(f^{T+1}_{M,N+2} - f^{T+1}_{M,N} \right) \right] \\
& - \frac{\mu_{vv}}{8} Q^n_{N-1} \widetilde{D}^n_{M,N-1} \\
& \times \left[P^n_{M,N-1} \left(f^{T+1}_{M+1,N-1} - f^{T+1}_{M-1,N-1} \right) + Q^n_{N-1} \left(f^{T+1}_{M,N} - f^{T+1}_{M,N-2} \right) \right] \Bigg\}
\end{aligned}
$$

$$
= \tag{6.10}
$$

$$
\begin{aligned}
f^{T}_{M,N} + \sum_{n=-\infty}^{\infty} \Bigg\{ & \frac{\mu_{vv}}{8} P^n_{M,N} \widetilde{D}^n_{M+1,N} \\
& \times \left[P^n_{M+1,N} \left(f^{T}_{M+2,N} - f^{T}_{M,N} \right) + Q^n_N \left(f^{T}_{M+1,N+1} - f^{T}_{M+1,N-1} \right) \right] \\
& - \frac{\mu_{vv}}{8} P^n_{M,N} \widetilde{D}^n_{M-1,N} \\
& \times \left[P^n_{M-1,N} \left(f^{T}_{M,N} - f^{T}_{M-2,N} \right) + Q^n_N \left(f^{T}_{M-1,N+1} - f^{T}_{M-1,N-1} \right) \right] \\
& + \frac{\mu_{vv}}{8} Q^n_{N+1} \widetilde{D}^n_{M,N+1} \\
& \times \left[P^n_{M,N+1} \left(f^{T}_{M+1,N+1} - f^{T}_{M-1,N+1} \right) + Q^n_{N+1} \left(f^{T}_{M,N+2} - f^{T}_{M,N} \right) \right] \\
& - \frac{\mu_{vv}}{8} Q^n_{N-1} \widetilde{D}^n_{M,N-1} \\
& \times \left[P^n_{M,N-1} \left(f^{T}_{M+1,N-1} - f^{T}_{M-1,N-1} \right) + Q^n_{N-1} \left(f^{T}_{M,N} - f^{T}_{M,N-2} \right) \right] \Bigg\},
\end{aligned}
$$

where

$$
P^n_{M,N} \equiv \frac{n\Omega_j [v_{\parallel N} - v_{g0}]}{[(\omega_{k0} - k_{\parallel 0} v_{g0}) v_{\parallel N} - n\Omega_j v_{g0}] v_{\perp M}}, \tag{6.11}
$$

$$Q_N^n \equiv \frac{\omega_{k0} - k_{\|0} v_{g0} - n\Omega_j}{(\omega_{k0} - k_{\|0} v_{g0}) v_{\|N} - n\Omega_j v_{g0}}, \tag{6.12}$$

$$\widetilde{D}_{M,N}^n \equiv \widetilde{D}_j^n \Big|_{\substack{v_\perp = v_{\perp M} \\ v_\| = v_{\|N}}}, \tag{6.13}$$

and $\mu_{vv} \equiv \Delta t / (\Delta v)^2$. Eq. (6.10) is a two-dimensional set of algebraic equations, the solution of which, $f_{M,N}^{T+1}$, for all $v_\perp$- and $v_\|$-indexes describes the VDF at time $T+1$ based on $f_{M,N}^T$ for all $v_\perp$- and $v_\|$-indexes.

In order to transform Eq. (6.10) into a single matrix equation with a tridiagonal matrix, we introduce the concept of a two-layer matrix. On both sides of Eq. (6.10), we group the terms by the same $v_\perp$-index in the VDF and rearrange these groups in increasing order in $v_\perp$-index. In each group, we then rearrange terms in increasing order in $v_\|$-index in the VDF. Then, we have

$$\begin{aligned}
&-\eta_{M,N}^{(1)} f_{M-2,N}^{T+1} - \xi_{M,N}^{(2)} f_{M-1,N-1}^{T+1} + \xi_{M,N}^{(1)} f_{M-1,N+1}^{T+1} - \beta_{M,N}^{(2)} f_{M,N-2}^{T+1} \\
&+\alpha_{M,N}^{(1)} f_{M,N}^{T+1} - \beta_{M,N}^{(1)} f_{M,N+2}^{T+1} + \xi_{M,N}^{(4)} f_{M+1,N-1}^{T+1} - \xi_{M,N}^{(3)} f_{M+1,N+1}^{T+1} - \eta_{M,N}^{(2)} f_{M+2,N}^{T+1} \\
&= \\
&\eta_{M,N}^{(1)} f_{M-2,N}^{T} + \xi_{M,N}^{(2)} f_{M-1,N-1}^{T} - \xi_{M,N}^{(1)} f_{M-1,N+1}^{T} + \beta_{M,N}^{(2)} f_{M,N-2}^{T} \\
&+\alpha_{M,N}^{(2)} f_{M,N}^{T} + \beta_{M,N}^{(1)} f_{M,N+2}^{T} - \xi_{M,N}^{(4)} f_{M+1,N-1}^{T} + \xi_{M,N}^{(3)} f_{M+1,N+1}^{T} + \eta_{M,N}^{(2)} f_{M+2,N}^{T},
\end{aligned} \tag{6.14}$$

where

$$\begin{aligned}
\alpha_{M,N}^{(1)} \equiv 1 + \frac{\mu_{vv}}{8} \sum_{n=-\infty}^{\infty} \Bigg[& \left(P_{M,N}^n P_{M+1,N}^n\right) \widetilde{D}_{M+1,N}^n + \left(P_{M,N}^n P_{M-1,N}^n\right) \widetilde{D}_{M-1,N}^n \\
& + \left(Q_{N+1}^n\right)^2 \widetilde{D}_{M,N+1}^n + \left(Q_{N-1}^n\right)^2 \widetilde{D}_{M,N-1}^n \Bigg],
\end{aligned} \tag{6.15}$$

$$\begin{aligned}
\alpha_{M,N}^{(2)} \equiv 1 - \frac{\mu_{vv}}{8} \sum_{n=-\infty}^{\infty} \Bigg[& \left(P_{M,N}^n P_{M+1,N}^n\right) \widetilde{D}_{M+1,N}^n + \left(P_{M,N}^n P_{M-1,N}^n\right) \widetilde{D}_{M-1,N}^n \\
& + \left(Q_{N+1}^n\right)^2 \widetilde{D}_{M,N+1}^n + \left(Q_{N-1}^n\right)^2 \widetilde{D}_{M,N-1}^n \Bigg],
\end{aligned} \tag{6.16}$$

$$\beta_{M,N}^{(1)} \equiv \frac{\mu_{vv}}{8} \sum_{n=-\infty}^{\infty} \left[\left(Q_{N+1}^n\right)^2 \widetilde{D}_{M,N+1}^n \right], \tag{6.17}$$

$$\beta^{(2)}_{M,N} \equiv \frac{\mu_{vv}}{8} \sum_{n=-\infty}^{\infty} \left[\left(Q^n_{N-1}\right)^2 \widetilde{D}^n_{M,N-1} \right], \tag{6.18}$$

$$\xi^{(1)}_{M,N} \equiv \frac{\mu_{vv}}{8} \sum_{n=-\infty}^{\infty} \left[\left(P^n_{M,N} Q^n_N\right) \widetilde{D}^n_{M-1,N} + \left(P^n_{M,N+1} Q^n_{N+1}\right) \widetilde{D}^n_{M,N+1} \right], \tag{6.19}$$

$$\xi^{(2)}_{M,N} \equiv \frac{\mu_{vv}}{8} \sum_{n=-\infty}^{\infty} \left[\left(P^n_{M,N} Q^n_N\right) \widetilde{D}^n_{M-1,N} + \left(P^n_{M,N-1} Q^n_{N-1}\right) \widetilde{D}^n_{M,N-1} \right], \tag{6.20}$$

$$\xi^{(3)}_{M,N} \equiv \frac{\mu_{vv}}{8} \sum_{n=-\infty}^{\infty} \left[\left(P^n_{M,N} Q^n_N\right) \widetilde{D}^n_{M+1,N} + \left(P^n_{M,N+1} Q^n_{N+1}\right) \widetilde{D}^n_{M,N+1} \right], \tag{6.21}$$

$$\xi^{(4)}_{M,N} \equiv \frac{\mu_{vv}}{8} \sum_{n=-\infty}^{\infty} \left[\left(P^n_{M,N} Q^n_N\right) \widetilde{D}^n_{M+1,N} + \left(P^n_{M,N-1} Q^n_{N-1}\right) \widetilde{D}^n_{M,N-1} \right], \tag{6.22}$$

$$\eta^{(1)}_{M,N} \equiv \frac{\mu_{vv}}{8} \sum_{n=-\infty}^{\infty} \left[\left(P^n_{M,N} P^n_{M-1,N}\right) \widetilde{D}^n_{M-1,N} \right], \tag{6.23}$$

and

$$\eta^{(2)}_{M,N} \equiv \frac{\mu_{vv}}{8} \sum_{n=-\infty}^{\infty} \left[\left(P^n_{M,N} P^n_{M+1,N}\right) \widetilde{D}^n_{M+1,N} \right]. \tag{6.24}$$

All terms in both sides of Eq. (6.14) with a constant $v_\perp$-index account for variations in the $v_\parallel$-space only. Therefore, they can be grouped into a single system of one-dimensional algebraic equations.

We transform all terms with $v_\perp$-index of M in the VDF on both sides of Eq. (6.14) into the tridiagonal matrices $\mathbb{A}^{(1)}_M \mathbb{F}^{T+1}_M$ and $\mathbb{A}^{(2)}_M \mathbb{F}^T_M$, where $\mathbb{F}^T_M \equiv [f^T_{M,1}\, f^T_{M,2}\, f^T_{M,3} \cdots f^T_{M,N_v}]^{\mathbf{T}}_{1\times N_v}$ ($\mathbf{T}$ represents the transpose of a matrix), and

$$\mathbb{A}^{(1)}_M \equiv \begin{bmatrix} \alpha^{(1)}_{M,1} & 0 & -\beta^{(1)}_{M,1} & 0 & 0 & \cdots & 0 \\ 0 & \alpha^{(1)}_{M,2} & 0 & -\beta^{(1)}_{M,2} & 0 & \cdots & 0 \\ -\beta^{(2)}_{M,3} & 0 & \alpha^{(1)}_{M,3} & 0 & -\beta^{(1)}_{M,3} & \cdots & 0 \\ & \vdots & & \ddots & & \vdots & \\ 0 & \cdots & 0 & 0 & -\beta^{(2)}_{M,N_v} & 0 & \alpha^{(1)}_{M,N_v} \end{bmatrix}_{N_v\times N_v}. \tag{6.25}$$

and

$$\mathbb{A}_M^{(2)} \equiv \begin{bmatrix} \alpha_{M,1}^{(2)} & 0 & -\beta_{M,1}^{(1)} & 0 & 0 & \cdots & 0 \\ 0 & \alpha_{M,2}^{(2)} & 0 & -\beta_{M,2}^{(1)} & 0 & \cdots & 0 \\ -\beta_{M,3}^{(2)} & 0 & \alpha_{M,3}^{(2)} & 0 & -\beta_{M,3}^{(1)} & \cdots & 0 \\ & \vdots & & \ddots & & \vdots & \\ 0 & \cdots & 0 & 0 & -\beta_{M,N_v}^{(2)} & 0 & \alpha_{M,N_v}^{(2)} \end{bmatrix}_{N_v \times N_v} . \tag{6.26}$$

We transform all terms with $v_\perp$-index of $M-1$ in the VDF on both sides of Eq. (6.14) into the tridiagonal matrices $\mathbb{B}_M^{(1)}\mathbb{F}_{M-1}^{T+1}$ and $-\mathbb{B}_M^{(1)}\mathbb{F}_{M-1}^{T}$, where

$$\mathbb{B}_M^{(1)} \equiv \begin{bmatrix} 0 & \xi_{M,1}^{(1)} & 0 & \cdots & 0 \\ -\xi_{M,2}^{(2)} & 0 & \xi_{M,2}^{(1)} & \cdots & 0 \\ & \vdots & \ddots & & \vdots \\ 0 & \cdots & 0 & -\xi_{M,N_v}^{(2)} & 0 \end{bmatrix}_{N_v \times N_v} . \tag{6.27}$$

We transform all terms with $v_\perp$-index of $M+1$ in the VDF on both sides of Eq. (6.14) into the tridiagonal matrices $\mathbb{B}_M^{(2)}\mathbb{F}_{M+1}^{T+1}$ and $-\mathbb{B}_M^{(2)}\mathbb{F}_{M+1}^{T}$, where

$$\mathbb{B}_M^{(2)} \equiv \begin{bmatrix} 0 & -\xi_{M,1}^{(3)} & 0 & \cdots & 0 \\ \xi_{M,2}^{(4)} & 0 & -\xi_{M,2}^{(3)} & \cdots & 0 \\ & \vdots & \ddots & & \vdots \\ 0 & \cdots & 0 & \xi_{M,N_v}^{(4)} & 0 \end{bmatrix}_{N_v \times N_v} . \tag{6.28}$$

We transform all terms with $v_\perp$-index of $M-2$ in the VDF on both sides of Eq. (6.14) into the tridiagonal matrices $\mathbb{C}_M^{(1)}\mathbb{F}_{M-2}^{T+1}$ and $-\mathbb{C}_M^{(1)}\mathbb{F}_{M-2}^{T}$, where

$$\mathbb{C}_M^{(1)} \equiv \begin{bmatrix} -\eta_{M,1}^{(1)} & 0 & \cdots & 0 \\ 0 & -\eta_{M,2}^{(1)} & \cdots & 0 \\ \vdots & & \ddots & \vdots \\ 0 & \cdots & 0 & -\eta_{M,N_v}^{(1)} \end{bmatrix}_{N_v \times N_v} . \tag{6.29}$$

Lastly, we transform all terms with $v_\perp$-index of $M+2$ in the VDF on both sides of

Eq. (6.14) into the tridiagonal matrices $\mathbb{C}_M^{(2)}\mathbb{F}_{M+2}^{T+1}$ and $-\mathbb{C}_M^{(2)}\mathbb{F}_{M+2}^{T}$, where

$$\mathbb{C}_M^{(2)} \equiv \begin{bmatrix} -\eta_{M,1}^{(2)} & 0 & \cdots & 0 \\ 0 & -\eta_{M,2}^{(2)} & \cdots & 0 \\ \vdots & & \ddots & \vdots \\ 0 & \cdots & 0 & -\eta_{M,N_v}^{(2)} \end{bmatrix}_{N_v \times N_v} . \tag{6.30}$$

This strategy allows us to express Eq. (6.14) as a single system of one-dimensional algebraic equations

$$\begin{aligned} &\mathbb{C}_M^{(1)}\mathbb{F}_{M-2}^{T+1} + \mathbb{B}_M^{(1)}\mathbb{F}_{M-1}^{T+1} + \mathbb{A}_M^{(1)}\mathbb{F}_M^{T+1} + \mathbb{B}_M^{(2)}\mathbb{F}_{M+1}^{T+1} + \mathbb{C}_M^{(2)}\mathbb{F}_{M+2}^{T+1} \\ &= -\mathbb{C}_M^{(1)}\mathbb{F}_{M-2}^{T} - \mathbb{B}_M^{(1)}\mathbb{F}_{M-1}^{T} + \mathbb{A}_M^{(2)}\mathbb{F}_M^{T} - \mathbb{B}_M^{(2)}\mathbb{F}_{M+1}^{T} - \mathbb{C}_M^{(2)}\mathbb{F}_{M+2}^{T}. \end{aligned} \tag{6.31}$$

Eq. (6.31) only describes the VDF evolution in the $v_\perp$-space. However, each matrix term itself includes the VDF evolution in the $v_\parallel$-space. We transform Eq. (6.31) into a single tridiagonal matrix

$$\mathbf{E}_{QLD}^{(1)}\mathbf{F}^{T+1} = \mathbf{E}_{QLD}^{(2)}\mathbf{F}^{T} \tag{6.32}$$

where $\mathbf{F}^T \equiv [\mathbb{F}_1^T\ \mathbb{F}_2^T\ \mathbb{F}_3^T\ \cdots\ \mathbb{F}_{N_v}^T]^{\mathbf{T}}_{1\times(N_v)^2}$,

$$\mathbf{E}_{QLD}^{(1)} \equiv \begin{bmatrix} \mathbb{A}_1^{(1)} & \mathbb{B}_1^{(2)} & \mathbb{C}_1^{(2)} & 0 & 0 & \cdots & 0 \\ \mathbb{B}_2^{(1)} & \mathbb{A}_2^{(1)} & \mathbb{B}_2^{(2)} & \mathbb{C}_2^{(2)} & 0 & \cdots & 0 \\ \mathbb{C}_3^{(1)} & \mathbb{B}_3^{(1)} & \mathbb{A}_3^{(1)} & \mathbb{B}_3^{(2)} & \mathbb{C}_3^{(2)} & \cdots & 0 \\ & \vdots & & \ddots & & \vdots & \\ 0 & \cdots & 0 & 0 & \mathbb{C}_{N_v}^{(1)} & \mathbb{B}_{N_v}^{(1)} & \mathbb{A}_{N_v}^{(1)} \end{bmatrix}_{N_v^2 \times N_v^2} , \tag{6.33}$$

and

$$\mathbf{E}^{(2)}_{QLD} \equiv \begin{bmatrix} \mathbb{A}^{(2)}_1 & -\mathbb{B}^{(2)}_1 & -\mathbb{C}^{(2)}_1 & 0 & 0 & \cdots & 0 \\ -\mathbb{B}^{(1)}_2 & \mathbb{A}^{(2)}_2 & -\mathbb{B}^{(2)}_2 & -\mathbb{C}^{(2)}_2 & 0 & \cdots & 0 \\ -\mathbb{C}^{(1)}_3 & -\mathbb{B}^{(1)}_3 & \mathbb{A}^{(2)}_3 & -\mathbb{B}^{(2)}_3 & -\mathbb{C}^{(2)}_3 & \cdots & 0 \\ & \vdots & & \ddots & & \vdots & \\ 0 & \cdots & 0 & 0 & -\mathbb{C}^{(1)}_{N_v} & -\mathbb{B}^{(1)}_{N_v} & \mathbb{A}^{(2)}_{N_v} \end{bmatrix}_{N_v^2 \times N_v^2} . \quad (6.34)$$

Eq. (6.32) is in the form of a two-layer matrix, and Eqs. (6.33) and (6.34) define the evolution matrices. By multiplying Eq. (6.32) with the inverse of $\mathbf{E}^{(1)}_{QLD}$ on both sides, Eq. (6.32) provides the time evolution of $f^T_{M,N}$ in one time step simultaneously in the $v_\perp$- and $v_\parallel$-spaces. The inner matrices of $\left(\mathbf{E}^{(1)}_{QLD}\right)^{-1}\mathbf{E}^{(2)}_{QLD}$ evolve $f^T_{M,N}$ in the $v_\parallel$-space while the outer matrices of $\left(\mathbf{E}^{(1)}_{QLD}\right)^{-1}\mathbf{E}^{(2)}_{QLD}$ evolve $f^T_{M,N}$ in the $v_\perp$-space during each time step. Therefore, it represents the numerical solution of Eq. (3.6) which describes the quasi-linear diffusion of a VDF through the all resonances.

6.3 Numerical Analysis for Fokker–Planck Operator

In this section, we present our numerical strategy to solve the Fokker–Planck operator for Coulomb collisions in Eq. (A.44). Using the Crank–Nicolson scheme

presented in section 6.2, we discretize Eq. (A.44) as

$$
\begin{aligned}
& f_{M,N}^{T+1} - \sum_b \Gamma_{jb} \Bigg[2\pi\Delta t \frac{m_j}{m_b} f_b f_{M,N}^{T+1} \\
& + \frac{\mu_v}{4} \left(H_{M,N}^{\perp} + \frac{G_{M,N}^{\perp}}{2v_{\perp}^2} \right) \left(f_{M+1,N}^{T+1} - f_{M-1,N}^{T+1} \right) \\
& + \frac{\mu_v}{4} H_{M,N}^{\parallel} \left(f_{M,N+1}^{T+1} - f_{M,N-1}^{T+1} \right) \\
& + \frac{\mu_{vv}}{8} G_{M,N}^{\parallel\perp} \left(f_{M+1,N+1}^{T+1} - f_{M-1,N+1}^{T+1} - f_{M+1,N-1}^{T+1} + f_{M-1,N-1}^{T+1} \right) \\
& + \frac{\mu_{vv} G_{M,N}^{\perp\perp}}{16} \left(f_{M+2,N}^{T+1} - 2 f_{M,N}^{T+1} + f_{M-2,N}^{T+1} \right) \\
& + \frac{\mu_{vv} G_{M,N}^{\parallel\parallel}}{16} \left(f_{M,N+2}^{T+1} - 2 f_{M,N}^{T+1} + f_{M,N-2}^{T+1} \right) \Bigg] \\
& = \qquad\qquad (6.35) \\
& f_{M,N}^{T} + \sum_b \Gamma_{jb} \Bigg[2\pi\Delta t \frac{m_j}{m_b} f_b f_{M,N}^{T} \\
& + \frac{\mu_v}{4} \left(H_{M,N}^{\perp} + \frac{G_{M,N}^{\perp}}{2v_{\perp}^2} \right) \left(f_{M+1,N}^{T} - f_{M-1,N}^{T} \right) \\
& + \frac{\mu_v}{4} H_{M,N}^{\parallel} \left(f_{M,N+1}^{T} - f_{M,N-1}^{T} \right) \\
& + \frac{\mu_{vv}}{8} G_{M,N}^{\parallel\perp} \left(f_{M+1,N+1}^{T} - f_{M-1,N+1}^{T} - f_{M+1,N-1}^{T} + f_{M-1,N-1}^{T} \right) \\
& + \frac{\mu_{vv} G_{M,N}^{\perp\perp}}{16} \left(f_{M+2,N}^{T} - 2 f_{M,N}^{T} + f_{M-2,N}^{T} \right) \\
& + \frac{\mu_{vv} G_{M,N}^{\parallel\parallel}}{16} \left(f_{M,N+2}^{T} - 2 f_{M,N}^{T} + f_{M,N-2}^{T} \right) \Bigg],
\end{aligned}
$$

where $\mu_v \equiv \Delta t/\Delta v$, $G_{M,N}^{\perp\perp} \equiv \partial^2 G_b/\partial v_{\perp}^2$, $G_{M,N}^{\parallel\parallel} \equiv \partial^2 G_b/\partial v_{\parallel}^2$, $G_{M,N}^{\parallel\perp} \equiv \partial^2 G_b/\partial v_{\parallel}\partial v_{\perp}$, $G_{M,N}^{\perp} \equiv \partial G_b/\partial v_{\perp}$, $H_{M,N}^{\perp} \equiv \partial H_b/\partial v_{\perp}$ and $H_{M,N}^{\parallel} \equiv \partial H_b/\partial v_{\parallel}$, estimated at $v_{\perp} = v_{\perp M}$ and $v_{\parallel} = v_{\parallel N}$. Note that we analytically estimate $G_{M,N}^{\perp\perp}$, $G_{M,N}^{\parallel\parallel}$, $G_{M,N}^{\parallel\perp}$, $G_{M,N}^{\perp}$, $H_{M,N}^{\perp}$ and $H_{M,N}^{\parallel}$ (see Appendix A.2).

Eq. (6.35) represents a system of two-dimensional algebraic equations. Therefore, we transform Eq. (6.35) into a single tridiagonal matrix using the same strategy for a two-layer matrix as presented in section 6.2. On both sides of Eq. (6.35), we group the terms by the same $v_{\perp}$-index in the VDF and rearrange these groups in

increasing order in $v_\perp$-index. In each group, we then rearrange terms in increasing order in $v_\parallel$-index in the VDF. Then, we have

$$\begin{aligned}
&-\tau_{M,N}f^{T+1}_{M-2,N}-\rho^{(1)}_{M,N}f^{T+1}_{M-1,N-1}+\rho^{(2)}_{M,N}f^{T+1}_{M-1,N}+\rho^{(1)}_{M,N}f^{T+1}_{M-1,N+1}-\varepsilon^{(2)}_{M,N}f^{T+1}_{M,N-2}\\
&+\varepsilon^{(1)}_{M,N}f^{T+1}_{M,N-1}+\chi^{(1)}_{M,N}f^{T+1}_{M,N}-\varepsilon^{(1)}_{M,N}f^{T+1}_{M,N+1}-\varepsilon^{(2)}_{M,N}f^{T+1}_{M,N+2}+\rho^{(1)}_{M,N}f^{T+1}_{M+1,N-1}\\
&-\rho^{(2)}_{M,N}f^{T+1}_{M+1,N}-\rho^{(1)}_{M,N}f^{T+1}_{M+1,N+1}-\tau_{M,N}f^{T+1}_{M+2,N}\\
&=\\
&\tau_{M,N}f^{T}_{M-2,N}+\rho^{(1)}_{M,N}f^{T}_{M-1,N-1}-\rho^{(2)}_{M,N}f^{T}_{M-1,N}-\rho^{(1)}_{M,N}f^{T}_{M-1,N+1}+\varepsilon^{(2)}_{M,N}f^{T}_{M,N-2}\\
&-\varepsilon^{(1)}_{M,N}f^{T}_{M,N-1}+\chi^{(2)}_{M,N}f^{T}_{M,N}+\varepsilon^{(1)}_{M,N}f^{T}_{M,N+1}+\varepsilon^{(2)}_{M,N}f^{T}_{M,N+2}-\rho^{(1)}_{M,N}f^{T}_{M+1,N-1}\\
&+\rho^{(2)}_{M,N}f^{T}_{M+1,N}+\rho^{(1)}_{M,N}f^{T}_{M+1,N+1}+\tau_{M,N}f^{T}_{M+2,N},
\end{aligned} \tag{6.36}$$

where

$$\chi^{(1)}_{M,N}\equiv 1-\sum_b \Gamma_{jb}\left[2\pi\Delta t\frac{m_j}{m_b}f_b-\frac{\mu_{vv}}{8}G^{\perp\perp}_{M,N}-\frac{\mu_{vv}}{8}G^{\parallel\parallel}_{M,N}\right], \tag{6.37}$$

$$\chi^{(2)}_{M,N}\equiv 1+\sum_b \Gamma_{jb}\left[2\pi\Delta t\frac{m_j}{m_b}f_b-\frac{\mu_{vv}}{8}G^{\perp\perp}_{M,N}-\frac{\mu_{vv}}{8}G^{\parallel\parallel}_{M,N}\right], \tag{6.38}$$

$$\varepsilon^{(1)}_{M,N}\equiv \sum_b \Gamma_{jb}\frac{\mu_v}{4}H^{\parallel}_{M,N}, \tag{6.39}$$

$$\varepsilon^{(2)}_{M,N}\equiv \sum_b \Gamma_{jb}\frac{\mu_{vv}}{16}G^{\parallel\parallel}_{M,N}, \tag{6.40}$$

$$\rho^{(1)}_{M,N}\equiv \sum_b \Gamma_{jb}\frac{\mu_{vv}}{8}G^{\parallel\perp}_{M,N}, \tag{6.41}$$

$$\rho^{(2)}_{M,N}\equiv \sum_b \Gamma_{jb}\frac{\mu_v}{4}\left(H^{\perp}_{M,N}+\frac{G^{\perp}_{M,N}}{2v_\perp^2}\right), \tag{6.42}$$

and

$$\tau_{M,N}\equiv \sum_b \Gamma_{jb}\frac{\mu_{vv}}{16}G^{\perp\perp}_{M,N}. \tag{6.43}$$

All terms in both sides of Eq. (6.36) with a constant $v_\perp$-index account for variations in the $v_\parallel$-space only. Therefore, they can be grouped into a single system of one-dimensional algebraic equations.

We transform all terms with $v_\perp$-index of M in the VDF on both sides of Eq. (6.36) into the tridiagonal matrices $\mathbb{X}_M^{(1)}\mathbb{F}_M^{T+1}$ and $\mathbb{X}_M^{(2)}\mathbb{F}_M^{T}$, where

$$\mathbb{X}_M^{(1)} \equiv \begin{bmatrix} \chi_{M,1}^{(1)} & -\varepsilon_{M,1}^{(1)} & -\varepsilon_{M,1}^{(2)} & 0 & 0 & \cdots & 0 \\ \varepsilon_{M,2}^{(1)} & \chi_{M,2}^{(1)} & -\varepsilon_{M,2}^{(1)} & -\varepsilon_{M,2}^{(2)} & 0 & \cdots & 0 \\ -\varepsilon_{M,3}^{(2)} & \varepsilon_{M,3}^{(1)} & \chi_{M,3}^{(1)} & -\varepsilon_{M,3}^{(1)} & -\varepsilon_{M,3}^{(2)} & \cdots & 0 \\ & \vdots & & \ddots & & \vdots & \\ 0 & \cdots & 0 & 0 & -\varepsilon_{M,N_v}^{(2)} & \varepsilon_{M,N_v}^{(1)} & \chi_{M,N_v}^{(1)} \end{bmatrix}_{N_v \times N_v}, \tag{6.44}$$

and

$$\mathbb{X}_M^{(2)} \equiv \begin{bmatrix} \chi_{M,1}^{(2)} & \varepsilon_{M,1}^{(1)} & \varepsilon_{M,1}^{(2)} & 0 & 0 & \cdots & 0 \\ -\varepsilon_{M,2}^{(1)} & \chi_{M,2}^{(2)} & \varepsilon_{M,2}^{(1)} & \varepsilon_{M,2}^{(2)} & 0 & \cdots & 0 \\ \varepsilon_{M,3}^{(2)} & -\varepsilon_{M,3}^{(1)} & \chi_{M,3}^{(2)} & \varepsilon_{M,3}^{(1)} & \varepsilon_{M,3}^{(2)} & \cdots & 0 \\ & \vdots & & \ddots & & \vdots & \\ 0 & \cdots & 0 & 0 & \varepsilon_{M,N_v}^{(2)} & -\varepsilon_{M,N_v}^{(1)} & \chi_{M,N_v}^{(2)} \end{bmatrix}_{N_v \times N_v}. \tag{6.45}$$

We transform all terms with $v_\perp$-index of $M-1$ in the VDF on both sides of Eq. (6.36) into the tridiagonal matrices $\mathbb{Y}_M\mathbb{F}_{M-1}^{T+1}$ and $-\mathbb{Y}_M\mathbb{F}_{M-1}^{T}$, where

$$\mathbb{Y}_M \equiv \begin{bmatrix} \rho_{M,1}^{(2)} & \rho_{M,1}^{(1)} & 0 & 0 & \cdots & 0 \\ -\rho_{M,2}^{(1)} & \rho_{M,2}^{(2)} & \rho_{M,2}^{(1)} & 0 & \cdots & 0 \\ & \vdots & \ddots & & & \vdots \\ 0 & \cdots & 0 & 0 & -\rho_{M,N_v}^{(1)} & \rho_{M,N_v}^{(2)} \end{bmatrix}_{N_v \times N_v}, \tag{6.46}$$

We transform all terms with $v_\perp$-index of $M+1$ in the VDF on both sides of Eq. (6.36) into the tridiagonal matrices $-\mathbb{Y}_M\mathbb{F}_{M+1}^{T+1}$ and $\mathbb{Y}_M\mathbb{F}_{M+1}^{T}$. We transform all terms with $v_\perp$-index of $M-2$ in the VDF on both sides of Eq. (6.36) into the

tridiagonal matrices $-\mathbb{Z}_M\mathbb{F}_{M-2}^{T+1}$ and $\mathbb{Z}_M\mathbb{F}_{M-2}^{T}$, where

$$\mathbb{Z}_M \equiv \begin{bmatrix} \tau_{M,1} & 0 & \cdots & 0 \\ 0 & \tau_{M,2} & \cdots & 0 \\ \vdots & & \ddots & \vdots \\ 0 & \cdots & 0 & \tau_{M,N_v} \end{bmatrix}_{N_v \times N_v} . \tag{6.47}$$

Lastly, we transform all terms with $v_\perp$-index of $M+2$ in the VDF on both sides of Eq. (6.36) into the tridiagonal matrices $-\mathbb{Z}_M\mathbb{F}_{M+2}^{T+1}$ and $\mathbb{Z}_M\mathbb{F}_{M+2}^{T}$.

This strategy allows me to express Eq. (6.36) as a single system of one-dimensional algebraic equations

$$\begin{aligned} &-\mathbb{Z}_M\mathbb{F}_{M-2}^{T+1} + \mathbb{Y}_M\mathbb{F}_{M-1}^{T+1} + \mathbb{X}_M^{(1)}\mathbb{F}_M^{T+1} - \mathbb{Y}_M\mathbb{F}_{M+1}^{T+1} - \mathbb{Z}_M\mathbb{F}_{M+2}^{T+1} \\ &= \mathbb{Z}_M\mathbb{F}_{M-2}^{T} - \mathbb{Y}_M\mathbb{F}_{M-1}^{T} + \mathbb{X}_M^{(2)}\mathbb{F}_M^{T} + \mathbb{Y}_M\mathbb{F}_{M+1}^{T} + \mathbb{Z}_M\mathbb{F}_{M+2}^{T}. \end{aligned} \tag{6.48}$$

Eq. (6.48) only describes the VDF evolution in the $v_\perp$-space. However, each matrix term itself includes the VDF evolution in the $v_\parallel$-space. We transform Eq. (6.48) into a single tridiagonal matrix

$$\mathbf{E}_F^{(1)}\mathbf{F}^{T+1} = \mathbf{E}_F^{(2)}\mathbf{F}^{T}, \tag{6.49}$$

where

$$\mathbf{E}_F^{(1)} \equiv \begin{bmatrix} \mathbb{X}_1^{(1)} & -\mathbb{Y}_1 & -\mathbb{Z}_1 & 0 & 0 & \cdots & 0 \\ \mathbb{Y}_2 & \mathbb{X}_2^{(1)} & -\mathbb{Y}_2 & -\mathbb{Z}_2 & 0 & \cdots & 0 \\ -\mathbb{Z}_3 & \mathbb{Y}_3 & \mathbb{X}_3^{(1)} & -\mathbb{Y}_3 & -\mathbb{Z}_3 & \cdots & 0 \\ & \vdots & & \ddots & & \vdots & \\ 0 & \cdots & 0 & 0 & -\mathbb{Z}_{N_v} & \mathbb{Y}_{N_v} & \mathbb{X}_{N_v}^{(1)} \end{bmatrix}_{N_v^2 \times N_v^2} , \tag{6.50}$$

and

$$\mathbf{E}_F^{(2)} \equiv \begin{bmatrix} \mathbb{X}_1^{(2)} & \mathbb{Y}_1 & \mathbb{Z}_1 & 0 & 0 & \cdots & 0 \\ -\mathbb{Y}_2 & \mathbb{X}_2^{(2)} & \mathbb{Y}_2 & \mathbb{Z}_2 & 0 & \cdots & 0 \\ \mathbb{Z}_3 & -\mathbb{Y}_3 & \mathbb{X}_3^{(2)} & \mathbb{Y}_3 & \mathbb{Z}_3 & \cdots & 0 \\ & \vdots & & \ddots & & \vdots & \\ 0 & \cdots & 0 & 0 & \mathbb{Z}_{N_v} & -\mathbb{Y}_{N_v} & \mathbb{X}_{N_v}^{(2)} \end{bmatrix}_{N_v^2 \times N_v^2}, \tag{6.51}$$

Like Eq. (6.32), Eq. (6.49) provides the time evolution of $f_{M,N}^T$ in one time step simultaneously in the $v_\perp$- and $v_\parallel$-spaces. Therefore, it represents the numerical solution of Eq. (A.44), which describes the action of Coulomb collisions of particles in f_j with particles in f_b.

6.4 Numerical Analysis for Kinetic Transport Equation

In the previous two sections, we present a mathematical approach using a two-layer matrix to numerically solve a diffusion equation with two dimensions in velocity space. In this section, we provide two different approaches to numerically solve the three-dimensional kinetic transport equation, Eq. (4.37), with two dimensions in velocity space and one dimension in configuration space.

For the sake of generality, we solve Eq. (4.37) with arbitrary coefficients for all terms:

$$\begin{aligned} \frac{\partial f_e}{\partial t} = \alpha f_e + \alpha^r \frac{\partial f_e}{\partial r} + \alpha^\perp \frac{\partial f_e}{\partial v_\perp} + \alpha^\parallel \frac{\partial f_e}{\partial v_\parallel} \\ + \alpha^{\perp\perp} \frac{\partial^2 f_e}{\partial v_\perp^2} + \alpha^{\parallel\parallel} \frac{\partial^2 f_e}{\partial v_\parallel^2} + \alpha^{\perp\parallel} \frac{\partial^2 f_e}{\partial v_\perp v_\parallel}, \end{aligned} \tag{6.52}$$

where $\alpha, \alpha^r, \alpha^\perp, \alpha^\parallel, \alpha^{\perp\perp}, \alpha^{\parallel\parallel}$ and $\alpha^{\perp\parallel}$ explicitly depend on $r, v_\perp$, and $v_\parallel$. The discrete velocity and time spaces are same as the one in previous chapters. We divide the radial space into N_r steps with equal step sizes of Δr by defining the inner and outer boundaries of radial space as r^{in} and r^{out}. The r-index L steps through 1,

2, ..., N_r. We define the discrete radial coordinate as $r_L \equiv r^{\text{in}} + (L-1)\Delta r$. We then define the discrete three-dimensional VDF as $f^T_{L,M,N} \equiv f_e(r_L, v_{\perp M}, v_{\parallel N}, t^T)$.

6.4.1 Approach fully based on the Crank–Nicolson scheme

In this section, we provide an approach which is fully based on the Crank–Nicolson scheme. We apply the Crank–Nicolson scheme to all terms in Eq. (6.52), which leads to

$$\begin{aligned}
\frac{f^{T+1}_{L,M,N} - f^T_{L,M,N}}{\Delta t} = {} & \frac{\alpha_{L,M,N}}{2}\left[f^{T+1}_{L,M,N} + f^T_{L,M,N}\right] \\
& + \frac{\alpha^r_{L,M,N}}{2}\left[\left(\frac{\partial f_e}{\partial r}\right)^{T+1}_{L,M,N} + \left(\frac{\partial f_e}{\partial r}\right)^{T}_{L,M,N}\right] \\
& + \frac{\alpha^\perp_{L,M,N}}{2}\left[\left(\frac{\partial f_e}{\partial v_\perp}\right)^{T+1}_{L,M,N} + \left(\frac{\partial f_e}{\partial v_\perp}\right)^{T}_{L,M,N}\right] \\
& + \frac{\alpha^\parallel_{L,M,N}}{2}\left[\left(\frac{\partial f_e}{\partial v_\parallel}\right)^{T+1}_{L,M,N} + \left(\frac{\partial f_e}{\partial v_\parallel}\right)^{T}_{L,M,N}\right] \\
& + \frac{\alpha^{\perp\perp}_{L,M,N}}{2}\left[\left(\frac{\partial^2 f_e}{\partial v_\perp^2}\right)^{T+1}_{L,M,N} + \left(\frac{\partial^2 f_e}{\partial v_\perp^2}\right)^{T}_{L,M,N}\right] \\
& + \frac{\alpha^{\parallel\parallel}_{L,M,N}}{2}\left[\left(\frac{\partial^2 f_e}{\partial v_\parallel^2}\right)^{T+1}_{L,M,N} + \left(\frac{\partial^2 f_e}{\partial v_\parallel^2}\right)^{T}_{L,M,N}\right] \\
& + \frac{\alpha^{\perp\parallel}_{L,M,N}}{2}\left[\left(\frac{\partial^2 f_e}{\partial v_\perp \partial v_\parallel}\right)^{T+1}_{L,M,N} + \left(\frac{\partial^2 f_e}{\partial v_\perp \partial v_\parallel}\right)^{T}_{L,M,N}\right],
\end{aligned} \tag{6.53}$$

where

$$\left(\frac{\partial f_e}{\partial r}\right)^T_{L,M,N} = \frac{f^T_{L+1,M,N} - f^T_{L-1,M,N}}{2\Delta r}, \tag{6.54}$$

$$\left(\frac{\partial f_e}{\partial v_\perp}\right)^T_{L,M,N} = \frac{f^T_{L,M+1,N} - f^T_{L,M-1,N}}{2\Delta v}, \tag{6.55}$$

$$\left(\frac{\partial f_e}{\partial v_\parallel}\right)^T_{L,M,N} = \frac{f^T_{L,M,N+1} - f^T_{L,M,N-1}}{2\Delta v}, \tag{6.56}$$

$$\left(\frac{\partial^2 f_e}{\partial v_\perp^2}\right)^T_{L,M,N} = \frac{f^T_{L,M+2,N} - 2f^T_{L,M,N} + f^T_{L,M-2,N}}{4(\Delta v)^2}, \tag{6.57}$$

$$\left(\frac{\partial^2 f_e}{\partial v_\parallel^2}\right)^T_{L,M,N} = \frac{f^T_{L,M,N+2} - 2f^T_{L,M,N} + f^T_{L,M,N-2}}{4(\Delta v)^2}, \tag{6.58}$$

$$\left(\frac{\partial^2 f_e}{\partial v_\perp \partial v_\parallel}\right)^T_{L,M,N} = \frac{f^T_{L,M+1,N+1} - f^T_{L,M+1,N-1} - f^T_{L,M-1,N+1} + f^T_{L,M-1,N-1}}{4(\Delta v)^2}, \tag{6.59}$$

and $\alpha_{L,M,N}$, $\alpha^r_{L,M,N}$, $\alpha^\perp_{L,M,N}$, $\alpha^\parallel_{L,M,N}$, $\alpha^{\perp\perp}_{L,M,N}$, $\alpha^{\parallel\parallel}_{L,M,N}$, and $\alpha^{\perp\parallel}_{L,M,N}$ are the values of $\alpha, \alpha^r, \alpha^\perp, \alpha^\parallel, \alpha^{\perp\perp}, \alpha^{\parallel\parallel}$ and $\alpha^{\perp\parallel}$, estimated at $r = r_L$, $v_\perp = v_{\perp M}$, and $v_\parallel = v_{\parallel N}$. Rearranging Eq. (6.53) yields

$$\begin{aligned}
&\frac{\mu_r}{4}\alpha^r_{L,M,N} f^{T+1}_{L-1,M,N} \\
&- \frac{\mu_{vv}}{8}\alpha^{\perp\perp}_{L,M,N} f^{T+1}_{L,M-2,N} - \frac{\mu_{vv}}{8}\alpha^{\perp\parallel}_{L,M,N} f^{T+1}_{L,M-1,N-1} + \frac{\mu_v}{4}\alpha^\perp_{L,M,N} f^{T+1}_{L,M-1,N} \\
&+ \frac{\mu_{vv}}{8}\alpha^{\perp\parallel}_{L,M,N} f^{T+1}_{L,M-1,N+1} - \frac{\mu_{vv}}{8}\alpha^{\parallel\parallel}_{L,M,N} f^{T+1}_{L,M,N-2} + \frac{\mu_v}{4}\alpha^\parallel_{L,M,N} f^{T+1}_{L,M,N-1} \\
&+ \left(1 - \frac{\Delta t}{2}\alpha_{L,M,N} + \frac{\mu_{vv}}{4}\alpha^{\perp\perp}_{L,M,N} + \frac{\mu_{vv}}{4}\alpha^{\parallel\parallel}_{L,M,N}\right) f^{T+1}_{L,M,N} \\
&- \frac{\mu_v}{4}\alpha^\parallel_{L,M,N} f^{T+1}_{L,M,N+1} - \frac{\mu_{vv}}{8}\alpha^{\parallel\parallel}_{L,M,N} f^{T+1}_{L,M,N+2} + \frac{\mu_{vv}}{8}\alpha^{\perp\parallel}_{L,M,N} f^{T+1}_{L,M+1,N-1} \\
&- \frac{\mu_v}{4}\alpha^\perp_{L,M,N} f^{T+1}_{L,M+1,N} - \frac{\mu_{vv}}{8}\alpha^{\perp\parallel}_{L,M,N} f^{T+1}_{L,M+1,N+1} - \frac{\mu_{vv}}{8}\alpha^{\perp\perp}_{L,M,N} f^{T+1}_{L,M+2,N} \\
&- \frac{\mu_r}{4}\alpha^r_{L,M,N} f^{T+1}_{L+1,M,N} \\
&= \\
&- \frac{\mu_r}{4}\alpha^r_{L,M,N} f^T_{L-1,M,N} \\
&\frac{\mu_{vv}}{8}\alpha^{\perp\perp}_{L,M,N} f^T_{L,M-2,N} + \frac{\mu_{vv}}{8}\alpha^{\perp\parallel}_{L,M,N} f^T_{L,M-1,N-1} - \frac{\mu_v}{4}\alpha^\perp_{L,M,N} f^T_{L,M-1,N} \\
&- \frac{\mu_{vv}}{8}\alpha^{\perp\parallel}_{L,M,N} f^T_{L,M-1,N+1} + \frac{\mu_{vv}}{8}\alpha^{\parallel\parallel}_{L,M,N} f^T_{L,M,N-2} - \frac{\mu_v}{4}\alpha^\parallel_{L,M,N} f^T_{L,M,N-1} \\
&+ \left(1 + \frac{\Delta t}{2}\alpha_{L,M,N} - \frac{\mu_{vv}}{4}\alpha^{\perp\perp}_{L,M,N} - \frac{\mu_{vv}}{4}\alpha^{\parallel\parallel}_{L,M,N}\right) f^T_{L,M,N} \\
&+ \frac{\mu_v}{4}\alpha^\parallel_{L,M,N} f^T_{L,M,N+1} + \frac{\mu_{vv}}{8}\alpha^{\parallel\parallel}_{L,M,N} f^T_{L,M,N+2} - \frac{\mu_{vv}}{8}\alpha^{\perp\parallel}_{L,M,N} f^T_{L,M+1,N-1} \\
&+ \frac{\mu_v}{4}\alpha^\perp_{L,M,N} f^T_{L,M+1,N} + \frac{\mu_{vv}}{8}\alpha^{\perp\parallel}_{L,M,N} f^T_{L,M+1,N+1} + \frac{\mu_{vv}}{8}\alpha^{\perp\perp}_{L,M,N} f^T_{L,M+2,N} \\
&+ \frac{\mu_r}{4}\alpha^r_{L,M,N} f^T_{L+1,M,N}
\end{aligned} \tag{6.60}$$

where $\mu_r = \Delta t/\Delta r$. On both sides of Eq. (6.60), we group the terms by the same r-index of VDFs, and arrange these groups in increasing order in r-index of VDFs. In each group of the same r-index of VDFs, we group the terms by the same $v_\perp$-index of VDFs, and arrange these groups in increasing order in $v_\perp$-index of VDFs. In each group by the same r and $v_\perp$-indices of VDFs, we arrange terms in increasing order in $v_\parallel$-index of VDFs. Eq. (6.60) is a three-dimensional set of algebraic matrix equations. The arrangement shown in Eq. (6.60) allows us to transform Eq. (6.60) into a single matrix equation by using a three-layer matrix.

We transform all terms with r-index L and $v_\perp$-index M in the VDF on both sides of Eq. (6.60) into the tridiagonal matrices $\mathbb{A}^{(1)}_{L,M}\mathbb{F}^{T+1}_{L,M}$ and $\mathbb{A}^{(2)}_{L,M}\mathbb{F}^{T}_{L,M}$, where $\mathbb{F}^{T}_{L,M} \equiv [f^T_{L,M,1}\, f^T_{L,M,2} \cdots f^T_{L,M,N_v}]^{\mathbf{T}}_{1\times N_v}$. We then find that

$$\mathbb{A}^{(1)}_{L,M} \equiv \begin{bmatrix} \alpha^{(1)}_{L,M,1} & -\frac{\mu_v}{4}\alpha^{\parallel}_{L,M,1} & -\frac{\mu_{vv}}{8}\alpha^{\parallel\parallel}_{L,M,1} & 0 & \cdots & 0 \\ \frac{\mu_v}{4}\alpha^{\parallel}_{L,M,2} & \alpha^{(1)}_{L,M,2} & -\frac{\mu_v}{4}\alpha^{\parallel}_{L,M,2} & -\frac{\mu_{vv}}{8}\alpha^{\parallel\parallel}_{L,M,2} & \cdots & 0 \\ & \vdots & & \ddots & & \vdots \\ 0 & \cdots & 0 & -\frac{\mu_{vv}}{8}\alpha^{\parallel\parallel}_{L,M,N_v} & \frac{\mu_v}{4}\alpha^{\parallel}_{L,M,N_v} & \alpha^{(1)}_{L,M,N_v} \end{bmatrix}_{N_v\times N_v}, \tag{6.61}$$

$$\alpha^{(1)}_{L,M,N} = 1 - \frac{\Delta t}{2}\alpha_{L,M,N} + \frac{\mu_{vv}}{4}\alpha^{\perp\perp}_{L,M,N} + \frac{\mu_{vv}}{4}\alpha^{\parallel\parallel}_{L,M,N}, \tag{6.62}$$

$$\mathbb{A}^{(2)}_{L,M} \equiv \begin{bmatrix} \alpha^{(2)}_{L,M,1} & \frac{\mu_v}{4}\alpha^{\parallel}_{L,M,1} & \frac{\mu_{vv}}{8}\alpha^{\parallel\parallel}_{L,M,1} & 0 & \cdots & 0 \\ -\frac{\mu_v}{4}\alpha^{\parallel}_{L,M,2} & \alpha^{(2)}_{L,M,2} & \frac{\mu_v}{4}\alpha^{\parallel}_{L,M,2} & \frac{\mu_{vv}}{8}\alpha^{\parallel\parallel}_{L,M,2} & \cdots & 0 \\ & \vdots & & \ddots & & \vdots \\ 0 & \cdots & 0 & \frac{\mu_{vv}}{8}\alpha^{\parallel\parallel}_{L,M,N_v} & -\frac{\mu_v}{4}\alpha^{\parallel}_{L,M,N_v} & \alpha^{(2)}_{L,M,N_v} \end{bmatrix}_{N_v\times N_v}, \tag{6.63}$$

and

$$\alpha^{(2)}_{L,M,N} = 1 + \frac{\Delta t}{2}\alpha_{L,M,N} - \frac{\mu_{vv}}{4}\alpha^{\perp\perp}_{L,M,N} - \frac{\mu_{vv}}{4}\alpha^{\parallel\parallel}_{L,M,N}. \tag{6.64}$$

We transform all terms with r-index L and $v_\perp$-index $M-1$ in the VDF on both sides

of Eq. (6.60) into the tridiagonal matrices $\mathbb{B}_{L,M}\mathbb{F}^{T+1}_{L,M-1}$ and $-\mathbb{B}_{L,M}\mathbb{F}^{T}_{L,M-1}$, where

$$\mathbb{B}_{L,M} \equiv \begin{bmatrix} \frac{\mu_v}{4}\alpha^{\perp}_{L,M,1} & \frac{\mu_{vv}}{8}\alpha^{\perp\|}_{L,M,1} & 0 & \cdots & 0 \\ -\frac{\mu_{vv}}{8}\alpha^{\perp\|}_{L,M,2} & \frac{\mu_v}{4}\alpha^{\perp}_{L,M,2} & \frac{\mu_{vv}}{8}\alpha^{\perp\|}_{L,M,2} & \cdots & 0 \\ & \vdots & \ddots & & \vdots \\ 0 & \cdots & 0 & -\frac{\mu_{vv}}{8}\alpha^{\perp\|}_{L,M,N_v} & \frac{\mu_v}{4}\alpha^{\perp}_{L,M,N_v} \end{bmatrix}_{N_v\times N_v} . \quad (6.65)$$

We transform all terms with r-index L and $v_\perp$-index $M+1$ in the VDF on both sides of Eq. (6.60) into the tridiagonal matrices $-\mathbb{B}_{L,M}\mathbb{F}^{T+1}_{L,M+1}$ and $\mathbb{B}_{L,M}\mathbb{F}^{T}_{L,M+1}$. Likewise, we transform all terms with r-index L and $v_\perp$-index $M-2$ in the VDF on both sides of Eq. (6.60) into the tridiagonal matrices $-\mathbb{C}_{L,M}\mathbb{F}^{T+1}_{L,M-2}$ and $\mathbb{C}_{L,M}\mathbb{F}^{T}_{L,M-2}$, where

$$\mathbb{C}_{L,M} \equiv \begin{bmatrix} \frac{\mu_{vv}}{8}\alpha^{\perp\perp}_{L,M,1} & 0 & \cdots & 0 \\ 0 & \frac{\mu_{vv}}{8}\alpha^{\perp\perp}_{L,M,2} & \cdots & 0 \\ \vdots & & \ddots & \vdots \\ 0 & \cdots & 0 & \frac{\mu_{vv}}{8}\alpha^{\perp\perp}_{L,M,N_v} \end{bmatrix}_{N_v\times N_v} . \quad (6.66)$$

We transform all terms with r-index L and $v_\perp$-index $M+2$ in the VDF on both sides of Eq. (6.60) into the tridiagonal matrices $-\mathbb{C}_{L,M}\mathbb{F}^{T+1}_{L,M+2}$ and $\mathbb{C}_{L,M}\mathbb{F}^{T}_{L,M+2}$. Likewise, we transform all terms with r-index $L-1$ and $v_\perp$-index M in the VDF on both sides of Eq. (6.60) into the tridiagonal matrices $\mathbb{D}_{L,M}\mathbb{F}^{T+1}_{L-1,M}$ and $-\mathbb{D}_{L,M}\mathbb{F}^{T}_{L-1,M}$, where

$$\mathbb{D}_{L,M} \equiv \begin{bmatrix} \frac{\mu_r}{4}\alpha^{r}_{L,M,1} & 0 & \cdots & 0 \\ 0 & \frac{\mu_r}{4}\alpha^{r}_{L,M,2} & \cdots & 0 \\ \vdots & & \ddots & \vdots \\ 0 & \cdots & 0 & \frac{\mu_r}{4}\alpha^{r}_{L,M,N_v} \end{bmatrix}_{N_v\times N_v} . \quad (6.67)$$

Lastly, we transform all terms with r-index $L+1$ and $v_\perp$-index M in the VDF on both sides of Eq. (6.60) into the tridiagonal matrices $-\mathbb{D}_{L,M}\mathbb{F}^{T+1}_{L+1,M}$ and $\mathbb{D}_{L,M}\mathbb{F}^{T}_{L+1,M}$. By combining all transformed matrices, Eq. (6.60) becomes a two-

dimensional set of algebraic matrix equations given as

$$\begin{aligned}
&\mathbb{D}_{L,M}\mathbb{F}^{T+1}_{L-1,M} - \mathbb{C}_{L,M}\mathbb{F}^{T+1}_{L,M-2} + \mathbb{B}_{L,M}\mathbb{F}^{T+1}_{L,M-1} + \mathbb{A}^{(1)}_{L,M}\mathbb{F}^{T+1}_{L,M} - \mathbb{B}_{L,M}\mathbb{F}^{T+1}_{L,M+1} \\
&- \mathbb{C}_{L,M}\mathbb{F}^{T+1}_{L,M+2} - \mathbb{D}_{L,M}\mathbb{F}^{T+1}_{L+1,M} \\
&= -\mathbb{D}_{L,M}\mathbb{F}^{T}_{L-1,M} + \mathbb{C}_{L,M}\mathbb{F}^{T}_{L,M-2} - \mathbb{B}_{L,M}\mathbb{F}^{T}_{L,M-1} + \mathbb{A}^{(2)}_{L,M}\mathbb{F}^{T}_{L,M} + \mathbb{B}_{L,M}\mathbb{F}^{T}_{L,M+1} \\
&+ \mathbb{C}_{L,M}\mathbb{F}^{T}_{L,M+2} + \mathbb{D}_{L,M}\mathbb{F}^{T}_{L+1,M}.
\end{aligned} \tag{6.68}$$

Eq. (6.68) describes the VDF evolution in r- and $v_\perp$-space. However, each matrix term itself includes the VDF evolution in $v_\parallel$-space. Once again, we transform all terms with r-index L in the VDF on both sides of Eq. (6.68) into the tridiagonal matrices $\mathbf{A}^{(1)}_L\mathbf{F}^{T+1}_L$ and $\mathbf{A}^{(2)}_L\mathbf{F}^{T}_L$, where $\mathbf{F}^T_L \equiv [\mathbb{F}^T_{L,1}\,\mathbb{F}^T_{L,2}\cdots\mathbb{F}^T_{L,N_v}]^{\mathbf{T}}_{1\times(N_v)^2}$,

$$\mathbf{A}^{(1)}_L \equiv \begin{bmatrix}
\mathbb{A}^{(1)}_{L,1} & -\mathbb{B}_{L,1} & -\mathbb{C}_{L,1} & 0 & 0 & \cdots & 0 \\
\mathbb{B}_{L,2} & \mathbb{A}^{(1)}_{L,2} & -\mathbb{B}_{L,2} & -\mathbb{C}_{L,2} & 0 & \cdots & 0 \\
-\mathbb{C}_{L,3} & \mathbb{B}_{L,3} & \mathbb{A}^{(1)}_{L,3} & -\mathbb{B}_{L,3} & -\mathbb{C}_{L,3} & \cdots & 0 \\
 & \vdots & & \ddots & & \vdots & \\
0 & \cdots & 0 & 0 & -\mathbb{C}_{L,N_v} & \mathbb{B}_{L,N_v} & \mathbb{A}^{(1)}_{L,N_v}
\end{bmatrix}_{(N_v)^2\times(N_v)^2}, \tag{6.69}$$

and

$$\mathbf{A}^{(2)}_L \equiv \begin{bmatrix}
\mathbb{A}^{(2)}_{L,1} & \mathbb{B}_{L,1} & \mathbb{C}_{L,1} & 0 & 0 & \cdots & 0 \\
-\mathbb{B}_{L,2} & \mathbb{A}^{(2)}_{L,2} & \mathbb{B}_{L,2} & \mathbb{C}_{L,2} & 0 & \cdots & 0 \\
\mathbb{C}_{L,3} & -\mathbb{B}_{L,3} & \mathbb{A}^{(2)}_{L,3} & \mathbb{B}_{L,3} & \mathbb{C}_{L,3} & \cdots & 0 \\
 & \vdots & & \ddots & & \vdots & \\
0 & \cdots & 0 & 0 & \mathbb{C}_{L,N_v} & -\mathbb{B}_{L,N_v} & \mathbb{A}^{(2)}_{L,N_v}
\end{bmatrix}_{(N_v)^2\times(N_v)^2}. \tag{6.70}$$

We transform the term with r-index $L-1$ in the VDF on both sides of Eq. (6.68)

into the tridiagonal matrices $\mathbf{D}_L\mathbf{F}_{L-1}^{T+1}$ and $-\mathbf{D}_L\mathbf{F}_{L-1}^{T}$, where

$$\mathbf{D}_L \equiv \begin{bmatrix} \mathbb{D}_{L,1} & 0 & \cdots & 0 \\ 0 & \mathbb{D}_{L,2} & \cdots & 0 \\ \vdots & & \ddots & \vdots \\ 0 & \cdots & 0 & \mathbb{D}_{L,N_v} \end{bmatrix}_{(N_v)^2\times(N_v)^2} . \tag{6.71}$$

Lastly, we transform the term with r-index $L+1$ in the VDF on both sides of Eq. (6.68) into the tridiagonal matrices $-\mathbf{D}_L\mathbf{F}_{L+1}^{T+1}$ and $\mathbf{D}_L\mathbf{F}_{L+1}^{T}$. By combining all transformed matrices, Eq. (6.68) becomes a one-dimensional set of algebraic matrix equations given as

$$\mathbf{D}_L\mathbf{F}_{L-1}^{T+1} + \mathbf{A}_L^{(1)}\mathbf{F}_L^{T+1} - \mathbf{D}_L\mathbf{F}_{L+1}^{T+1} = -\mathbf{D}_L\mathbf{F}_{L-1}^{T} + \mathbf{A}_L^{(2)}\mathbf{F}_L^{T} + \mathbf{D}_L\mathbf{F}_{L+1}^{T}. \tag{6.72}$$

Eq. (6.72) only describes the VDF evolution in the r-space. However, each term in Eq. (6.72) is in the form of a two-layer matrix. The outer matrices evolve $f_{L,M,N}^{T}$ in $v_\perp$-space, and the inner matrices evolve $f_{L,M,N}^{T}$ in $v_\parallel$-space during each time step. Lastly, we transform Eq. (6.72) into a single tridiagonal matrix

$$\overline{\mathbf{A}}^{(1)}\overline{\mathbf{F}}^{T+1} = \overline{\mathbf{A}}^{(2)}\overline{\mathbf{F}}^{T}, \tag{6.73}$$

where $\overline{\mathbf{F}}^{T} \equiv [\mathbf{F}_1^T\ \mathbf{F}_2^T\ \cdots\ \mathbf{F}_{N_r}^T]^{\mathbf{T}}_{1\times N_r(N_v)^2}$.

$$\overline{\mathbf{A}}^{(1)} = \begin{bmatrix} \mathbf{A}_1^{(1)} & -\mathbf{D}_1 & 0 & 0 & \cdots & 0 \\ \mathbf{D}_2 & \mathbf{A}_2^{(1)} & -\mathbf{D}_2 & 0 & \cdots & 0 \\ 0 & \mathbf{D}_3 & \mathbf{A}_3^{(1)} & -\mathbf{D}_3 & \cdots & 0 \\ & \vdots & & \ddots & & \vdots \\ 0 & \cdots & 0 & 0 & \mathbf{D}_{N_r} & \mathbf{A}_{N_r}^{(1)} \end{bmatrix}_{N_r(N_v)^2\times N_r(N_v)^2} \tag{6.74}$$

and

$$\overline{\mathbf{A}}^{(2)} = \begin{bmatrix} \mathbf{A}_1^{(2)} & \mathbf{D}_1 & 0 & 0 & \cdots & 0 \\ -\mathbf{D}_2 & \mathbf{A}_2^{(2)} & \mathbf{D}_2 & 0 & \cdots & 0 \\ 0 & -\mathbf{D}_3 & \mathbf{A}_3^{(2)} & \mathbf{D}_3 & \cdots & 0 \\ & \vdots & & \ddots & & \vdots \\ 0 & \cdots & 0 & 0 & -\mathbf{D}_{N_r} & \mathbf{A}_{N_r}^{(2)} \end{bmatrix}_{N_r(N_v)^2 \times N_r(N_v)^2} \tag{6.75}$$

Eq. (6.73) is in the form of a 3-layer matrix, and Eqs. (6.74) and (6.75) define the evolution matrices. By multiplying Eq. (6.73) with the inverse of $\overline{\mathbf{A}}^{(1)}$ on both sides, Eq. (6.73) provides the time evolution of $f^T_{L,M,N}$ in one time step simultaneously in the r-, $v_\perp$- and $v_\parallel$-spaces. The innermost matrices of $\left(\overline{\mathbf{A}}^{(1)}\right)^{-1}\overline{\mathbf{A}}^{(2)}$ evolve $f^T_{L,M,N}$ in the $v_\parallel$-space, the middle matrices of $\left(\overline{\mathbf{A}}^{(1)}\right)^{-1}\overline{\mathbf{A}}^{(2)}$ evolve $f^T_{L,M,N}$ in the $v_\perp$-space, and the outermost matrices of $\left(\overline{\mathbf{A}}^{(1)}\right)^{-1}\overline{\mathbf{A}}^{(2)}$ evolve $f^T_{L,M,N}$ in the r-space during each time step.

6.4.2 Approach based on the combination of the Crank–Nicolson scheme and Euler scheme

In the previous section, we numerically solve Eq. (6.52) through the three-layer matrix approach by fully applying the Crank–Nicolson scheme. However, the size of the three-layer matrix can easily be computationally too expensive to run the code. Therefore, a good resolution may not be achievable due to the limited amount of computational resources.

In this section, we apply the Crank–Nicolson scheme only to the velocity derivatives and the source term, and a forward Euler scheme to the radial deriva-

tive to Eq. (6.52), which leads to

$$
\begin{aligned}
\frac{f_{L,M,N}^{T+1}-f_{L,M,N}^{T}}{\Delta t} &= \frac{\alpha_{L,M,N}}{2}\left[f_{L,M,N}^{T+1}+f_{L,M,N}^{T}\right] \\
&+\alpha_{L,M,N}^{r}\left(\frac{\partial f_e}{\partial r}\right)_{L,M,N}^{T} \\
&+\frac{\alpha_{L,M,N}^{\perp}}{2}\left[\left(\frac{\partial f_e}{\partial v_\perp}\right)_{L,M,N}^{T+1}+\left(\frac{\partial f_e}{\partial v_\perp}\right)_{L,M,N}^{T}\right] \\
&+\frac{\alpha_{L,M,N}^{\parallel}}{2}\left[\left(\frac{\partial f_e}{\partial v_\parallel}\right)_{L,M,N}^{T+1}+\left(\frac{\partial f_e}{\partial v_\parallel}\right)_{L,M,N}^{T}\right] \\
&+\frac{\alpha_{L,M,N}^{\perp\perp}}{2}\left[\left(\frac{\partial^2 f_e}{\partial v_\perp^2}\right)_{L,M,N}^{T+1}+\left(\frac{\partial^2 f_e}{\partial v_\perp^2}\right)_{L,M,N}^{T}\right] \\
&+\frac{\alpha_{L,M,N}^{\parallel\parallel}}{2}\left[\left(\frac{\partial^2 f_e}{\partial v_\parallel^2}\right)_{L,M,N}^{T+1}+\left(\frac{\partial^2 f_e}{\partial v_\parallel^2}\right)_{L,M,N}^{T}\right] \\
&+\frac{\alpha_{L,M,N}^{\perp\parallel}}{2}\left[\left(\frac{\partial^2 f_e}{\partial v_\perp \partial v_\parallel}\right)_{L,M,N}^{T+1}+\left(\frac{\partial^2 f_e}{\partial v_\perp \partial v_\parallel}\right)_{L,M,N}^{T}\right],
\end{aligned}
\tag{6.76}
$$

Rearranging Eq. (6.76) yields

$$
\begin{aligned}
&-\frac{\mu_{vv}}{8}\alpha^{\perp\perp}_{L,M,N}f^{T+1}_{L,M-2,N}-\frac{\mu_{vv}}{8}\alpha^{\perp\parallel}_{L,M,N}f^{T+1}_{L,M-1,N-1}+\frac{\mu_{v}}{4}\alpha^{\perp}_{L,M,N}f^{T+1}_{L,M-1,N}\\
&+\frac{\mu_{vv}}{8}\alpha^{\perp\parallel}_{L,M,N}f^{T+1}_{L,M-1,N+1}-\frac{\mu_{vv}}{8}\alpha^{\parallel\parallel}_{L,M,N}f^{T+1}_{L,M,N-2}+\frac{\mu_{v}}{4}\alpha^{\parallel}_{L,M,N}f^{T+1}_{L,M,N-1}\\
&+\left(1-\frac{\Delta t}{2}\alpha_{L,M,N}+\frac{\mu_{vv}}{4}\alpha^{\perp\perp}_{L,M,N}+\frac{\mu_{vv}}{4}\alpha^{\parallel\parallel}_{L,M,N}\right)f^{T+1}_{L,M,N}\\
&-\frac{\mu_{v}}{4}\alpha^{\parallel}_{L,M,N}f^{T+1}_{L,M,N+1}-\frac{\mu_{vv}}{8}\alpha^{\parallel\parallel}_{L,M,N}f^{T+1}_{L,M,N+2}+\frac{\mu_{vv}}{8}\alpha^{\perp\parallel}_{L,M,N}f^{T+1}_{L,M+1,N-1}\\
&-\frac{\mu_{v}}{4}\alpha^{\perp}_{L,M,N}f^{T+1}_{L,M+1,N}-\frac{\mu_{vv}}{8}\alpha^{\perp\parallel}_{L,M,N}f^{T+1}_{L,M+1,N+1}-\frac{\mu_{vv}}{8}\alpha^{\perp\perp}_{L,M,N}f^{T+1}_{L,M+2,N}\\
&=\\
&\frac{\mu_{vv}}{8}\alpha^{\perp\perp}_{L,M,N}f^{T}_{L,M-2,N}+\frac{\mu_{vv}}{8}\alpha^{\perp\parallel}_{L,M,N}f^{T}_{L,M-1,N-1}-\frac{\mu_{v}}{4}\alpha^{\perp}_{L,M,N}f^{T}_{L,M-1,N}\\
&-\frac{\mu_{vv}}{8}\alpha^{\perp\parallel}_{L,M,N}f^{T}_{L,M-1,N+1}+\frac{\mu_{vv}}{8}\alpha^{\parallel\parallel}_{L,M,N}f^{T}_{L,M,N-2}-\frac{\mu_{v}}{4}\alpha^{\parallel}_{L,M,N}f^{T}_{L,M,N-1}\\
&+\left(1+\frac{\Delta t}{2}\alpha_{L,M,N}-\frac{\mu_{vv}}{4}\alpha^{\perp\perp}_{L,M,N}-\frac{\mu_{vv}}{4}\alpha^{\parallel\parallel}_{L,M,N}\right)f^{T}_{L,M,N}\\
&+\frac{\mu_{v}}{4}\alpha^{\parallel}_{L,M,N}f^{T}_{L,M,N+1}+\frac{\mu_{vv}}{8}\alpha^{\parallel\parallel}_{L,M,N}f^{T}_{L,M,N+2}-\frac{\mu_{vv}}{8}\alpha^{\perp\parallel}_{L,M,N}f^{T}_{L,M+1,N-1}\\
&+\frac{\mu_{v}}{4}\alpha^{\perp}_{L,M,N}f^{T}_{L,M+1,N}+\frac{\mu_{vv}}{8}\alpha^{\perp\parallel}_{L,M,N}f^{T}_{L,M+1,N+1}+\frac{\mu_{vv}}{8}\alpha^{\perp\perp}_{L,M,N}f^{T}_{L,M+2,N}\\
&+\frac{\mu_{r}}{2}\alpha^{r}_{L,M,N}\left[f^{T}_{L+1,M,N}-f^{T}_{L-1,M,N}\right]
\end{aligned}
\tag{6.77}
$$

where $\mu_r = \Delta t/\Delta r$. On both sides of Eq. (6.77), we group the terms by the same $v_\perp$-index of VDFs with r-index of L and arrange these groups in increasing order in $v_\perp$-index of VDFs. In each group, we arrange terms in increasing order in $v_\parallel$-index of VDFs. On the right-hand side of Eq. (6.77), we leave terms which have VDFs with r-index of $L+1$ and $L-1$ in the form of Euler scheme. Eq. (6.77) is a three-dimensional set of algebraic matrix equations. Eq. (6.77) is implicit for the two-dimensional velocity space, resulting from the Crank–Nicolson scheme, and explicit for the one-dimensional configuration (r) space, resulting from the Euler scheme. The arrangement shown in Eq. (6.77) allows us to transform Eq. (6.77) into a one-dimensional explicit equation in r-space by applying the concept of a two-layer matrix to the velocity space.

We transform all terms with r-index L and $v_\perp$-index M in the VDF on both sides of Eq. (6.77) into the tridiagonal matrices $\mathbb{A}^{(1)}_{L,M}\mathbb{F}^{T+1}_{L,M}$ and $\mathbb{A}^{(2)}_{L,M}\mathbb{F}^{T}_{L,M}$. We trans-

form all terms with r-index L and $v_\perp$-index $M-1$ in the VDF on both sides of Eq. (6.77) into the tridiagonal matrices $\mathbb{B}_{L,M}\mathbb{F}^{T+1}_{L,M-1}$ and $-\mathbb{B}_{L,M}\mathbb{F}^{T}_{L,M-1}$. We transform all terms with r-index L and $v_\perp$-index $M+1$ in the VDF on both sides of Eq. (6.77) into the tridiagonal matrices $-\mathbb{B}_{L,M}\mathbb{F}^{T+1}_{L,M+1}$ and $\mathbb{B}_{L,M}\mathbb{F}^{T}_{L,M+1}$. Likewise, we transform all terms with r-index L and $v_\perp$-index $M-2$ in the VDF on both sides of Eq. (6.77) into the tridiagonal matrices $-\mathbb{C}_{L,M}\mathbb{F}^{T+1}_{L,M-2}$ and $\mathbb{C}_{L,M}\mathbb{F}^{T}_{L,M-2}$. We transform all terms with r-index L and $v_\perp$-index $M+2$ in the VDF on both sides of Eq. (6.77) into the tridiagonal matrices $-\mathbb{C}_{L,M}\mathbb{F}^{T+1}_{L,M+2}$ and $\mathbb{C}_{L,M}\mathbb{F}^{T}_{L,M+2}$. Likewise, we transform all terms with r-index $L-1$ and $v_\perp$-index M in the VDF on the right-hand side of Eq. (6.77) into the tridiagonal matrices $-2\mathbb{D}_{L,M}\mathbb{F}^{T}_{L-1,M}$. Lastly, we transform all terms with r-index $L+1$ and $v_\perp$-index M in the VDF on the right-hand side of Eq. (6.77) into the tridiagonal matrices $2\mathbb{D}_{L,M}\mathbb{F}^{T}_{L+1,M}$. By combining all transformed matrices, Eq. (6.77) becomes a two-dimensional set of algebraic matrix equations given as

$$\begin{aligned}
&-\mathbb{C}_{L,M}\mathbb{F}^{T+1}_{L,M-2}+\mathbb{B}_{L,M}\mathbb{F}^{T+1}_{L,M-1}+\mathbb{A}^{(1)}_{L,M}\mathbb{F}^{T+1}_{L,M}-\mathbb{B}_{L,M}\mathbb{F}^{T+1}_{L,M+1}-\mathbb{C}_{L,M}\mathbb{F}^{T+1}_{L,M+2}\\
&=\mathbb{C}_{L,M}\mathbb{F}^{T}_{L,M-2}-\mathbb{B}_{L,M}\mathbb{F}^{T}_{L,M-1}+\mathbb{A}^{(2)}_{L,M}\mathbb{F}^{T}_{L,M}+\mathbb{B}_{L,M}\mathbb{F}^{T}_{L,M+1}+\mathbb{C}_{L,M}\mathbb{F}^{T}_{L,M+2}\\
&+2\mathbb{D}_{L,M}\left[\mathbb{F}^{T}_{L+1,M}-\mathbb{F}^{T}_{L-1,M}\right].
\end{aligned} \tag{6.78}$$

Eq. (6.78) describes the VDF evolution in r- and $v_\perp$-space. However, each matrix term itself includes the VDF evolution in $v_\parallel$-space. Once again, we transform all terms with r-index L in the VDF on both sides of Eq. (6.78) into the tridiagonal matrices $\mathbf{A}^{(1)}_L\mathbf{F}^{T+1}_L$ and $\mathbf{A}^{(2)}_L\mathbf{F}^{T}_L$. We transform the term with r-index $L-1$ in the VDF on the right-hand side of Eq. (6.78) into the tridiagonal matrices $-2\mathbf{D}_L\mathbf{F}^{T}_{L-1}$. Lastly, we transform the term with r-index $L+1$ in the VDF on the right-hand side of Eq. (6.78) into the tridiagonal matrices $2\mathbf{D}_L\mathbf{F}^{T}_{L+1}$. By combining all transformed matrices, Eq. (6.78) becomes a one-dimensional set of algebraic matrix equations given as

$$\mathbf{A}^{(1)}_L\mathbf{F}^{T+1}_L=\mathbf{A}^{(2)}_L\mathbf{F}^{T}_L+2\mathbf{D}_L\left[\mathbf{F}^{T}_{L+1}-\mathbf{F}^{T}_{L-1}\right]. \tag{6.79}$$

Eq. (6.79) is a one-dimensional explicit equation as a form of Euler scheme, and describes the VDF evolution in r-space. However, each term in Eq. (6.79) is in the form of a two-layer matrix. The outer matrices evolve $f^T_{L,M,N}$ in $v_\perp$-space, and the inner matrices evolve $f^T_{L,M,N}$ in $v_\parallel$-space during each time step. By multiplying Eq. (6.79) with the inverse of the tridiagonal matrix $\mathbf{A}^{(1)}_L$ from Eq. (6.69), $\mathbf{F}^T_L$ evolves in the r-, $v_\perp$- and $v_\parallel$-spaces for one time step. Eq. (6.79) is then repeated to step through further time steps as required.

This strategy requires a two-layer matrix because the implicit method is applied only to the two-dimensional velocity space. It means that the computational effort required for the combination of the Crank–Nicolson and Euler schemes is much less than the one required for a pure Crank–Nicolson scheme.

6.5 Summary

For the computational evaluation of our theoretical models, we introduce a mathematical approach based on the Crank–Nicolson scheme to numerically solve our kinetic equations. We highlight that this mathematical approach applies to all general diffusion equations with an arbitrary N-dimension, including those with off-diagonal diffusion terms. Therefore, our mathematical approach is applicable to a variety of fields, such as the financial industry to solve the Black–Scholes equation (Wade et al., 2007; Persson and Persson, 2007; Kim et al., 2016).

Chapter 7

Conclusions and Future Studies

Kinetic plasma physics is of great importance to understand phenomena which prevail in the solar-wind plasma. This thesis develops analytical models to describe the evolution of solar-wind electrons through local wave–particle interactions and the global plasma expansion. In addition, this thesis provides the data and numerical analysis tools to support our theoretical work.

7.1 Summary and Conclusions

This thesis starts by introducing the fundamentals of kinetic plasma physics in Chapter 1. Following that, we discuss why this approach is essential for describing the evolution of the solar wind in Chapter 2. Based on what we have discussed in the first two chapters, the importance of a comprehensive kinetic model for the solar wind has become clear to explain the non-Maxwellian features which appear in *in-situ* plasma measurements in the solar wind.

We propose a quasi-linear diffusion model for any generalised wave–particle instability in Chapter 3. We analyse the quasi-linear diffusion equation by expressing the electric field of an arbitrary unstable and resonant wave mode as a Gaussian wave packet. From Boltzmann's H-theorem in our quasi-linear analysis, we define a window function that determines the specific velocity-space range in which a dominant wave–particle instability and counter-acting damping contributions are effective. This window function is the consequence of the localised energy density of our Gaussian wave packet both in configuration space and in wavevector space.

Moreover, we derive a relation describing the diffusive trajectories of the resonant particles for such an instability in velocity space. These trajectories evolve the particle VDF into a stable state in which no further quasi-linear diffusion occurs. Therefore, our theoretical model illustrates the diffusion and stabilisation which resonant particles, depending on their location in velocity space, experience in wave–particle interactions.

As an example, we apply our model to the oblique FM/W instability that is able to scatter strahl electrons in the solar wind. Our model shows that the $n = +1$ resonant instability of FM/W waves propagating with an angle of $\sim 55^\circ$ with respect to the background magnetic field scatters strahl electrons towards larger $v_\perp$ and smaller $v_\parallel$. The strahl scattering instability through the $n = +1$ resonance dominates over the counter-acting damping contributions from the electron core through the $n = -1$ and $n = 0$ resonances. This instability creates a strong pitch-angle gradient in the electron-strahl VDF. We also show that Coulomb collisions of strahl electrons with core electrons and protons relax this strong pitch-angle gradient on a timescale 10^5 times longer than the timescale of the collisionless strahl scattering at a heliocentric distance of 0.3 au. This finding suggests that, apart from this second-order relaxation process, collisional effects are negligible in the strahl-driven oblique FM/W instability, which is a representative example for a resonant wave–particle instability in the solar wind.

This work, for the first time, presents a quasi-linear description of the strahl scattering through the oblique FM/W instability, which had been predicted based on linear theory. Our predicted evolution of the electron VDF is consistent with the observed formation of a proto-halo through strahl scattering (Gurgiolo et al., 2012). However, further observations are ambiguous regarding the exact source of the proto-halo (Gurgiolo and Goldstein, 2016). High-resolution electron observations with Solar Orbiter and Parker Solar Probe at different distances from the Sun may help us to resolve these ambiguities. Our general quasi-linear diffusion model applies to all non-relativistic collisionless plasmas, such as planetary magnetospheres (e.g. Mourenas et al., 2015). It also applies to other types of wave–

particle instabilities in plasmas such as the resonant instabilities driven by temperature anisotropy or by relative drift. We especially note that our model is capable of describing ion-driven instabilities.

In Chapter 4, we derive a gyro-averaged kinetic transport equation to describe the global expansion of the solar-wind electrons in a magnetic field that follows the Parker-spiral geometry. In the derivation of our kinetic transport equation, we rotate the reference frame co-moving with the solar wind to account for the Parker-spiral magnetic field. Based on Hamiltonian mechanics, we analyse the external electromagnetic forces and complete our kinetic transport equation. The derivation for our equation is independent of the derivation of the kinetic transport equation by Skilling (1971), Webb (1985), Isenberg (1997), le Roux et al. (2007), le Roux and Webb (2009), and Zank (2013).

We evaluate our kinetic transport equation to explain the electron-strahl evolution through the spherical expansion of the solar wind in the very inner heliosphere. This is especially of great importance for the understanding of the heat flux in the suprathermal part of the electron VDF. Therefore, we focus on the range of heliocentric distances between the collisional corona and the range of heliocentric distances up to $r/r_s = 20$, which has not yet been explored by in-situ spacecraft. We show that the solar-wind electrons evolve through the combined effects of the accelerating solar wind, ballistic particle streaming, the parallel (to the magnetic field) electric field, the magnetic mirror force, the Parker-spiral geometry, and Coulomb collisions. Our global kinetic evolution shows the formation of the electron strahl through ballistic particle streaming and the magnetic mirror force, a sunward shift of the electron core in velocity space through the interplanetary electric field, and a decrease of the electron density in agreement with the continuity equation for the electrons due to the spherically symmetric expansion. These results are in clear agreement with previous work on the kinetic electron evolution (Lie-Svendsen et al., 1997; Lie-Svendsen and Leer, 2000; Vocks and Mann, 2003; Smith et al., 2012; Landi et al., 2012; Tang et al., 2020; Berčič et al., 2021).

We apply a fitting routine to our numerical results for the comparison of the

electron core and strahl parameters with PSP observations. At around $r/r_s = 20$, the strahl density in our model is 7% of the total electron density, compared to 5% in typical observations from PSP (Abraham et al., 2021). The strahl parallel and perpendicular temperatures from our model are about 1.2 and 1.7 times greater while the core parallel and perpendicular temperatures from our model are 0.7 and 0.9 times less than the observed temperatures. The strahl bulk velocity in our model increases from $r/r_s = 5$ to $r/r_s = 15$ and then stays constant with distance at a value of about $U_s/v_{Ae0} = 5.6$ where $v_{Ae0} = 836\,\mathrm{km/s}$, which is close to the typically observed value. Both $\beta_{\|c}$ and $\beta_{\|s}$ are less than 1 in our region of interest. While $\beta_{\|s}$ stays nearly constant at around 0.02, $\beta_{\|c}$ steadily increases, approaching a value of $\beta_{\|c} \approx 0.11$ at $r/r_s = 20$. The comparison of our numerical results with PSP data suggests the necessity of an additional physical mechanism for the core parallel heating in our model. The electron Landau damping of kinetic Alfvén waves (Chen et al., 2019) can be a possible explanation for additional core parallel-heating mechanisms. Lastly, by comparing our results with the threshold for the oblique FM/W instability in the low-$\beta_{\|c}$ regime, we find that the electron strahl is not scattered by oblique FM/W instability for typical solar-wind conditions within $r/r_s = 20$.

Our global kinetic expansion model confirms the development of the core–strahl configuration in the electron VDF near the Sun. However, as discussed, this model presents us with open questions regarding the mechanisms for the core parallel heating and the stability of the electron strahl.

To confirm the above theoretical evidence about the electron strahl, we observationally analyse the stability of the electron strahl against the oblique FM/W instability for self-induced strahl scattering in two different $\beta_{\|c}$ regimes in Chapter 5. We evaluate the analytical instability thresholds as functions of heliocentric distance based on binned and averaged electron data from PSP and Helios. We find that the instability thresholds are not satisfied for the average solar wind at heliocentric distances between $25r_s$ and $210r_s$, and suggest that the strahl is not scattered by the oblique FM/W instability in the inner heliosphere on average. Even within the error bars in each bin, the strahl does not cross the instability threshold, suggesting

that the oblique FM/W instability plays a minor role, even in cases of "extreme" solar wind. Although our results are statistically robust, we recommend the numerical evaluation of the stability of individual distributions in the future to account for any uncertainties in the validity of the analytical expressions for the instability thresholds. To corroborate this finding, it is also important to investigate the occurrence rate of oblique FM/W waves in observations (Cattell et al., 2021) because their presence would be independent evidence for the occurrence of the oblique FM/W instability.

To numerically solve the two- and three-dimensional kinetic equations used in the research chapters, we devise a mathematical approach based on the Crank–Nicolson scheme in Chapter 6. We note that, in principle, this approach solves the general diffusion equation in any number of dimensions. However, if the computational capacity is limited, a simple numerical scheme, such as the Euler scheme, can be partially applied to our approach to reduce the amount of computations. We highlight that this approach can be used in different fields where multi-dimensional advection-diffusion equations are used.

7.2 Outlook

Our research clarifies how the electron strahl scattering by the oblique FM/W instability evolves on quasi-linear timescales, how the electron strahl and core populations form in the electron VDF during the expansion of the solar wind, and that the electron strahl is stable, on average, against the oblique FM/W instability in the inner heliosphere. In addition, this thesis provides an inventive mathematical approach for the required numerical analyses.

I identify three potential avenues for future work to follow up with the work presented in this thesis:

First, for a more complete description of the kinetic evolution of the electron VDF, we must combine our quasi-linear diffusion model and our global expansion model. Our expansion model for the electron VDF in Chapter 4 suggests the necessity for core parallel heating in the evolution of the electron VDF, which can

be realised by electron Landau damping of kinetic Alfvén waves. Even though our quasi-linear diffusion model itself can describe this damping locally, it must be included in a model for the full kinetic evolution. In addition, because other local wave–particle interactions such as the fan instability of the lower-hybrid mode (Krafft et al., 2005; Krafft and Volokitin, 2006; Shevchenko and Galinsky, 2010), the kinetic-Alfvén-wave (KAW) heat-flux instability (Gary et al., 1975), and the electrostatic heat-flux instability (Gary and Saito, 2007; Pavan et al., 2013) possibly occur in the solar wind, they must be included as well. Therefore, the fusion of these two models (local and global) is necessary. The difficulty of this work lies in the significantly different timescales associated with local quasi-linear diffusion and global kinetic expansion. Since the quasi-linear diffusion has a much shorter timescale, and is thus a local event, our global expansion model should consider an "occurrence condition" of the local quasi-linear diffusion so that the diffusion occurs in the model whenever its requirements are fulfilled.

Second, we must model the global kinetic expansion as in Chapter 4 up to large heliocentric distances (i.e., up to $\sim$1 au and potentially beyond) to numerically investigate the stability of the electron strahl. This numerical work can help us understand our data-based investigation of the strahl stability conducted in Chapter 5. The difficulty of this work lies in its very large demand in terms of computational resources to cover large heliocentric distances, while retaining the required spatial and velocity-space resolution. To overcome this difficulty, we require more advanced computers or develop a more efficient numerical scheme which reduces the amount of computations.

Third, to consolidate our data-based results of the strahl stability in Chapter 5, we must use more advanced numerical tools such as the ALPS (Verscharen and Chandran, 2018) or LEOPARD codes (Astfalk and Jenko, 2017). The analytical instability thresholds have uncertainties because they are based on some assumptions on the shape of the electron VDFs in their derivations. By solving the full hot-plasma dispersion relation via those tools, we can calculate the stability of individually measured electron VDFs, without assuming a bi-Maxwellian shape of the

electron VDF. This would help us clarify the role of non-bi-Maxwellian structures in the VDF for the driving of kinetic micro-instabilities.

Appendix A

Analysis of the Fokker–Planck Operator

A.1 Tensor Calculus in Cylindrical Velocity Space

The Fokker–Planck operator given in Eq. (1.61) is a tensor operator. In standard tensor notation, Eq (1.61) is

$$\left(\frac{\partial f_j}{\partial t}\right)_{\text{col}} = \sum_b \Gamma_{jb}\left\{4\pi\frac{m_j}{m_b}f_b f_j + H_b^{\alpha} f_{j,\alpha} + \frac{1}{2}G_b^{\alpha\beta} f_{j,\alpha\beta}\right\}, \tag{A.1}$$

Therefore, we must first find the form of Eq. (A.1) in cylindrical velocity space covering the original Euclidean space.

For an arbitrary scalar X in our tensor framework, X_α and $X_{\alpha\beta}$ indicate the first and second covariant derivatives, and

$$X^{\alpha} = g^{\alpha I} X_I, \tag{A.2}$$

$$X^{\alpha\beta} = g^{\alpha I} g^{\beta J} X_{IJ} \tag{A.3}$$

where g^{IJ} is the contravariant fundamental tensor. Since our space is Euclidean, the Riemann–Christoffel tensor is zero, and the order of differentiation is not important. An element of length in the Euclidean, cylindrical velocity space is

$$ds^2 = dv_\perp^2 + v_\perp^2 d\phi^2 + dv_\parallel^2. \tag{A.4}$$

Then, the fundamental tensor is given as

$$g_{\alpha\beta} \equiv \begin{bmatrix} 1 & 0 & 0 \\ 0 & v_\perp^2 & 0 \\ 0 & 0 & 1 \end{bmatrix}_{3\times 3}, \tag{A.5}$$

and the contravariant fundamental tensor is

$$g^{\alpha\beta} \equiv \begin{bmatrix} 1 & 0 & 0 \\ 0 & \frac{1}{v_\perp^2} & 0 \\ 0 & 0 & 1 \end{bmatrix}_{3\times 3}. \tag{A.6}$$

For a tensor $X_{\alpha\beta}$, we have the relation

$$X_{\alpha\beta} = \frac{\partial X_\alpha}{\partial X^\beta} - \Gamma^I_{\alpha\beta} X_I \tag{A.7}$$

where

$$\Gamma^I_{\alpha\beta} = \frac{1}{2} g^{IJ} \left(\frac{\partial g_{\alpha J}}{\partial X^\beta} + \frac{\partial g_{\beta J}}{\partial X^\alpha} - \frac{\partial g_{\alpha\beta}}{\partial X^J} \right) = \Gamma^I_{\beta\alpha}, \tag{A.8}$$

which is a Christoffel symbol of the second kind. By using Eqs. (A.5) and (A.6), and setting $X^1 = v_\perp$, $X^2 = \phi$ and $X^3 = v_\parallel$, the Christoffel symbols in the cylindrical velocity space are given as

$$\Gamma^I_{11} = 0 \ \text{ for } \ I = 1,\ 2,\ 3, \tag{A.9}$$

$$\Gamma^I_{12} = \Gamma^I_{21} = \begin{cases} 0, & I = 1, \\ \frac{1}{v_\perp}, & I = 2, \\ 0, & I = 3, \end{cases} \tag{A.10}$$

$$\Gamma^I_{13} = \Gamma^I_{31} = 0 \ \text{ for } \ I = 1,\ 2,\ 3, \tag{A.11}$$

$$\Gamma^I_{22} = \begin{cases} -v_\perp, & I = 1, \\ 0, & I = 2, \\ 0, & I = 3, \end{cases} \tag{A.12}$$

$$\Gamma^I_{23} = \Gamma^I_{32} = 0 \ \text{ for } \ I = 1,\ 2,\ 3, \tag{A.13}$$

and

$$\Gamma^I_{33} = 0 \ \text{ for } \ I = 1,\ 2,\ 3. \tag{A.14}$$

In our analysis for Eq (A.1), we assume that f_b and f_j are gyrotropic. Therefore, the partial derivative with respect to ϕ is zero. In the cylindrical velocity space, the first covariant derivatives of H_b are given as

$$H_{b,1} = \frac{\partial H_b}{\partial v_\perp}, \tag{A.15}$$

$$H_{b,2} = 0, \tag{A.16}$$

and

$$H_{b,3} = \frac{\partial H_b}{\partial v_\parallel}. \tag{A.17}$$

By the same logic, the first covariant derivatives of f_j are given as

$$f_{j,1} = \frac{\partial f_j}{\partial v_\perp}, \tag{A.18}$$

$$f_{j,2} = 0, \tag{A.19}$$

and

$$f_{j,3} = \frac{\partial f_j}{\partial v_\parallel}. \tag{A.20}$$

By using Eq. (A.2) and Eq. (A.6), we have

$$H^1_b = \frac{\partial H_b}{\partial v_\perp}, \tag{A.21}$$

$$H^2_b = 0, \tag{A.22}$$

and

$$H_b^3 = \frac{\partial H_b}{\partial v_\parallel}. \tag{A.23}$$

Then, through Eqs. (A.18) to (A.23), the second term in the bracket on the right-hand side of Eq. (A.1) becomes

$$H_b^\alpha f_{j,\alpha} = \frac{\partial H_b}{\partial v_\perp}\frac{\partial f_j}{\partial v_\perp} + \frac{\partial H_b}{\partial v_\parallel}\frac{\partial f_j}{\partial v_\parallel}. \tag{A.24}$$

By using Eqs. (A.5) through (A.14), the second covariant derivatives of G_b are given as

$$G_{b,11} = \frac{\partial^2 G_b}{\partial v_\perp^2}, \tag{A.25}$$

$$G_{b,12} = G_{b,21} = 0, \tag{A.26}$$

$$G_{b,13} = G_{b,31} = \frac{\partial^2 G_b}{\partial v_\parallel \partial v_\perp}, \tag{A.27}$$

$$G_{b,22} = v_\perp \frac{\partial G_b}{\partial v_\perp}, \tag{A.28}$$

$$G_{b,23} = G_{b,32} = 0, \tag{A.29}$$

and

$$G_{b,33} = \frac{\partial^2 G_b}{\partial v_\parallel^2}. \tag{A.30}$$

By the same logic, the second covariant derivatives of f_j are given as

$$f_{j,11} = \frac{\partial^2 f_j}{\partial v_\perp^2}, \tag{A.31}$$

$$f_{j,12} = f_{j,21} = 0, \tag{A.32}$$

$$f_{j,13} = f_{j,31} = \frac{\partial^2 f_j}{\partial v_\parallel \partial v_\perp}, \tag{A.33}$$

$$f_{j,22} = v_\perp \frac{\partial f_j}{\partial v_\perp}, \tag{A.34}$$

$$f_{j,23} = f_{j,32} = 0, \tag{A.35}$$

and

$$f_{j,33} = \frac{\partial^2 f_j}{\partial v_\parallel^2}. \tag{A.36}$$

Using Eq. (A.3) and Eq. (A.6), we obtain

$$G_b^{11} = \frac{\partial^2 G_b}{\partial v_\perp^2}, \tag{A.37}$$

$$G_b^{12} = G_b^{21} = 0, \tag{A.38}$$

$$G_b^{13} = G_b^{31} = \frac{\partial^2 G_b}{\partial v_\parallel \partial v_\perp}, \tag{A.39}$$

$$G_b^{22} = \frac{1}{v_\perp^3}\frac{\partial G_b}{\partial v_\perp}, \tag{A.40}$$

$$G_b^{23} = G_b^{32} = 0, \tag{A.41}$$

and

$$G_b^{33} = \frac{\partial^2 G_b}{\partial v_\parallel^2}. \tag{A.42}$$

Then, with Eqs. (A.31) through (A.42), the third term in the bracket on the right-hand side of Eq. (A.1) becomes

$$G_b^{\alpha\beta} f_{j,\alpha\beta} = \frac{\partial^2 G_b}{\partial v_\perp^2}\frac{\partial^2 f_j}{\partial v_\perp^2} + 2\frac{\partial^2 G_b}{\partial v_\parallel \partial v_\perp}\frac{\partial^2 f_j}{\partial v_\parallel \partial v_\perp} + \frac{1}{v_\perp^2}\frac{\partial G_b}{\partial v_\perp}\frac{\partial f_j}{\partial v_\perp} + \frac{\partial^2 G_b}{\partial v_\parallel^2}\frac{\partial^2 f_j}{\partial v_\parallel^2}. \tag{A.43}$$

Upon substituting Eqs. (A.24) and (A.43) into Eq. (A.1), we obtain (Vocks, 2002)

$$\begin{aligned}\left(\frac{\partial f_j}{\partial t}\right)_{\text{col}} = \sum_b \Gamma_{jb} \Bigg(& 4\pi\frac{m_j}{m_b} f_b f_j + \frac{\partial H_b}{\partial v_\perp}\frac{\partial f_j}{\partial v_\perp} + \frac{\partial H_b}{\partial v_\parallel}\frac{\partial f_j}{\partial v_\parallel} + \frac{1}{2v_\perp^2}\frac{\partial G_b}{\partial v_\perp}\frac{\partial f_j}{\partial v_\perp} \\ & + \frac{1}{2}\frac{\partial^2 G_b}{\partial v_\perp^2}\frac{\partial^2 f_j}{\partial v_\perp^2} + \frac{\partial^2 G_b}{\partial v_\parallel \partial v_\perp}\frac{\partial^2 f_j}{\partial v_\parallel \partial v_\perp} + \frac{1}{2}\frac{\partial^2 G_b}{\partial v_\parallel^2}\frac{\partial^2 f_j}{\partial v_\parallel^2} \Bigg).\end{aligned} \tag{A.44}$$

We use Eq. (A.44) for the Coulomb collision operator throughout our study.

A.2 Rosenbluth Potential Analysis for Maxwellian VDFs

In our analysis, we treat the Rosenbluth potentials with the collisional background particles which have gyrotropic and Maxwellian VDFs,

$$f_b(v) = \frac{n_b}{\pi^{3/2} v_{th,b}^3} \exp\left(-\frac{v^2}{v_{th,b}^2}\right), \tag{A.45}$$

where $v^2 = v_\perp^2 + v_\parallel^2$. Using Eq. (A.45) and the identities

$$\int \frac{\exp(-\mathbf{x}^2)}{|\mathbf{x}-\mathbf{y}|} d^3\mathbf{x} = \frac{\pi^{3/2}}{\mathbf{y}} \operatorname{erf}(\mathbf{y}) \tag{A.46}$$

and

$$\int \exp(-\mathbf{x}^2)|\mathbf{x}-\mathbf{y}| d^3\mathbf{x} = \frac{\pi^{3/2}}{2\mathbf{y}} \left[\frac{2\mathbf{y}}{\sqrt{\pi}} \exp(-\mathbf{y}^2) + (1+2\mathbf{y}^2)\operatorname{erf}(\mathbf{y})\right], \tag{A.47}$$

we calculate Eqs. (1.58) and (1.59), and obtain

$$G_b(v) = \pi v_{th,b}^4 f_b + n_b \frac{v_{th,b}^2 + 2v^2}{2v} \operatorname{erf}\left(\frac{v}{v_{th,b}}\right) \tag{A.48}$$

and

$$H_b(v) = \frac{m_b - m_j}{m_b} \frac{n_b}{v} \operatorname{erf}\left(\frac{v}{v_{th,b}}\right), \tag{A.49}$$

where

$$\operatorname{erf}(z) = \frac{2}{\sqrt{\pi}} \int_0^z \exp(-z'^2) dz'. \tag{A.50}$$

Note that Eqs. (A.48) and (A.49) are valid at $v = 0$ because

$$\lim_{z\to\infty} \frac{\operatorname{erf}(z)}{z} = \frac{2}{\sqrt{\pi}}. \tag{A.51}$$

However, in numerical calculations, it is not possible to satisfy Eq. (A.51). Thus, for the case with small values of $v/v_{th,b}$ in Eqs. (A.48) and (A.49), we use a Taylor expansion at $v/v_{th,b} = 0$. Through the Taylor expansion of $(v_{th,b}/v)\operatorname{erf}(v/v_{th,b})$ at

$v/v_{th,b} = 0$ to second order, we obtain

$$\frac{v_{th,b}}{v}\,\mathrm{erf}\left(\frac{v}{v_{th,b}}\right) \approx \frac{2}{\sqrt{\pi}} - \frac{2}{3\sqrt{\pi}}\left(\frac{v}{v_{th,b}}\right)^2 + \frac{1}{5\sqrt{\pi}}\left(\frac{v}{v_{th,b}}\right)^4. \tag{A.52}$$

By applying Eq. (A.52) to Eqs. (A.48) and (A.49), we obtain the coefficients of Eq. (A.44) as follow:

$$\frac{\partial G_b}{\partial v_\perp} = \begin{cases} \frac{\pi v_{th,b}^4 v_\perp}{v^2} f_b + n_b \frac{(2v^2 - v_{th,b}^2)v_\perp}{2v^3}\,\mathrm{erf}\left(\frac{v}{v_{th,b}}\right) & \text{if } \frac{v}{v_{th,b}} \geq 1, \\ n_b \frac{2v_\perp}{\sqrt{\pi} v_{th,b}} \left[\frac{2}{3} - \frac{2v^2}{15v_{th,b}^2} + \frac{v^4}{10v_{th,b}^4}\right] & \text{if } \frac{v}{v_{th,b}} < 1, \end{cases} \tag{A.53}$$

$$\frac{\partial^2 G_b}{\partial v_\parallel^2} = \begin{cases} \frac{\pi(v^2 - 3v_\parallel^2)v_{th,b}^4}{v^4} f_b + n_b \frac{2v^4 - 2v_\parallel^2 v^2 - (v^2 - 3v_\parallel^2)v_{th,b}^2}{2v^5}\,\mathrm{erf}\left(\frac{v}{v_{th,b}}\right) & \text{if } \frac{v}{v_{th,b}} \geq 1, \\ n_b \frac{2}{\sqrt{\pi} v_{th,b}} \left[\frac{2}{3} - \frac{2(v^2 + 2v_\parallel^2)}{15v_{th,b}^2} + \frac{(v^2 + 4v_\parallel^2)v^2}{10v_{th,b}^4}\right] & \text{if } \frac{v}{v_{th,b}} < 1, \end{cases} \tag{A.54}$$

$$\frac{\partial^2 G_b}{\partial v_\perp^2} = \begin{cases} \frac{\pi(v^2 - 3v_\perp^2)v_{th,b}^4}{v^4} f_b + n_b \frac{2v^4 - 2v_\perp^2 v^2 - (v^2 - 3v_\perp^2)v_{th,b}^2}{2v^5}\,\mathrm{erf}\left(\frac{v}{v_{th,b}}\right) & \text{if } \frac{v}{v_{th,b}} \geq 1, \\ n_b \frac{2}{\sqrt{\pi} v_{th,b}} \left[\frac{2}{3} - \frac{2(v^2 + 2v_\perp^2)}{15v_{th,b}^2} + \frac{(v^2 + 4v_\perp^2)v^2}{10v_{th,b}^4}\right] & \text{if } \frac{v}{v_{th,b}} < 1, \end{cases} \tag{A.55}$$

$$\frac{\partial^2 G_b}{\partial v_\perp \partial v_\parallel} = \begin{cases} -\frac{3\pi v_\perp v_\parallel v_{th,b}^4}{v^4} f_b + n_b \frac{v_\perp v_\parallel}{v^3} \left[\frac{3v_{th,b}^2}{2v^2} - 1\right] \mathrm{erf}\left(\frac{v}{v_{th,b}}\right) & \text{if } \frac{v}{v_{th,b}} \geq 1, \\ n_b \frac{4v_\perp v_\parallel}{5\sqrt{\pi} v_{th,b}^3} \left[\frac{v^2}{v_{th,b}^2} - \frac{2}{3}\right] & \text{if } \frac{v}{v_{th,b}} < 1, \end{cases} \tag{A.56}$$

$$\frac{\partial H_b}{\partial v_\parallel} = \begin{cases} \frac{m_b - m_j}{m_b} \left[2\pi \frac{v_\parallel v_{th,b}^2}{v^2} f_b - n_b \frac{v_\parallel}{v^3}\,\mathrm{erf}\left(\frac{v}{v_{th,b}}\right)\right] & \text{if } \frac{v}{v_{th,b}} \geq 1, \\ n_b \frac{m_b - m_j}{m_b} \frac{4}{\sqrt{\pi}} \frac{v_\parallel}{v_{th,b}^3} \left[-\frac{1}{3} + \frac{1}{5}\frac{v^2}{v_{th,b}^2}\right] & \text{if } \frac{v}{v_{th,b}} < 1, \end{cases} \tag{A.57}$$

and

$$\frac{\partial H_b}{\partial v_\perp} = \begin{cases} \frac{m_b - m_j}{m_b} \left[2\pi \frac{v_\perp v_{th,b}^2}{v^2} f_b - n_b \frac{v_\perp}{v^3}\,\mathrm{erf}\left(\frac{v}{v_{th,b}}\right)\right] & \text{if } \frac{v}{v_{th,b}} \geq 1, \\ n_b \frac{m_b - m_j}{m_b} \frac{4}{\sqrt{\pi}} \frac{v_\perp}{v_{th,b}^3} \left[-\frac{1}{3} + \frac{1}{5}\frac{v^2}{v_{th,b}^2}\right] & \text{if } \frac{v}{v_{th,b}} < 1. \end{cases} \tag{A.58}$$

We then apply Eqs. (A.53) through (A.58) to Eq. (A.44) in our evaluation of the Fokker–Planck collision operator.

Appendix B

Smoothing Effect in Velocity Space

Fig. B.1 shows the results for the kinetic evolution of the electron VDF calculated with our numerical treatment described in section 4.3. However, the result shown in Fig. B.1 does not include the smoothing defined in Eq. (4.63), while Fig. 4.2 does.

In the top-right corner of Fig. B.1b, numerical errors occur at very low values of the VDF. Comparing Fig. B.1 with Fig. 4.2, our smoothing scheme, Eq. (4.63), only cleans out these numerical errors without changing other parts of the electron VDF. Using the fitting scheme from section 4.4.2, the fit parameters for the VDF shown in Fig. B.1b are $n_c/n_e = 0.93$, $n_s/n_e = 0.07$, $T_{\|c} = 0.31 \times 10^6 K$, $T_{\perp c}(10^6 K) = 0.35$, $T_{\|s} = 0.89 \times 10^6 K$, $T_{\perp s} = 0.54 \times 10^6 K$, $U_c/v_{Ae0} = -0.18$ and $U_s/v_{Ae0} = 5.59$. These fit parameters are identical to the fit parameters from Fig. 4.2b (see Fig. 4.5b). These errors are due to the limited velocity resolution and grow over time.

We conclude that Eq. (4.63) is an appropriate method to improve the numerical stability of our algorithm without affecting the physics captured in our model.

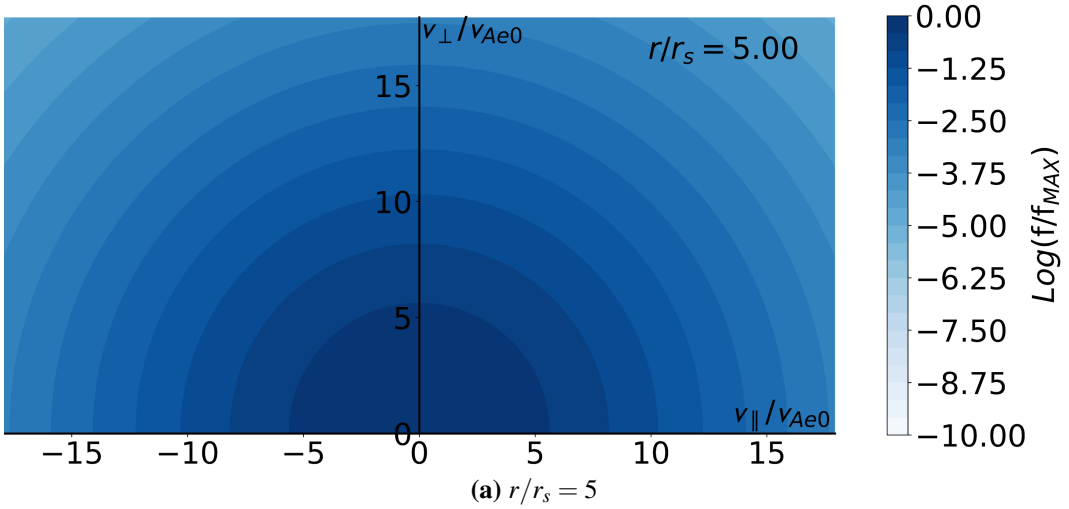

(a) $r/r_s = 5$

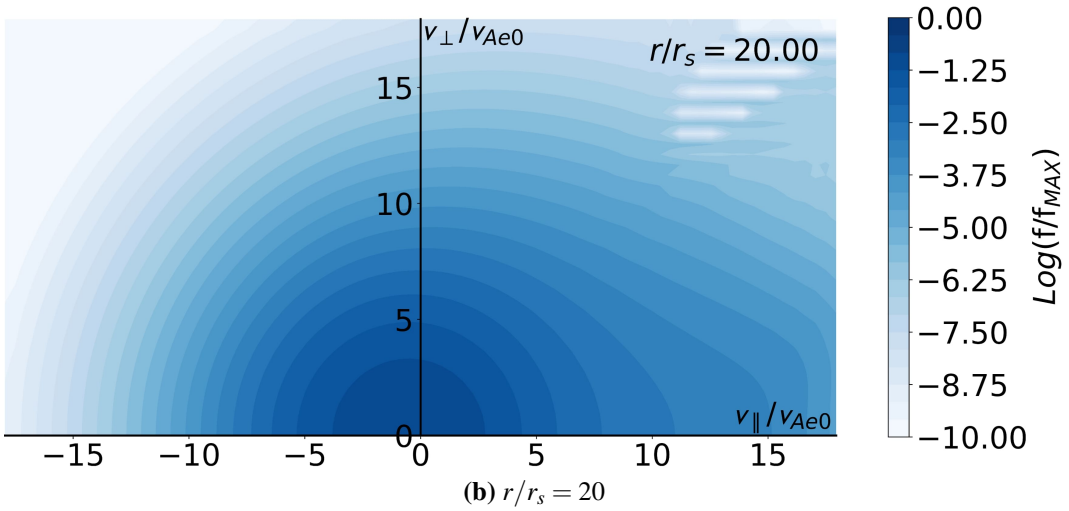

(b) $r/r_s = 20$

Figure B.1: Numerical results without averaging through Eq. (4.63) in velocity space. Due to the limited velocity resolution, the numerical errors occur on the top-right corner in Fig. B.1b. Panels (a) and (b) show the initial and final snapshot of the animation.

Appendix C

Logarithmic Radial Profiles

The radial profiles in the linear scale given in Chapter 5 are more convenient for the calculation with Eqs. (5.2) and (5.3), which is our main goal of Chapter 5. As another perspective, the radial profiles in the logarithmic scale would be good to investigate the power-law behaviour of plasma parameters. Therefore, in this chapter, we provide the logarithmic version of the radial profiles shown in Chapter 5. Note that both linear and logarithmic versions provide the same physics conclusion in Chapter 5.

We apply the logarithmic scale (i.e. $\log_{10}$) to the radial profiles shown in Chapter 5. The radial (horizontal) axis in the following figures ranges from $10^{1.40} r/r_s$ to $10^{2.35} r/r_s$.

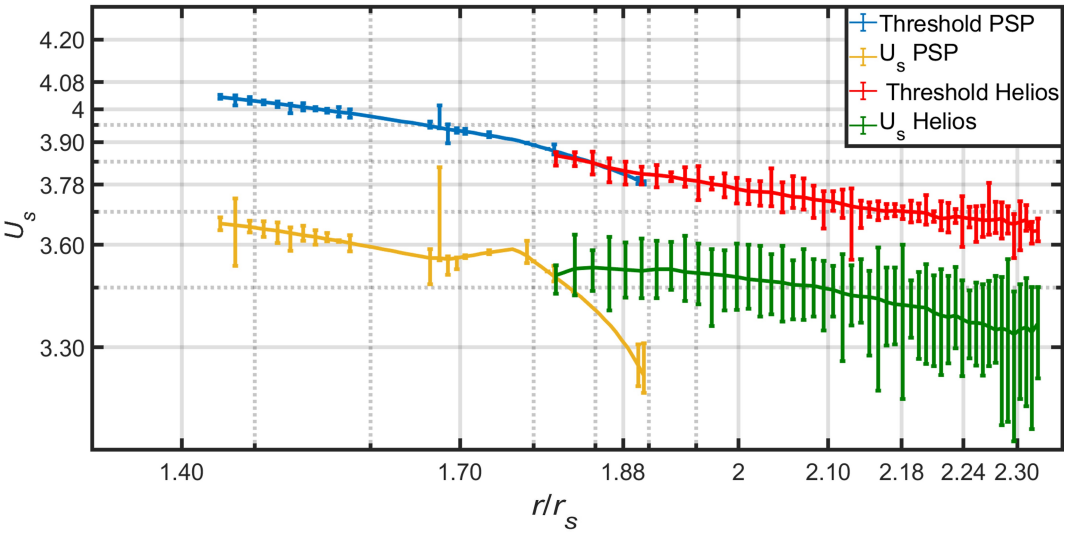

Figure C.1: Logarithmic profiles of the low-$\beta_{\|c}$ threshold of the oblique FM/W instability from Eq. (5.2) and U_s as functions of heliocentric distance. All PSP and Helios data underlying this figure have $\beta_{\|c} < 0.25$. The vertical axis ranges from $10^{3.20}$ km/s to $10^{4.20}$ km/s.

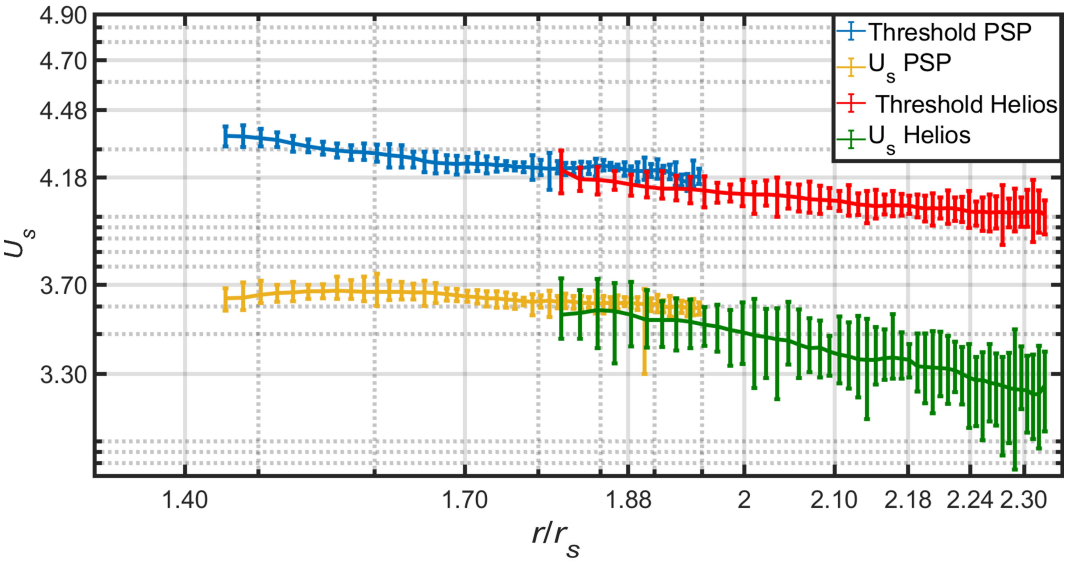

Figure C.2: Logarithmic profiles of the high-$\beta_{\|c}$ threshold of the oblique FM/W instability from Eq. (5.3) and U_s as functions of heliocentric distance. All PSP and Helios data underlying this figure have $\beta_{\|c} > 0.25$. The vertical axis ranges from $10^{3.10}$ km/s to $10^{4.90}$ km/s.

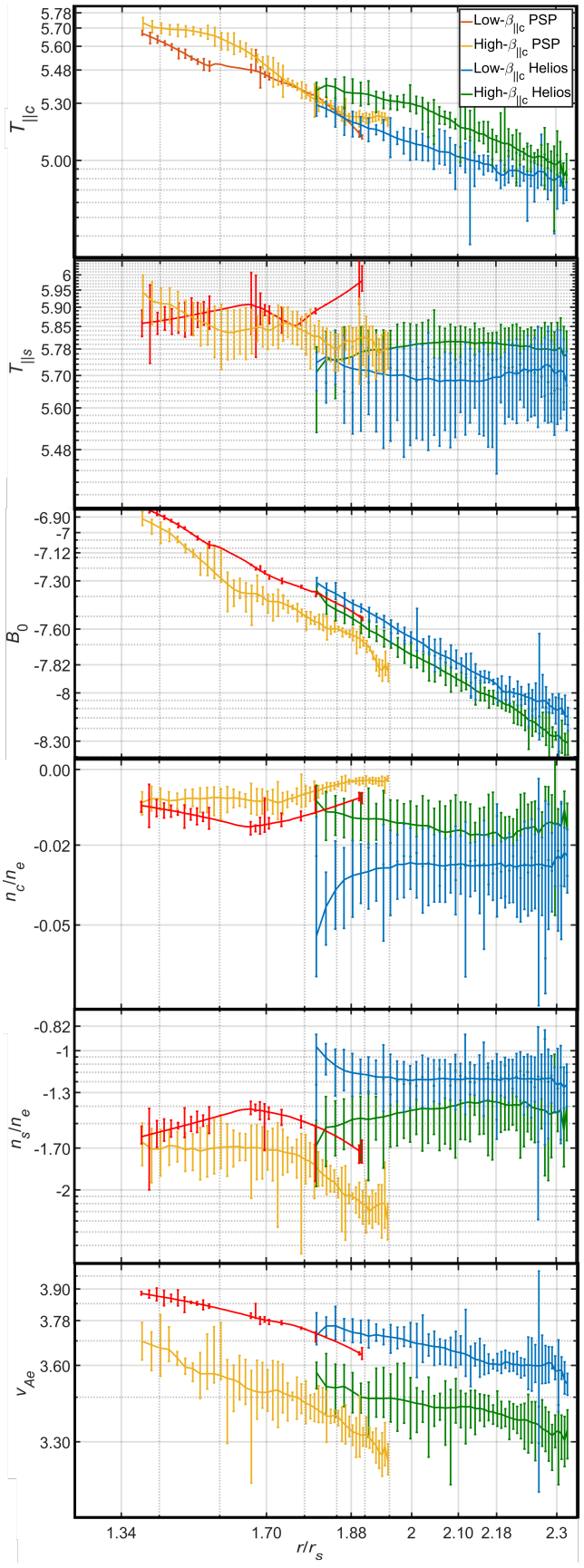

Figure C.3: Logarithmic radial profiles of $T_{\|c}$, $T_{\|s}$, $|\mathbf{B}_0|$, n_c/n_e, n_s/n_e and v_{Ae} in our PSP and Helios datasets, separated between the low-$\beta_{\|c}$ and the high-$\beta_{\|c}$ regimes. The vertical axes of $T_{\|c}$, $T_{\|s}$, $|\mathbf{B}_0|$, n_c/n_e, n_s/n_e and v_{Ae} range from $10^{4.70}$ K to $10^{5.80}$ K, from $10^{5.30}$ K to $10^{6.1}$ K, from $10^{-8.20}$ T to $10^{-6.8}$ T, from $10^{-0.07}$ to 10^{0}, from $10^{-2.4}$ to $10^{-0.82}$, and from $10^{3.2}$ km/s to 10^{4} km/s, respectively.

Bibliography

Abraham, J. B., Owen, C. J., Verscharen, D., Bakrania, M., Stansby, D., Wicks, R. T., Nicolaou, G., Agudelo Rueda, J. A., Jeong, S. Y., Whittlesey, P. L., and Berčič, L. (2021). Radial evolution of thermal and suprathermal electron populations in the slow solar wind from 0.13 to 0.5 au using Machine learning: Parker Solar Probe Observations. .

Albert, J. M. (2004). Using quasi-linear diffusion to model acceleration and loss from wave-particle interactions. *Space Weather*, 2(9).

Astfalk, P. and Jenko, F. (2017). Leopard: A grid-based dispersion relation solver for arbitrary gyrotropic distributions. *Journal of Geophysical Research: Space Physics*, 122(1):89–101.

Badman, S. T., Bale, S. D., Rouillard, A. P., Bowen, T. A., Bonnell, J. W., Goetz, K., Harvey, P. R., MacDowall, R. J., Malaspina, D. M., and Pulupa, M. (2021). Measurement of the open magnetic flux in the inner heliosphere down to 0.13 AU. , 650:A18.

Bale, S. D., Pulupa, M., Salem, C., Chen, C. H. K., and Quataert, E. (2013). Electron Heat Conduction in the Solar Wind: Transition from Spitzer-Härm to the Collisionless Limit. , 769(2):L22.

Bemporad, A. (2017). Exploring the inner acceleration region of solar wind: A study based on coronagraphic UV and visible light data. *The Astrophysical Journal*, 846(1):86.

Berčič, L., Maksimović, M., Halekas, J. S., Landi, S., Owen, C. J., Verscharen, D., Larson, D., Whittlesey, P., Badman, S. T., Bale, S. D., Case, A. W., Goetz, K., Harvey, P. R., Kasper, J. C., Korreck, K. E., Livi, R., MacDowall, R. J., Malaspina, D. M., Pulupa, M., and Stevens, M. L. (2021). Ambipolar electric field and potential in the solar wind estimated from electron velocity distribution functions. 921(1):83.

Berčič, L., Maksimović, , M., Landi, S., and Matteini, L. (2019). Scattering of strahl electrons in the solar wind between 0.3 and 1 au: Helios observations. , 486(3):3404–3414.

Berčič, L., Landi, S., and Maksimović, M. (2021). The interplay between ambipolar electric field and coulomb collisions in the solar wind acceleration region. *Journal of Geophysical Research: Space Physics*, 126(3):e2020JA028864. e2020JA028864 2020JA028864.

Boldyrev, S., Forest, C., and Egedal, J. (2020). Electron temperature of the solar wind. *Proceedings of the National Academy of Sciences*, 117(17):9232–9240.

Boldyrev, S. and Horaites, K. (2019). Kinetic theory of the electron strahl in the solar wind. , 489(3):3412–3419.

Borovsky, J. E. (2012). Looking for evidence of mixing in the solar wind from 0.31 to 0.98 AU. *Journal of Geophysical Research (Space Physics)*, 117(A6):A06107.

Bravo, S. and Stewart, G. A. (1997). Fast and Slow Wind from Solar Coronal Holes. , 489(2):992–999.

Brügmann, B., Tichy, W., and Jansen, N. (2004). Numerical simulation of orbiting black holes. *Physical Review Letters*, 92(21).

Cattell, C., Breneman, A., Dombeck, J., Hanson, E., Johnson, M., Halekas, J., Bale, S. D., de Wit, T. D., Goetz, K., Goodrich, K., Malaspina, D., Pulupa, M., Case, T., Kasper, J. C., Larson, D., Stevens, M., and Whittlesey, P. (2021). No whistler waves near the sun: what regulates the heat flux close to the sun?

Chen, C. H. K., Klein, K. G., and Howes, G. G. (2019). Evidence for electron Landau damping in space plasma turbulence. *Nature Communications*, 10:740.

Chen, W. M., Lai, C. S., Lin, H. E., and Lin, W. C. (1972). Collisionless solar wind in the spiral magnetic field. *Journal of Geophysical Research (1896-1977)*, 77(1):1–11.

Cranmer, S. R. (2020). Updated measurements of proton, electron, and oxygen temperatures in the fast solar wind. *Research Notes of the AAS*, 4(12):249.

Ebert, R. W., McComas, D. J., Elliott, H. A., Forsyth, R. J., and Gosling, J. T. (2009). Bulk properties of the slow and fast solar wind and interplanetary coronal mass ejections measured by ulysses: Three polar orbits of observations. *Journal of Geophysical Research: Space Physics*, 114(A1).

Feldman, U., Landi, E., and Schwadron, N. A. (2005). On the sources of fast and slow solar wind. *Journal of Geophysical Research: Space Physics*, 110(A7).

Feldman, W. C., Anderson, R. C., Bame, S. J., Gosling, J. T., Zwickl, R. D., and Smith, E. J. (1983). Electron velocity distributions near interplantary shocks. *Journal of Geophysical Research: Space Physics*, 88(A12):9949–9958.

Feldman, W. C., Asbridge, J. R., Bame, S. J., Montgomery, M. D., and Gary, S. P. (1975). Solar wind electrons. *Journal of Geophysical Research (1896-1977)*, 80(31):4181–4196.

Fitzenreiter, R. J., Ogilvie, K. W., Bale, S. D., and Viñas, A. F. (2003). Modification of the solar wind electron velocity distribution at interplanetary shocks. *Journal of Geophysical Research: Space Physics*, 108(A12).

Gary, S. P., Feldman, W. C., Forslund, D. W., and Montgomery, M. D. (1975). Electron heat flux instabilities in the solar wind. *Geophysical Research Letters*, 2(3):79–82.

Gary, S. P. and Saito, S. (2007). Broadening of solar wind strahl pitch-angles by the electron/electron instability: Particle-in-cell simulations. *Geophysical Research Letters*, 34(14).

Gary, S. P., Saito, S., and Li, H. (2008). Cascade of whistler turbulence: Particle-in-cell simulations. *Geophysical Research Letters*, 35(2).

Gendrin, R. (1968). Pitch angle diffusion of low energy protons due to gyroresonant interaction with hydromagnetic waves. *Journal of Atmospheric and Terrestrial Physics*, 30(7):1313–1330.

Gendrin, R. (1981). General relationships between wave amplification and particle diffusion in a magnetoplasma. *Reviews of Geophysics*, 19(1):171–184.

Gendrin, R. and Roux, A. (1980). Energization of helium ions by proton-induced hydromagnetic waves. *Journal of Geophysical Research: Space Physics*, 85(A9):4577–4586.

Gilat, A. and Subramaniam, V. V. (2011). *Numerical methods : an introduction with applications using MATLAB*. Wiley Publishing.

Glauert, S. A. and Horne, R. B. (2005). Calculation of pitch angle and energy diffusion coefficients with the padie code. *Journal of Geophysical Research: Space Physics*, 110(A4).

Graham, G. A., Rae, I. J., Owen, C. J., Walsh, A. P., Arridge, C. S., Gilbert, L., Lewis, G. R., Jones, G. H., Forsyth, C., Coates, A. J., and Waite, J. H. (2017). The evolution of solar wind strahl with heliospheric distance. *Journal of Geophysical Research: Space Physics*, 122(4):3858–3874.

Gurgiolo, C. and Goldstein, M. L. (2016). Observations of diffusion in the electron halo and strahl. *Annales Geophysicae*, 34(12):1175–1189.

Gurgiolo, C., Goldstein, M. L., Viñas, A. F., and Fazakerley, A. N. (2012). Direct observations of the formation of the solar wind halo from the strahl. *Annales Geophysicae*, 30(1):163–175.

Gurnett, D. A. and Bhattacharjee, A. (2017). Introduction to plasma physics: With space, laboratory and astrophysical applications.

Halekas, J. S., Whittlesey, P. L., Larson, D. E., McGinnis, D., Bale, S. D., Berthomier, M., Case, A. W., Chandran, B. D. G., Kasper, J. C., Klein, K. G., Korreck, K. E., Livi, R., MacDowall, R. J., Maksimovic, M., Malaspina, D. M., Matteini, L., Pulupa, M. P., and Stevens, M. L. (2021). Electron heat flux in the near-sun environment. *A&A*, 650:A15.

Hellinger, P., Trávníček, P. M., Štverák, , Matteini, L., and Velli, M. (2013). Proton thermal energetics in the solar wind: Helios reloaded. *Journal of Geophysical Research: Space Physics*, 118(4):1351–1365.

Heuer, M. and Marsch, E. (2007). Diffusion plateaus in the velocity distributions of fast solar wind protons. *Journal of Geophysical Research: Space Physics*, 112(A3).

Horaites, K., Astfalk, P., Boldyrev, S., and Jenko, F. (2018a). Stability analysis of core-strahl electron distributions in the solar wind. , 480(2):1499–1506.

Horaites, K., Boldyrev, S., and Medvedev, M. V. (2019). Electron strahl and halo formation in the solar wind. , 484(2):2474–2481.

Horaites, K., Boldyrev, S., Wilson, Lynn B., I., Viñas, A. F., and Merka, J. (2018b). Kinetic Theory and Fast Wind Observations of the Electron Strahl. , 474(1):115–127.

Isenberg, P. and Vasquez, B. (2011). A kinetic model of solar wind generation by oblique ion-cyclotron waves. *The Astrophysical Journal*, 731:88.

Isenberg, P. A. (1997). A hemispherical model of anisotropic interstellar pickup ions. *Journal of Geophysical Research: Space Physics*, 102(A3):4719–4724.

Isenberg, P. A. and Lee, M. A. (1996). A dispersive analysis of bispherical pickup ion distributions. *Journal of Geophysical Research: Space Physics*, 101(A5):11055–11066.

Iserles, A. (2008). A first course in the numerical analysis of differential equations.

Jeong, S.-Y., Abraham, J. B., Verscharen, D., Berčič, L., Stansby, D., Nicolaou, G., Owen, C. J., Wicks, R. T., Fazakerley, A. N., Rueda, J. A. A., and Bakrania, M. (2022a). The stability of the electron strahl against the oblique fast-magnetosonic/whistler instability in the inner heliosphere. *The Astrophysical Journal Letters*, 926(2):L26.

Jeong, S.-Y., Verscharen, D., Vocks, C., Abraham, J. B., Owen, C. J., Wicks, R. T., Fazakerley, A. N., Stansby, D., Berčič, L., Nicolaou, G., Rueda, J. A. A., and Bakrania, M. (2022b). The kinetic expansion of solar-wind electrons: Transport theory and predictions for the very inner heliosphere. *The Astrophysical Journal*, 927(2):162.

Jeong, S.-Y., Verscharen, D., Wicks, R. T., and Fazakerley, A. N. (2020). A quasi-linear diffusion model for resonant wave–particle instability in homogeneous plasma. *The Astrophysical Journal*, 902(2):128.

Jockers, K. (1970). Solar Wind Models Based on Exospheric Theory. , 6:219.

Kasper, J. C., Abiad, R., Austin, G., Balat-Pichelin, M., Bale, S. D., Belcher, J. W., Berg, P., Bergner, H., Berthomier, M., Bookbinder, J., Brodu, E., Caldwell, D., Case, A. W., Chandran, B. D. G., Cheimets, P., Cirtain, J. W., Cranmer, S. R., Curtis, D. W., Daigneau, P., Dalton, G., Dasgupta, B., DeTomaso, D., Diaz-Aguado, M., Djordjevic, B., Donaskowski, B., Effinger, M., Florinski, V., Fox, N., Freeman, M., Gallagher, D., Gary, S. P., Gauron, T., Gates, R., Goldstein, M., Golub, L., Gordon, D. A., Gurnee, R., Guth, G., Halekas, J., Hatch, K., Heerikuisen, J., Ho, G., Hu, Q., Johnson, G., Jordan, S. P., Korreck, K. E., Larson, D., Lazarus, A. J., Li, G., Livi, R., Ludlam, M., Maksimovic, M., McFadden, J. P., Marchant, W., Maruca, B. A., McComas, D. J., Messina, L., Mercer, T., Park, S., Peddie, A. M., Pogorelov, N., Reinhart, M. J., Richardson, J. D., Robinson, M., Rosen, I., Skoug, R. M., Slagle, A., Steinberg, J. T., Stevens, M. L., Szabo, A., Taylor, E. R., Tiu, C., Turin, P., Velli, M., Webb, G., Whittlesey, P.,

Wright, K., Wu, S. T., and Zank, G. (2016). Solar Wind Electrons Alphas and Protons (SWEAP) Investigation: Design of the Solar Wind and Coronal Plasma Instrument Suite for Solar Probe Plus. , 204(1-4):131–186.

Kennel, C. F. and Engelmann, F. (1966). Velocity Space Diffusion from Weak Plasma Turbulence in a Magnetic Field. *Physics of Fluids*, 9(12):2377–2388.

Kennel, C. F. and Wong, H. V. (1967). Resonant particle instabilities in a uniform magnetic field. *Journal of Plasma Physics*, 1(1):75–80.

Khazanov, G. V., Gamayunov, K. V., Jordanova, V. K., and Krivorutsky, E. N. (2002). A self-consistent model of the interacting ring current ions and electromagnetic ion cyclotron waves, initial results: Waves and precipitating fluxes. *Journal of Geophysical Research: Space Physics*, 107(A6):SMP 14–1–SMP 14–9.

Kim, J., Kim, T., Jo, J., Choi, Y., Lee, S., Hwang, H., Yoo, M., and Jeong, D. (2016). A practical finite difference method for the three-dimensional black–scholes equation. *European Journal of Operational Research*, 252(1):183–190.

Klein, K. G. and Chandran, B. D. G. (2016). Evolution of The Proton Velocity Distribution due to Stochastic Heating in the Near-Sun Solar Wind. , 820(1):47.

Kolobov, V., Arslanbekov, R., and Levko, D. (2020). Electron groups in solar wind and gas discharge plasmas. 1623:012006.

Krafft, C. and Volokitin, A. (2006). Stabilization of the fan instability: Electron flux relaxation. *Physics of Plasmas*, 13(12):122301.

Krafft, C., Volokitin, A., and Zaslavsky, A. (2005). Saturation of the fan instability: Nonlinear merging of resonances. *Physics of Plasmas*, 12(11):112309.

Lacombe, C., Alexandrova, O., Matteini, L., Santolík, O., Cornilleau-Wehrlin, N., Mangeney, A., de Conchy, Y., and Maksimovic, M. (2014). Whistler Mode Waves and the Electron Heat Flux in the Solar Wind: Cluster Observations. , 796(1):5.

Landi, S., Matteini, L., and Pantellini, F. (2012). On the competition between radial expansion and coulomb collisions in shaping the electron velocity distribution function: Kinetic simulations. *The Astrophysical Journal*, 760(2):143.

Landi, S. and Pantellini, F. (2003). Kinetic simulations of the solar wind from the subsonic to the supersonic regime. *A&A*, 400(2):769–778.

le Roux, J. A. and Webb, G. M. (2009). Time-dependent acceleration of interstellar pickup ions at the heliospheric termination shock using a focused transport approach. *The Astrophysical Journal*, 693(1):534–551.

le Roux, J. A., Webb, G. M., Florinski, V., and Zank, G. P. (2007). A Focused Transport Approach to Pickup Ion Shock Acceleration: Implications for the Termination Shock. , 662(1):350–371.

Lemaire, J. and Scherer, M. (1970). Model of the polar ion-exosphere. *Planetary and Space Science*, 18(1):103–120.

Lemaire, J. and Scherer, M. (1971). Kinetic models of the solar wind. *Journal of Geophysical Research (1896-1977)*, 76(31):7479–7490.

Lie-Svendsen, Ø., Hansteen, V. H., and Leer, E. (1997). Kinetic electrons in high-speed solar wind streams: Formation of high-energy tails. , 102(A3):4701–4718.

Lie-Svendsen, Ø. and Leer, E. (2000). The electron velocity distribution in the high-speed solar wind: Modeling the effects of protons. , 105(A1):35–46.

Lindquist, R. W. (1966). Relativistic transport theory. *Annals of Physics*, 37(3):487–518.

Livadiotis, G. and McComas, D. J. (2009). Beyond kappa distributions: Exploiting tsallis statistical mechanics in space plasmas. *Journal of Geophysical Research: Space Physics*, 114(A11).

Livadiotis, G. and McComas, D. J. (2013). Understanding Kappa Distributions: A Toolbox for Space Science and Astrophysics. , 175(1-4):183–214.

Livi, S., Marsch, E., and Rosenbauer, H. (1986). Coulomb collisional domains in the solar wind. *Journal of Geophysical Research: Space Physics*, 91(A7):8045–8050.

Ljepojevic, N. N., Burgess, A., and Moffatt, H. K. (1990). Calculation of the electron velocity distribution function in a plasma slab with large temperature and density gradients. *Proceedings of the Royal Society of London. A. Mathematical and Physical Sciences*, 428(1874):71–111.

López, R. A., Lazar, M., Shaaban, S. M., Poedts, S., and Moya, P. S. (2020). Alternative high-plasma beta regimes of electron heat-flux instabilities in the solar wind. *The Astrophysical Journal*, 900(2):L25.

Lyons, L. R. (1974). General relations for resonant particle diffusion in pitch angle and energy. *Journal of Plasma Physics*, 12(1):45–49.

Lyons, L. R., Thorne, R. M., and Kennel, C. F. (1971). Electron pitch-angle diffusion driven by oblique whistler-mode turbulence. *Journal of Plasma Physics*, 6(3):589–606.

Lyutikov, M. and Gavriil, F. P. (2006). Resonant cyclotron scattering and Comptonization in neutron star magnetospheres. *Monthly Notices of the Royal Astronomical Society*, 368(2):690–706.

Maksimovic, M., Pierrard, V., and Lemaire, J. F. (1997). A kinetic model of the solar wind with Kappa distribution functions in the corona. , 324:725–734.

Maksimovic, M., Zouganelis, I., Chaufray, J.-Y., Issautier, K., Scime, E. E., Littleton, J. E., Marsch, E., McComas, D. J., Salem, C., Lin, R. P., and Elliott, H. (2005). Radial evolution of the electron distribution functions in the fast solar wind between 0.3 and 1.5 au. *Journal of Geophysical Research: Space Physics*, 110(A9).

Mann, G., Warmuth, A., and Aurass, H. (2009). Generation of highly energetic

electrons at reconnection outflow shocks during solar flares. *A&A*, 494(2):669–675.

Marsch, E. (2006). Kinetic physics of the solar corona and solar wind. *Living Reviews in Solar Physics*, 3(1):1.

Marsch, E. and Bourouaine, S. (2011). Velocity-space diffusion of solar wind protons in oblique waves and weak turbulence. *Annales Geophysicae*, 29(11):2089–2099.

Marsch, E., Pilipp, W. G., Thieme, K. M., and Rosenbauer, H. (1989). Cooling of solar wind electrons inside 0.3 AU. , 94(A6):6893–6898.

Marsch, E. and Tu, C.-Y. (2001). Evidence for pitch angle diffusion of solar wind protons in resonance with cyclotron waves. *Journal of Geophysical Research: Space Physics*, 106(A5):8357–8361.

McComas, D. J., Bame, S. J., Barraclough, B. L., Feldman, W. C., Funsten, H. O., Gosling, J. T., Riley, P., Skoug, R., Balogh, A., Forsyth, R., Goldstein, B. E., and Neugebauer, M. (1998). Ulysses' return to the slow solar wind. , 25(1):1–4.

McComas, D. J., Barraclough, B. L., Funsten, H. O., Gosling, J. T., Santiago-Muñoz, E., Skoug, R. M., Goldstein, B. E., Neugebauer, M., Riley, P., and Balogh, A. (2000). Solar wind observations over ulysses' first full polar orbit. *Journal of Geophysical Research: Space Physics*, 105(A5):10419–10433.

McComas, D. J., Elliott, H. A., Schwadron, N. A., Gosling, J. T., Skoug, R. M., and Goldstein, B. E. (2003). The three-dimensional solar wind around solar maximum. *Geophysical Research Letters*, 30(10).

Micera, A., Zhukov, A. N., López, R. A., Boella, E., Tenerani, A., Velli, M., Lapenta, G., and Innocenti, M. E. (2021). On the role of solar wind expansion as a source of whistler waves: Scattering of suprathermal electrons and heat flux regulation in the inner heliosphere. *The Astrophysical Journal*, 919(1):42.

Micera, A., Zhukov, A. N., López, R. A., Innocenti, M. E., Lazar, M., Boella, E., and Lapenta, G. (2020). Particle-in-cell simulation of whistler heat-flux instabilities in the solar wind: Heat-flux regulation and electron halo formation. *The Astrophysical Journal Letters*, 903(1):L23.

Moncuquet, M., Meyer-Vernet, N., Issautier, K., Pulupa, M., Bonnell, J. W., Bale, S. D., de Wit, T. D., Goetz, K., Griton, L., Harvey, P. R., MacDowall, R. J., Maksimovic, M., and Malaspina, D. M. (2020). First in situ measurements of electron density and temperature from quasi-thermal noise spectroscopy with parker solar probe/FIELDS. *The Astrophysical Journal Supplement Series*, 246(2):44.

Mourenas, D., Artemyev, A. V., Agapitov, O. V., Krasnoselskikh, V., and Mozer, F. S. (2015). Very oblique whistler generation by low-energy electron streams. *Journal of Geophysical Research: Space Physics*, 120(5):3665–3683.

Nicolaou, G. and Livadiotis, G. (2016). Misestimation of temperature when applying Maxwellian distributions to space plasmas described by kappa distributions. , 361(11):359.

Nolting, W. (2016). *Hamilton Mechanics*. Springer International Publishing, Cham.

Owens, M. J., Crooker, N. U., and Schwadron, N. A. (2008). Suprathermal electron evolution in a parker spiral magnetic field. *Journal of Geophysical Research: Space Physics*, 113(A11).

Pagel, C., Crooker, N. U., Larson, D. E., Kahler, S. W., and Owens, M. J. (2005). Understanding electron heat flux signatures in the solar wind. *Journal of Geophysical Research: Space Physics*, 110(A1).

Pagel, C., Gary, S. P., de Koning, C. A., Skoug, R. M., and Steinberg, J. T. (2007). Scattering of suprathermal electrons in the solar wind: Ace observations. *Journal of Geophysical Research: Space Physics*, 112(A4).

Parker, E. N. (1958). Dynamics of the Interplanetary Gas and Magnetic Fields. , 128:664.

Pavan, J., Viñas, A. F., Yoon, P. H., Ziebell, L. F., and Gaelzer, R. (2013). Solar wind strahl broadening by self-generated plasma waves. *The Astrophysical Journal*, 769(2):L30.

Persson, J. and Persson, L. (2007). Pricing european multi-asset options using a space-time adaptive fd-method. *Computing and Visualization in Science*, 10:173–183.

Phillips, J. L., Bame, S. J., Barnes, A., Barraclough, B. L., Feldman, W. C., Goldstein, B. E., Gosling, J. T., Hoogeveen, G. W., McComas, D. J., Neugebauer, M., and Suess, S. T. (1995). Ulysses solar wind plasma observations from pole to pole. *Geophysical Research Letters*, 22(23):3301–3304.

Pierrard, V., Issautier, K., Meyer-Vernet, N., and Lemaire, J. (2001). Collisionless model of the solar wind in a spiral magnetic field. *Geophysical Research Letters*, 28(2):223–226.

Pierrard, V., Maksimovic, M., and Lemaire, J. (1999). Electron velocity distribution functions from the solar wind to the corona. *Journal of Geophysical Research: Space Physics*, 104(A8):17021–17032.

Pilipp, W. G., Miggenrieder, H., Montgomery, M. D., Mühlhäuser, K. H., Rosenbauer, H., and Schwenn, R. (1987a). Characteristics of electron velocity distribution functions in the solar wind derived from the helios plasma experiment. *Journal of Geophysical Research: Space Physics*, 92(A2):1075–1092.

Pilipp, W. G., Miggenrieder, H., Mühlhäuser, K. H., Rosenbauer, H., Schwenn, R., and Neubauer, F. M. (1987b). Variations of electron distribution functions in the solar wind. *Journal of Geophysical Research: Space Physics*, 92(A2):1103–1118.

Roberg-Clark, G. T., Drake, J. F., Reynolds, C. S., and Swisdak, M. (2016). Suppression of electron thermal conduction in the high intracluster medium of galaxy clusters. *The Astrophysical Journal*, 830(1):L9.

Rosenbauer, H., Schwenn, R., Miggenrieder, H., Meyer, B., Grünwaldt, H., Mühlhäuser, K. H., Pellkofer, H., and Wlofe, J. (1981). Die instrumente des Plasmaexperiments auf den HELIOS- Sonnensonden. *Research report W 81-015: Luft - and space Weltraumforschung / Weltraumtechnologie*, (August).

Rosenbluth, M. N., MacDonald, W. M., and Judd, D. L. (1957). Fokker-planck equation for an inverse-square force. *Phys. Rev.*, 107:1–6.

Ryu, C.-M., Rhee, T., Umeda, T., Yoon, P. H., and Omura, Y. (2007). Turbulent acceleration of superthermal electrons. *Physics of Plasmas*, 14(10):100701.

Saito, S., Gary, S. P., Li, H., and Narita, Y. (2008). Whistler turbulence: Particle-in-cell simulations. *Physics of Plasmas*, 15(10):102305.

Saito, S., Gary, S. P., and Narita, Y. (2010). Wavenumber spectrum of whistler turbulence: Particle-in-cell simulation. *Physics of Plasmas*, 17(12):122316.

Saito, S. and Peter Gary, S. (2012). Beta dependence of electron heating in decaying whistler turbulence: Particle-in-cell simulations. *Physics of Plasmas*, 19(1):012312.

Salem, C., Hubert, D., Lacombe, C., Bale, S. D., Mangeney, A., Larson, D. E., and Lin, R. P. (2003). Electron properties and coulomb collisions in the solar wind at 1 AU:WindObservations. *The Astrophysical Journal*, 585(2):1147–1157.

Schroeder, J. M., Boldyrev, S., and Astfalk, P. (2021). Stability of superthermal strahl electrons in the solar wind. , 507(1):1329–1336.

Scudder, J. D. (1992a). On the Causes of Temperature Change in Inhomogeneous Low-Density Astrophysical Plasmas. , 398:299.

Scudder, J. D. (1992b). Why All Stars Should Possess Circumstellar Temperature Inversions. , 398:319.

Scudder, J. D. (2019). The Thermal Force in Astrophysical Plasmas: Current Free Coulomb Friction. , 882(2):146.

Seough, J., Nariyuki, Y., Yoon, P. H., and Saito, S. (2015). Strahl formation in the solar wind electrons via whistler instability. *The Astrophysical Journal*, 811(1):L7.

Seough, J. and Yoon, P. H. (2012). Quasilinear theory of anisotropy-beta relations for proton cyclotron and parallel firehose instabilities. *Journal of Geophysical Research: Space Physics*, 117(A8).

Shevchenko, V. I. and Galinsky, V. L. (2010). Stability of the strahl electron distribution function and its dynamics. *Nonlinear Processes in Geophysics*, 17(5):593–597.

Skilling, J. (1971). Cosmic Rays in the Galaxy: Convection or Diffusion? , 170:265.

Smith, H. M., Marsch, E., and Helander, P. (2012). Electron transport in the fast solar wind. *The Astrophysical Journal*, 753(1):31.

Spitzer, L. and Härm, R. (1953). Transport phenomena in a completely ionized gas. *Phys. Rev.*, 89:977–981.

Stix, T. H. (1992). *Waves in plasmas*. New York : American Institute of Physics.

Stone, E. C., Cummings, A. C., McDonald, F. B., Heikkila, B. C., Lal, N., and Webber, W. R. (2005). Voyager 1 explores the termination shock region and the heliosheath beyond. *Science*, 309(5743):2017–2020.

Štverák, Š., Maksimovic, M., Trávníček, P. M., Marsch, E., Fazakerley, A. N., and Scime, E. E. (2009). Radial evolution of nonthermal electron populations in the low-latitude solar wind: Helios, cluster, and ulysses observations. *Journal of Geophysical Research: Space Physics*, 114(A5).

Štverák, Š., Trávníček, P. M., and Hellinger, P. (2015). Electron energetics in the expanding solar wind via helios observations. *Journal of Geophysical Research: Space Physics*, 120(10):8177–8193.

Summers, D. (2005). Quasi-linear diffusion coefficients for field-aligned electromagnetic waves with applications to the magnetosphere. *Journal of Geophysical Research: Space Physics*, 110(A8).

Summers, D., Thorne, R. M., and Xiao, F. (1998). Relativistic theory of wave-particle resonant diffusion with application to electron acceleration in the magnetosphere. *Journal of Geophysical Research: Space Physics*, 103(A9):20487–20500.

Summers, D., Thorne, R. M., and Xiao, F. (2001). Gyroresonant acceleration of electrons in the magnetosphere by superluminous electromagnetic waves. *Journal of Geophysical Research: Space Physics*, 106(A6):10853–10868.

Sun, H., Zhao, J., Liu, W., Voitenko, Y., Pierrard, V., Shi, C., Yao, Y., Xie, H., and Wu, D. (2021). Electron heat flux instabilities in the inner heliosphere: Radial distribution and implication on the evolution of the electron velocity distribution function. *The Astrophysical Journal Letters*, 916(1):L4.

Tang, B., Zank, G. P., and Kolobov, V. I. (2020). Numerical modeling of suprathermal electron transport in the solar wind: Effects of whistler turbulence. *The Astrophysical Journal*, 892(2):95.

Taran, S., Safari, H., and Daei, F. (2019). Kappa-Maxwellian Electrons and Bi-Maxwellian Protons in a Two-fluid Model for Fast Solar Wind. , 882(2):157.

Tu, C.-Y. and Marsch, E. (2002). Anisotropy regulation and plateau formation through pitch angle diffusion of solar wind protons in resonance with cyclotron waves. *Journal of Geophysical Research: Space Physics*, 107(A9):SSH 7–1–SSH 7–8.

Ukhorskiy, A. Y. and Sitnov, M. I. (2014). Dynamics of radiation belt particles.

Vasko, I. Y., Krasnoselskikh, V., Tong, Y., Bale, S. D., Bonnell, J. W., and Mozer, F. S. (2019). Whistler Fan Instability Driven by Strahl Electrons in the Solar Wind. , 871(2):L29.

Verscharen, D. and Chandran, B. D. G. (2018). NHDS: The new hampshire dispersion relation solver. *Research Notes of the AAS*, 2(2):13.

Verscharen, D., Chandran, B. D. G., Jeong, S.-Y., Salem, C. S., Pulupa, M. P., and Bale, S. D. (2019). Self-induced Scattering of Strahl Electrons in the Solar Wind. , 886(2):136.

Verscharen, D., Klein, K., and Maruca, B. (2019). The multi-scale nature of the solar wind. *Living Reviews in Solar Physics*, 16(1).

Viñas, A. F., Wong, H. K., and Klimas, A. J. (2000). Generation of Electron Suprathermal Tails in the Upper Solar Atmosphere: Implications for Coronal Heating. , 528(1):509–523.

Vocks, C. (2002). A kinetic model for ions in the solar corona including wave-particle interactions and coulomb collisions. *The Astrophysical Journal*, 568(2):1017–1029.

Vocks, C. and Mann, G. (2003). Generation of suprathermal electrons by resonant wave-particle interaction in the solar corona and wind. *The Astrophysical Journal*, 593(2):1134–1145.

Vocks, C., Salem, C., Lin, R. P., and Mann, G. (2005). Electron halo and strahl formation in the solar wind by resonant interaction with whistler waves. *The Astrophysical Journal*, 627(1):540–549.

Wade, B., Khaliq, A., Yousuf, M., Vigo-Aguiar, J., and Deininger, R. (2007). On smoothing of the crank–nicolson scheme and higher order schemes for pricing barrier options. *Journal of Computational and Applied Mathematics*, 204(1):144–158. Special issue dedicated to Professor Shinnosuke Oharu on the occasion of his 65th birthday.

Webb, G. M. (1985). Relativistic Transport Theory for Cosmic Rays. , 296:319.

Whittlesey, P. L., Larson, D. E., Kasper, J. C., Halekas, J., Abatcha, M., Abiad, R., Berthomier, M., Case, A. W., Chen, J., Curtis, D. W., Dalton, G., Klein, K. G.,

Korreck, K. E., Livi, R., Ludlam, M., Marckwordt, M., Rahmati, A., Robinson, M., Slagle, A., Stevens, M. L., Tiu, C., and Verniero, J. L. (2020). The Solar Probe ANalyzers—Electrons on the Parker Solar Probe. , 246(2):74.

Wilson, Lynn B., I., Chen, L.-J., Wang, S., Schwartz, S. J., Turner, D. L., Stevens, M. L., Kasper, J. C., Osmane, A., Caprioli, D., Bale, S. D., Pulupa, M. P., Salem, C. S., and Goodrich, K. A. (2019). Electron Energy Partition across Interplanetary Shocks. II. Statistics. , 245(2):24.

Yakimenko, V. (1963). Absorption of waves in a plasma (quasilinear approximation). *J. Exptl. Theoret. Phys.*, 17.

Yakovlev, O. I. and Pisanko, Y. V. (2018). Radio sounding of the solar wind acceleration region with spacecraft signals. *Advances in Space Research*, 61(1):552–566.

Yang, X., Wang, W., and Duan, Y. (2009). The approximation of a crank–nicolson scheme for the stochastic navier–stokes equations. *Journal of Computational and Applied Mathematics*, 225(1):31 – 43.

Yoon, P. H. (2017). Kinetic instabilities in the solar wind driven by temperature anisotropies. *Reviews of Modern Plasma Physics*, 1(1):4.

Yoon, P. H., López, R. A., Seough, J., and Sarfraz, M. (2017). Velocity moment-based quasilinear theory and particle-in-cell simulation of parallel electron firehose instability. *Physics of Plasmas*, 24(11):112104.

Yoon, P. H. and Seough, J. (2012). Quasilinear theory of anisotropy-beta relation for combined mirror and proton cyclotron instabilities. *Journal of Geophysical Research: Space Physics*, 117(A8).

Yoon, P. H., Seough, J., Hwang, J., and Nariyuki, Y. (2015). Macroscopic quasilinear theory and particle-in-cell simulation of helium ion anisotropy instabilities. *Journal of Geophysical Research: Space Physics*, 120(8):6071–6084.

Yoon, P. H., Ziebell, L. F., Gaelzer, R., Lin, R. P., and Wang, L. (2012). Langmuir Turbulence and Suprathermal Electrons. , 173(1-4):459–489.

Zank, G. (2013). *Transport Processes in Space Physics and Astrophysics*, volume 877.

Zouganelis, I., Meyer-Vernet, N., Landi, S., Maksimovic, M., and Pantellini, F. (2005). Acceleration of weakly collisional solar-type winds. *The Astrophysical Journal*, 626(2):L117–L120.